UNIVERSITÀ DI TRENTO
Department of Industrial Engineering

XXXIV cycle

Doctoral School in Materials, Mechatronics and System Engineering

# Laser Directed Energy Deposition of tool steels; Investigating the heat treatment strategies and other potentialities of LDED

Sasan Amirabdollahian

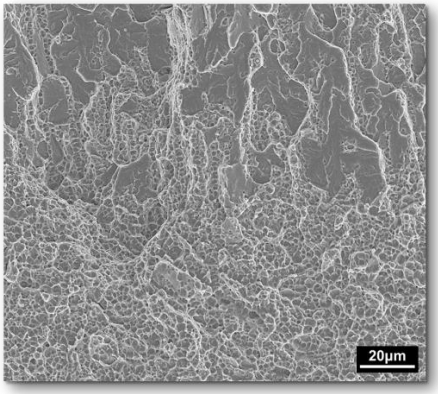


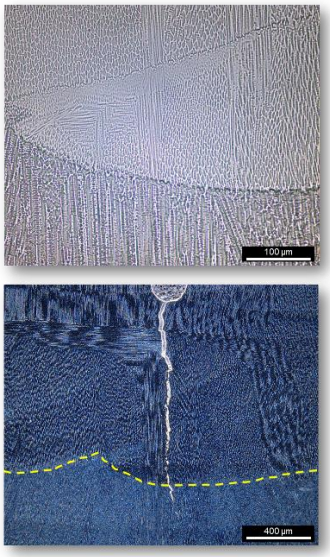


January 2023

# Laser Directed Energy Deposition of tool steels; investigating the heat treatment strategies and other potentialities of LDED

Sasan Amirabdollahian

Email: s.amirabdollahian@unitn.it

**Approved by:**

Prof. Alberto Molinari, Advisor
Dept. of Industrial Engineering
University of Trento, Italy

Prof., Paolo Bosetti, Advisor
Dept. of Industrial Engineering
University of Trento, Italy

Dr. Faraz Deirmina, Co. Advisor
Sandvik Additive Manufacturing,
Sandviken, Sweden

**Ph.D. Commission:**

Prof. Massimo Pellizzari
Dept. of Industrial Engineering
University of Trento, Italy

Prof. Herbert Danninger
Faculty of Technical Chemistry
TU Vienna, Austria

Prof. Riccardo Casati
Dept. of Industrial Engineering
Polytechnic University of Milan, Italy

**University of Trento**

**Department of Industrial Engineering**

**January 2023**

University of Trento

Department of Industrial Engineering

Doctoral Thesis

Sasan Amirabdollahian - January 2023

Published in Trento (Italy) - by University of Trento

ISBN: - - - - - - - - -

# Abstract

Laser additive manufacturing (LAM) has enabled the fabrication of complex and highly customizable metallic parts from a computer-aided design (CAD) file through layer-by-layer construction of the components via local melting of powder/wire using a focussed laser beam. The significant reduction in lead time and the design freedom that allows for substantial savings through weight reduction and the introduction of additional functionality to parts have piqued the industry's interest in these technologies. However, the complicated thermal histories experienced by the components and the very high cooling rates inherent to these processes, lead to different microstructures in the parts, and not all conventional alloys are proper for additive manufacturing (AM). In particular, tool steels with medium to high amounts of carbon are extremely difficult to process due to their susceptibility to cracking. This implies that heat treatments should also be tailored for the LAM parts apart from alloy modification.

Therefore this work tries to study in more detail some of the classic tool steels available in the market, along with two recently utilized tool steels for LAM. The first part of this work is devoted to the microstructural characterization of two carbon-bearing tool steels, namely AISI H13, and X35CrMoMn7-2-1 (PLASWeld Ferro55), fabricated through Laser Directed Energy Deposition (LDED). The as-built microstructure of these steels comprises a martensitic matrix with ~10 vol.% retained austenite (RA) as a consequence of microsegregation at cellular\dendrite boundaries. The tempering behavior is studied consequently, using two heat treatment strategies of direct tempering of the as-built part (DT), and austenitization followed by quenching and tempering (QT). It was demonstrated that in the DT scenario, the secondary hardening peak was shifted to a higher temperature (i.e., 525°C vs. 500°C) which is attributed to the decomposition of RA, producing carbides and fresh martensite in the first tempering step in DT samples. This proved advantageous for tempering resistance of H13 samples tempered to an equivalent hardness, where the hardness values for specimens of 500 HV dropped to 360 HV vs. 300 HV for the DT and QT scenarios, respectively. The apparent fracture toughness for H13 was 70 and 89 $MPa.m^{1/2}$ in the DT and QT specimens, respectively. Similar behavior was also observed for the Ferro55 grade. The Apparent fracture toughness for Ferro55 specimens was considerably higher than H13 specimens tempered to equal hardness (i.e., 110 &106 $MPa.m^{1/2}$ vs. 70 &89 $MPa.m^{1/2}$ for the Fe55-DT&QT and H13- DT&QT, respectively). On the other

hand, H13 specimens demonstrated better tempering resistance. This was attributed to the presence of vanadium carbides which have much lower coarsening rates compared to Cr carbides which are the main constituents in Fe55.

Overall, although the DT scenario demonstrates lower Kapp values compared to the QT scenario, the values are still comparable to the conventionally manufactured (CM) parts, implying that depending on the application, the DT scenario might be a more suitable and economical solution for post-processing. Moreover, for applications where the tool is not subject to high temperatures, Fe55 seems to be a suitable alternative to H13, considering its easier processability and lower tempering temperature required to obtain similar hardness.

In the second part of the work, other potentialities of LDED are investigated on two carbon-free maraging tool steels, namely Osprey® 18Ni300 and Osprey® MAR-60HRC. It is well known that parts undergo a so-called Intrinsic Heat Treatment(IHT) during LAM processes due to thermal cycles that previously deposited layers undergo upon deposition of successive layers. Osprey® MAR-60HRC was selected to investigate IHT due to its higher Co and Mo content which gives rise to faster aging kinetics and higher peak hardness. It was demonstrated that through tailoring the thermal history cycles by applying inter-layer dwell times (IDT), it was possible to trigger the precipitation events during the deposition process and to increase the hardness in the as-built part from 360 HV (no IDT) to 520 HV (IDT-250s). This is particularly advantageous in repair applications where it may be possible to avoid heat treating the entire part.

The comparatively inferior wear resistance of maraging steels compared to tool steels is another typical concern. One solution to this issue is to enhance the hardness. However, this strategy would result in a reduction in fracture toughness. The last part of this work demonstrates that the production of bimetallic specimens or compositionally graded (CG) material can be a successful approach in this regard. Bimetal specimens with a hard surface (Osprey® MAR-60HRC) and tough core (Osprey® 18Ni300) were prepared successfully. The fracture toughness of the sample was significantly increased from ~56 $MPa.m^{1/2}$ (Osprey® MAR-60HRC) to 70 $MPa.m^{1/2}$ with a similar surface hardness.

## ACKNOWLEDGMENTS

First and foremost I would like to express my sincere gratitude to Professor Molinari for always being there when I needed his support, reviewing my progress constantly, and guiding me not only through my Ph.D. studies but all through my years of study at the University of Trento. Furthermore, I would like to thank Prof. Bosetti for his support and for providing me with the opportunity to conduct my research within the context of the AMICO project which provided me with the scholarship.

My heartfelt thanks go out to Prof. Pellizzari for all the guidance and feedback, as well as to Prof. Cristofolini who has supported me since I completed my master's degree.

A special thanks go to Dr. Faraz Deirmina for always being there for me, for his mentorship, and for all his suggestions and criticisms. This work would not have been accomplished without his constant support. I would also extend my acknowledgment to Sandvik additive manufacturing for providing the maraging powders and their support for some of the microstructural characterizations.

I am very thankful to my colleagues at the ProM facility and especially Dr. Matteo Perini for his constant support and supervision with the instruments and sample preparations.

A special thanks to my colleagues and lab mates Marco, Lorena, Farid, Hamid, and Maryam for their help and the perfect time we spent together along the way.

Most importantly I would like to thank my wife Sogol for her endless amount of love and encouragement and for always believing in me, and my family for their unconditional love and unwavering support. Finally, thanks go to my friends here and overseas for being understanding when I was late in answering their phone calls or messages!

Contents

# Chapter 1

# Introduction

## 1.1 Additive Manufacturing

According to the definition by the American Society for Testing and Materials (ASTM), Additive manufacturing (AM), also known as three-dimensional printing (3DP), is defined as the "process of joining materials to make parts from 3D model data, usually layer upon layer", in contrast to subtractive manufacturing (e.g., milling, turning, drilling, etc.) and formative manufacturing (e.g., forging, bending, casting, injection molding, powder metallurgy, etc.) methodologies [1]. This distinctive feature enables the manufacturing of complicated components that, in some cases, are not conceivable through subtractive manufacturing techniques straight from the design. Moreover, by eliminating the need for costly tooling or reducing the time needed to assemble multiple components, AM process reduces lead times by a substantial amount and is cost-effective for small batches and single parts [2].

The AM process can be summarized in eight key steps, as presented below. Since this is a generic procedure, different AM technologies may handle this process sequence differently[3].

1. Conceptualization and CAD
2. Conversion to STL/AMF
3. Transfer and manipulation of STL/AMF file on AM machine
4. Machine setup
5. Build
6. Part removal and cleanup
7. Post-processing of part
8. Application

Various classifications of AM processes can be found in the literature. In general terms, the classifications are: (i) based on the type of base material (polymers, metals, and ceramics); (ii) according to the bonding method (direct and indirect); and (iii) depending on the raw feedstock materials (liquid, molten, powder, and solid layer)[4]. According to ASTM, seven main categories can be defined for AM technologies, presented in Table 1.

Table 1-1 Overview of AM technologies

| AM Category | Process Description | Subcategories | Materials |
|---|---|---|---|
| **Material extrusion (ME)** | Material is selectively dispensed through a nozzle or orifice | FDM, FFF, BPE | Polymer, Metals |
| **Powder Bed Fusion (PBF)** | Thermal energy selectively fuses regions of a powder bed | LPBF, EBM, DLMS, SLS, MJF | Polymer, Metals, Ceramics |
| **Vat Photopolymerization (VP)** | Liquid photopolymer in a vat is selectively cured by light-activated polymerization | VAT, SLA, DLP | Polymer, Composites |
| **Directed Energy Deposition (DED)** | Focused thermal energy is used to fuse materials by melting as they are being deposited | LDED, WAAM, EBAM | Polymer, Metals |
| **Material Jetting (MJ)** | Droplets of build material are selectively deposited | MJ, NPJ, DOD, CS | Polymer, Metals |
| **Binder Jetting (BJ)** | A liquid bonding agent is selectively deposited to join powder materials | BJ | Polymer, Metals |
| **Sheet Lamination (SL)** | Sheets of material are bonded to form a part | LOM, UAM | Polymer, Metals |

## 1.2 Metal Additive Manufacturing

Although additive manufacturing of metal is a relatively new production paradigm, over the course of the last two decades, it has experienced enormous improvements, and due to its demonstrated ability to create complex shapes, it is now being used in serious applications in sectors such as aerospace, automotive, biomedical, energy, and tooling [4]–[9]. A breakdown of various metals applied across diverse sectors may be found in Table 1-2.

Table 1-2 Common alloys in AM and their application[10].

| Applications / Alloys | Aluminum | Maraging steel | Stainless steel | Titanium | Cobalt Chromium | Nickel super- alloys | Precious metals | Refractory metals |
|---|---|---|---|---|---|---|---|---|
| Aerospace | × | × | × | × | × | × | | |
| Medical | | | × | × | × | | × | |
| Energy | | | × | | | | | |
| Oil and gas | | | × | | | | | |
| Automotive | × | | × | × | | | | |
| Marine | | | × | × | | | | |
| Machinability and weldability | | | × | × | × | × | | |
| Corrosion resistance | | | × | × | | × | | |
| Tools and molds | | × | × | | | × | | |
| High temperature | | | × | | | × | | × |
| Consumer products | | | × | × | | | × | |

MJ, ME, and BJ are considered indirect or multi-step MAM processes since there are one or more steps to consolidate the shape and function after the shaping step. Powders are typically kept together by a binder material that keeps them in shape, which is later removed through debinding steps [11]. A further sintering stage is also required in most cases to obtain the desired density and mechanical properties. Widespread adoption of these technologies has been hindered by the additional steps in processing and, in particular, challenges with dimensional control during sintering. Alternatively, powder bed fusion(PBF) and directed energy deposition (DED) are the two most commonly utilized MAM categories due to their distinct advantages [12].

PBF technologies, particularly laser-powder bed fusion (LPBF), being among the most commercialized AM processes, have been hailed as the most versatile metal additive manufacturing processes since they can produce functional near-net shape metallic parts at near-full density with complex geometries in a reduced lead time. The working principle in these methods is to create a thin homogenous layer of powder through a powder feeding system (roller/rake), followed by selective melting and solidification of metallic powders to form the part, followed by recoating with a new layer of fresh powder using a high energy heat source that can be either laser or electron beam. The process is performed in a chamber with a controlled atmosphere (i.e., vacuum for EPBF and inert gas for LPBF) to avoid oxidation[13].

### 1.2.1 Directed energy deposition

In DED, a concentrated high-energy heat source (laser, electron beam, electric arc\plasma) is employed to form a melt pool on a substrate where the material to be deposited is introduced simultaneously (powder or wire), and the final part is realized through layer by layer deposition[14]. DED can be divided into various

categories considering the type of heat source and the feedstock, as presented in Figure 1-1.

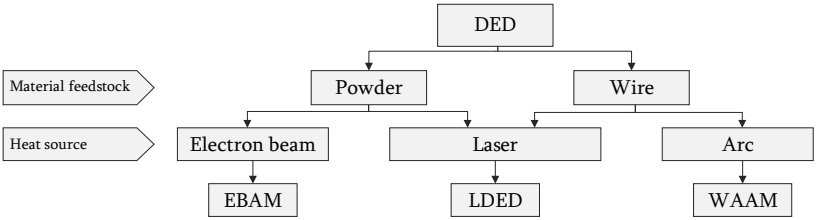


Figure 1-1 Classification of DED processes.

As an AM process, DED is well suited to the deposition of high-performance metals, including stainless steel, tool steel, alloy steel, titanium-based alloys, cobalt-based and nickel-based alloys, high-entropy alloys, and functionally graded materials (FGMs)[15]. Some of the advantages and disadvantages of the DED process, according to ASTM 3413[16], are as follows.

**Advantages:**

A broad range of feedstock materials; better mechanical properties in the as-built (AB) condition compared to PBF parts; the possibility of local adjustment of properties by tailoring the processing parameters; higher deposition rates and the potential to deposit larger components compared to PBF; larger particle size distribution (PSD) compared to PBF (considering cost and safety); possibility to deposit complete parts, partial features, coatings, or repair in the same machine; Possibility of combination with subtractive methods in the same machine (hybrid manufacturing); ability to manufacture multi-material, composite, or FGM parts

**Disadvantages:**

Local temperature differences in parts can result in residual stress and deformation; lower-dimensional resolution compared to PBF; limitations with the complexity of the part's geometry; lower powder efficiency and powder recyclability compared to PBF (in powder systems).

### 1.2.2 Laser directed energy deposition

The most common DED technique, laser directed energy deposition (LDED), was commercialized in the mid-1990s based on Laser Cladding (LC) technology.

Depending on the different variations and groups that developed the technology, it is known by several names such as Laser Engineered Net Shaping (LENS)[17], Direct Laser Powder Deposition (DLPD)[18], Direct Metal Deposition (DMD)[19], Laser-aided Metal/Material Deposition (LMD)[20], to name a few. Although wire-based LDED machines might be advantageous for increasing process efficiency and surface quality, their prevalence in the field is substantially less than that of powder-fed LDED[14]. In LDED, a focused laser beam is employed to fuse and consolidate the intended material (powder or wire), which is delivered simultaneously into the melt pool to accomplish the deposition. A fraction of the laser's heat is absorbed or reflected by the powder particles, but the majority is absorbed by the substrate upon which the material is deposited, producing a controlled melt pool on the surface. Typically, an inert gas is introduced into the deposition area to reduce the risk of oxidation. Depending on the main parameters, spot size, scan speed, and laser power, the melt pool size in the order of a few centimeters and layer thickness might vary between hundreds of microns to 1 mm, and build rates up to 300 $cm^3/h$ can be achieved [7]. Figure 1-2 presents a schematic of a powder-based LDED system with a co-axial nozzle.

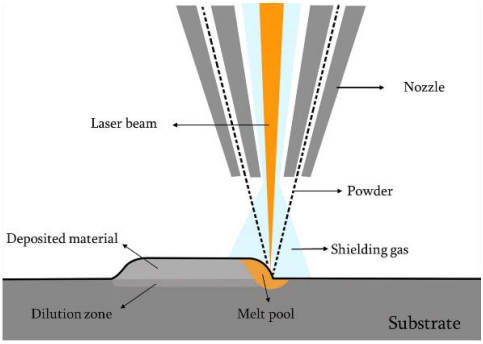


Figure 1-2 Schematic of a powder LDED system with co-axial nozzle

Manufacturing high-quality parts through LDED technology is an exceedingly complicated process. Several coupled physical phenomena occur concurrently in powder-based DLD on a concise time scale, and numerous processing variables can influence the part's thermal history and solidification (Figure 1-3). All these might consequently affect the microstructure and properties of the as-deposited material[21].

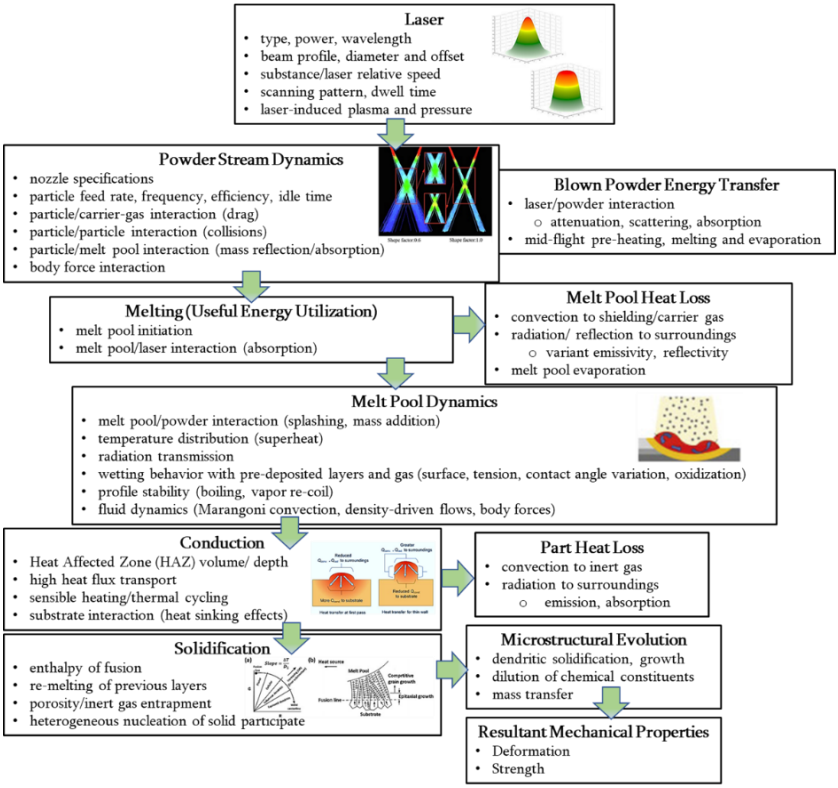


Figure 1-3 Physical occurrences during LDED (adapted from[14])

As demonstrated in Figure 1-3, powder-based LDED is highly challenging to model due to the multiple physical phenomena interacting simultaneously. Therefore, studies aimed at enhancing the quality of LDED parts typically employ an experimental approach to identify optimal process parameters and achieve some targeted product attributes using tools such as the statistical design of experiments (DOE). The three key processing factors regarded in LDED are the laser power, the laser scan speed, and the powder flow rate[3], [22], [23]. While numerous reports have examined the effect of the LDED process parameters on the properties of the deposited material[24]–[28], no detailed study has been conducted concerning the relationship between crosslinking interactions. Moreover, many of the inherent physical properties are not constant and have significant alterations as the process proceeds and the thermal history of the part changes. Therefore, various models have been proposed for controlling the build

height, including systems that adjust the powder feed rate [29], systems that use closed control loops to stabilize the meltpool dimension by altering the power and traverse speed [30], systems that control traverse speed [31], and even by varying the power stream shape [32]. The application of artificial intelligence (AI) in DED has been thoroughly examined with the goal of reducing reliance on human intervention while increasing control over the process's more intricate elements. Several AI techniques, including neural networks(NN), support vector machines (SVM), and gaussian process (GP) techniques, are capable of achieving this objective. These models have been used in the DED process and trained for very accurate results. They demonstrated prediction accuracy ranging from 80% to 97% for various approaches and varied attributes[33].

Despite the well-known advantages of the process, it is known that parts built by LDED often exhibit non-uniform microstructure and properties which can confine their application [34]. In DED techniques, heat is dissipated mainly through conduction to the substrate, conduction to the build material, and convection to the shield gas [35]. The microstructure and properties of laser-deposited materials depend on the solidification and the solid-state transformations that happen upon cooling to ambient temperature [36]. Typically, columnar grains are observed to develop epitaxially from the substrate or the previously deposited layer in the direction of the heat source's scanning due to directional heat flux. To manufacture parts with proper mechanical properties, exerting modifications to the grain structure, such as the columnar-to-equiaxed transition (CET), is necessary[37]. Controlling the microstructure can be approached from either the grain or phase perspective. The microstructural evolution in LAM parts can be manipulated through thermal gradient (G) and growth rate (R) by altering processing parameters like power, scanning speed, scanning strategy, and baseplate preheating. The G/R ratio affects the mode of solidification (morphology), while the size of the solidification structures is determined by GR or the cooling rate [10]. Modulating the laser profile[38] or intensity [39] has also been applied successfully to modify the microstructure. On the other hand, phase control is more challenging since both the solidification and solid-state phase transformations are involved, and manipulation of process parameters for optimization of thermal history for precipitation can be at the expense of solidification and grain size control [35]. The majority of investigations in this area are restricted to the control of in-situ aging of LAM material [40], [41].

Two other distinctive applications of DED technologies are alloy design and fabrication of multi-material parts[42]–[45]. DED processes are the most common AM processes for metal multi-material Additive manufacturing (MM-AM) [45].

## 1.3 Tool steels

Generally, tool steels are ferrous alloys that are used to manufacture tools, dies, and molds for shaping, forming, and other materials. In a more detailed definition: "Tool steels are carbon alloy, or high-speed steels, capable of being hardened and tempered. They are usually melted in electric furnaces and produced under tool steel practice to meet special requirements. They may be used in certain hand tools or mechanical fixtures for cutting, shaping, forming, and blanking materials at either ordinary or elevated temperatures. Tool steels are also used in a wide variety of other applications where resistance to wear, strength, toughness, and other properties are selected for optimum performance[46]".

This description emphasizes the wide range of chemical compositions that can be found in tool steels, from those with minimal alloying elements to those with very high quantities. Each of these groups shares the potential to undergo heat treatment—particularly hardening and tempering—to enhance their properties. This is a defining property of tool steels since it indicates a significant increase in mechanical properties after heat treatment. However, this possibility depends on applying proper heat-treatment conditions, which also depend upon their metallurgical properties[47]. Some of most essential requirements and characteristics of the tool steels are as follows[46], [48], [49]:

- **Compressive strength**: to endure the severe clamping forces during the molding process
- **Toughness**: to withstand cracking and fractures
- **Wear resistance**: to resist surface deterioration throughout the service
- **Fatigue resistance**: to withstand the cyclic load that the die material is subjected to.
- **Thermal conductivity**: for a better heat sink and control of mold temperature for higher productivity
- **Corrosion resistance**: to withstand chemical reactions in contact with corrosive media and the cooling channels
- **Machinability**: to reduce cost and time for tool manufacturing
- **Dimensional stability upon heat treatment**: to minimize shape/dimensional corrections after heat treatment

Many designations have been introduced for tool steels based on their application or chemical composition, among which the ASTM designation[50] presented in Table 1-3 is one of the most common.

Table 1-3 Classification of tool steels according to ASTM

| ASTM Classification | Symbol |
|---|---|
| Water-hardening tool steels | W |
| Shock-resisting tool steels | S |
| Oil-hardening cold work tool steels | O |
| Air-hardening, medium-alloy cold work tool steels | A |
| High-carbon, high-chromium cold work tool steels for Dies | D |
| Plastic mold steels | P |
| Hot work tool steels, chromium, tungsten | H |
| Tungsten high-speed tool steels | T |
| Molybdenum high-speed tool steels | M |

### 1.3.1 Tool steels in Laser-based Additive Manufacturing

The tool steels used in AM generally fall into two categories: carbon-bearing tool steels and carbon-free maraging steels [51]. The high cooling rate inherent to LAM methods satisfies the condition for obtaining an almost fully martensitic microstructure in the AB condition for both groups. The ultimate microstructure for both categories consists of martensite and precipitates, while the precipitates consist of secondary carbides in the first group and intermetallics in the latter. Although the as-built martensitic microstructure in high Ni maraging steels is soft and needs an aging treatment for precipitation hardening, the AB martensitic structure is very brittle in the carbon-bearing steels and prone to cracking due to residual stresses that form during AM process[52]. Since many AM technologies have not yet reached industrial maturity, relatively few steel powders tailored for AM are available in the market, and powders for thermal spraying and laser cladding are utilized for AM[53].

#### 1.3.1.1 Carbon-bearing tool steels

As discussed earlier, the fully martensitic brittle microstructure of carbon-bearing tool steels makes them hard to process, and a substantial amount of literature is devoted to finding the processing parameters for obtaining crack-free and sound samples. It is generally acknowledged that an increase in the carbon content of steel declines its weldability and increases its susceptibility to cracking[54]. Hence,

the number of carbon-bearing AM processed tool steels is limited to some low-medium carbon grades, namely the high-speed steels (HSS) M2[52], [55], M4[56], and HSS P20 [57]; cold work steel X65MoCrWV3-2 [58]; and hot work tool steels H11[59]–[61], and H13[62]–[71]; with the exception of medium-high air hardening steel D2[72], [73]. It can be noticed that most of the studies are dedicated to H13 hot work tool steel, owing to its widespread application due to a decent combination of hardness, toughness at high temperatures, tempering resistance, and wear resistance at high temperatures [46]. Considering grades with higher C content, preheating the baseplate would be necessary for avoiding the cracking issue, e.g., preheating in the range of 200-500˚C is advised for M4; however, this can result in lower toughness and strength at higher preheating temperatures [74], [75].

The as-built microstructure of the LDED-H13 tool steel consists of solidification cells/dendrites with considerable amounts of retained austenite within the intercellular/dendritic regions [51], [62], [70], [76]. Depending on the processing parameters and sampling position, the cell size can vary between 2 to 30 μm [36], [72], [77], [78]. Indeed, as the height increases throughout the deposition, the cooling rate declines since the heat sink into the base plate is reduced. Consequently, solidification cell diameters at the upper parts of the component are larger than those at the bottom [36]. The cellular structure results from constitutional undercooling that is accompanied by microsegregation, which leads to the enrichment of some alloying elements in the interdendritic regions. Brooks et al. [63] investigated the as-built microstructure of LDED-H13 through Wavelength-dispersive X-ray spectroscopy (WDS). They suggested that C, Cr, Mo, and V are enriched in the interdendritic/intercellular region so that intercellular austenite could be stabilized down to room temperature. This can be justified in view of the martensite transformation start temperature (Ms) since a decrease in the Ms temperature would lead to an increase in retained austenite content[79]. The relation between Ms and alloying elements can be expressed as[80]:

$$\mathrm{Ms}\ (°\mathrm{C}) = 521 - 353(\%\mathrm{C}) - 225(\%\mathrm{Si}) - 24.3(\%\mathrm{Mn}) - 27.4(\%\mathrm{Ni}) - 17.7(\%\mathrm{Cr}) - 25.8(\%\mathrm{Mo}) \quad (\text{Eq. } 1.1)$$

Accordingly, an increase in the amount of the aforementioned allowing elements declines the Ms and increases the amount of RA. Therefore, the as-built LDED H13 microstructure is martensitic with low amounts of retained austenite enriched with alloying elements. However, the martensite is tempered due to the intrinsic heat treatment (IHT) that parts experience during the LDED process [62]. This intrinsic heat treatment results from successive thermal cycles related to the deposition of each new layer [81]. Therefore, the top layer of a sample that experiences negligible IHT has a higher hardness in comparison to that of lower

layers with significant IHT [60], [65], [76], [82]. Additionally, different carbides have been reported to be present in the as-built LDED-H13 [3,4,12,14–16]. Specifically, lower layers of a part that have gone through many IHT cycles contain Cr and V-rich carbides [63] that are reported to be mostly MC carbides, with minor quantities of $M_7C_3$ carbides [78].

The conventional heat treatment of hot-work tool steels consists of austenitization, quenching, and multiple tempering to reach the desired hardness. This leads to a microstructure that comprises tempered martensite with a dispersion of secondary alloy carbides and a combination of properties, such as uniform hardness profile, hot strength, good toughness, thermal conductivity, and temper resistance. For the as-built LDED-H13, mechanical properties such as tensile strength (UTS ~2000 MPa), elongation at break (5–6%), and hardness values (550 to 700 HV) [66], [76], [82], [83] are comparable to those of conventionally heat-treated wrought material, which also indicates the in-situ tempered state [78]. This implies that the costly post-processing heat treatment could be avoided in particular applications. However, the non-uniformity of hardness along build direction, microstructural inhomogeneities due to the incomplete in-situ tempering, and existence of RA in the as-built LDED-H13 might be problematic in many processes and should be avoided in many high-temperature applications such as high-pressure die casting.

Another important issue to consider is the effect of IHT and thermal cycles on the properties of the LAMed parts. According to some studies, IHT variations can change microstructure, hardness, defects, residual stress, etc. in as-built components, resulting in inconsistent part quality and reducing repeatability of component quality [84]. It has been demonstrated that a greater number of thermal cycles increased the thermal stability of the retained austenite, which may lead to a reduction in CTE. A continuous decrease in the lattice parameters of martensite has been observed as the number of thermal cycles increased, indicating that higher compressive residual stresses might be developed in the material which can lead o inhomogeneity of residual stress distribution along the part height[85]. These variations in residual stresses, microstructure, and mechanical properties are well known to subsequently influence the fatigue properties of the material as they have a significant impact on the three stages of fatigue crack growth (FCG)[86], [87]. Therefore, studying the heat treatment and tempering behavior of LDED H13 is of high importance in achieving application-specific mechanical and thermo-mechanical requirements.

#### 1.3.1.2 Maraging steels

Maraging steels are a class of high-performance, low-carbon martensitic steels that combine ultra-high strength (UTS>≈1800 MPa) and high toughness [88]. The relatively soft and tough Fe-Ni martensite can be age-hardened by the precipitation of nano-sized intermetallic particles containing substitutional alloying elements (e.g., Mo, Ti, Al) through a simple heat treatment. Due to the high Ni content and the absence of C (less than 0.03wt%), hardenability is not an issue in these alloys, and hence cooling rate after solution annealing treatments is not critical [89]. In the solution annealed condition, the alloys, depending on the type and content of alloying elements, show hardness of the order of 30 HRC. Parts can be thus readily machined. Additional hardening can be achieved by aging at the recommended temperatures and times [90]. Dimensional changes after aging treatments are generally negligible, thus enabling finishing operations to be carried out on the parts before age hardening. They also show good polishability [89], [91]. More importantly, their excellent toughness at high strength levels makes this steel class an ideal candidate for use in applications requiring high strength-to-weight ratios [91], [92]. Maraging steels are therefore considered viable materials for tooling applications such as injection molds, extrusion tools, die-casting dies, core pins, and cores, as well as for structural applications [91].

Due to their excellent weldability even without preheating and negligible dimensional changes after age hardening, maraging steels have been exploited commercially in near-net shape AM processes such as LPBF and LDED [93]. On an industrial scale, parts in 18Ni300 (18.0Ni-9.0Co-4.5Mo-0.7Ti-0.1Al, Fe bal. (wt.%)) with complex geometries and enhanced mechanical properties have already been commercialized [94]. This steel shows a peak hardness of ~600 HV, and tensile strength of ~2000 MPa, with good ductility and toughness. 18Ni300 is the most extensively used alloy in AM for maraging steels[88], [95]–[101]. However, due to their simpler processability compared to carbon-bearing tool steels, more classes have been investigated in the literature, namely 14Ni200 [102], 18Ni250[103], Ti-free grade 300[104], CX(Fe-Cr-Ni-Al)[105]–[107], M789 (grade250)[108], [109], and some other Co-free grades [110]–[112]. The AM-processed maraging steels possess a cellular/dendritic solidification microstructure with cell size in orders of a few micrometers and relatively coarse PAGs in the range of a few millimetres for LDED. The general microstructure is martensitic, although RA is present in significant amounts (up to 11% depending on the AM process and parameters) due to the microsegregation of Ni at cellular boundaries, stabilizing austenite up to room temperature.[100].

The addition of Co in this alloy system raises the Ms temperature, enabling the addition of more substitutional alloying elements (e.g., Mo) without the risk of

stabilizing retained austenite [113]. Moreover, Co increases the supersaturation of Mo in the matrix, increasing the amount of this element participating in precipitation. The combination of Co with a specific weight percentage of Mo, as in the Mo-containing quaternary alloys (Fe-18Ni-Co-Mo), increases the strength by up to 500 MPa [89], [113]. Ti is the other alloying element contributing to age hardening at low weight percentages (i.e., 0.2 to ~2.0 wt.%) [114]. The conventional heat treatment for managing steels comprises solution annealing (820-1100˚C) followed by aging (480-580˚C). Depending on the alloying elements, the main intermetallic strengthening compounds in these systems are orthorhombic $Ni_3(Mo)$, hexagonal $Ni_3(Ti, Al)$, rhombohedral $Fe_7Mo_6$ μ phase, hexagonal $Fe_2Mo$ Laves phase, hexagonal ω phase, $Ti_6Si_7Ni_{16}$ G phase, and $A_8B$ hexagonal "S phase" [114]–[118]. Some studies have demonstrated that solution treatment can be avoided for LPBF-processed samples since the intermetallic precipitates have a more significant strengthening impact than the retained austenite and that the reversion of austenite plays a minimal role in the fracture process[96].

However, in certain applications, a further increase in hardness aimed at increasing the wear resistance of 18Ni300 has been considered a crucial requirement as it is known to be one of the most efficient ways to deal with high wear in use[119]. In recent years, several Fe-18Ni-Co-Mo alloys have been developed on an industrial and research scale [91]-[120], and Ni-Co-Mo compositions with lower Ni content as well as Co-free classes have been assessed [121]–[126]. Recently a new class of MAR-60HRC-AM has been developed, showing a maximum achievable hardness of ~61HRC and ultimate tensile strength of ~2600 MPa [127]. The higher Co and Mo content in this alloy gives rise to higher vol.% and enhanced $Ni_3Mo$ and μ phase precipitation kinetics leading to higher hardness after aging. The fracture toughness versus hardness for some of the maraging steel available in the literature is presented in Figure 1-4. As expected, a drop in fracture toughness is evident by increasing the hardness.

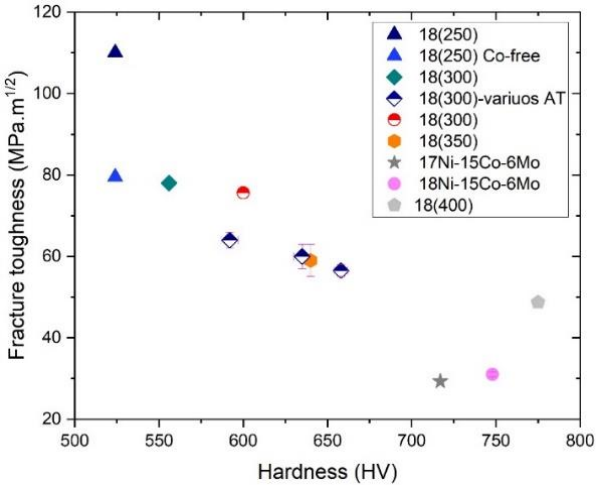


Figure 1-4 Fracture toughness vs. Hardness for different maraging steels. Half-filled symbols belong to AM samples [124], [128]–[131].

Other than alloy modification, the hardness can be increased through the addition of hard ceramic particles to fabricate AM 18Ni300 metal matrix composites. However, it is reported that substantial additions of reinforcing particles result in collision and agglomeration of un-melted/un-dissolved ceramic particles with much higher melting points than that of the matrix to the sides of the melt pools [132], [133]. The stabilization of retained austenite using carbon-containing ceramic particles such as TiC and WC is also documented, and interfacial reactions between the matrix and the reinforcement leading to the embrittlement of the interface are witnessed in some research works [132], [134], [135]. More importantly, mixing the ceramic particles with steel powders introduces an additional step to the process chain with the risk of powder contamination. In other studies, plasma nitriding has been applied to increase the surface hardness of 18Ni300 [136]–[138]. The process is assessed to increase the surface hardness of AM-18Ni300 both in the direct aging and after solution annealing aging. The surface hardness is reported to reach up to 1000 $HV_{0.01}$, and it declined to ~700 $HV_{0.01}$ within 30 µm from the surface and gradually dropped to the value of the base material at a depth of ~100 µm. The presence of some connected pores and cracks in the compound layer of the nitrided zone and the formation of discrete TiN particles are reported for the nitriding of AM-18Ni300 [138]. Another approach for realizing parts with different properties on the surface and at the core is producing bimetals. To date, few studies have investigated the fabrication of

bimetals of maraging steels [139], [140], and these studies are limited to LPBF of maraging steels on a tool steel baseplate. Although, the different heat treatment responses of these materials might be a limiting factor in some applications.

Maraging steels are also auspicious materials to exploit IHT capability in the in-situ strengthening of the LDED parts. Due to the layer-wise nature of this technique, the part experiences multiple thermal cycles comprising reheating and rapid cooling upon deposition of successive layers, with gradually decaying peak temperatures. In their pioneering work, Kürnsteiner et al.[141] demonstrated the possibility of IHT for a tailor-made Fe19Ni5Ti (wt.%) maraging steel through mixing a pre-alloyed Fe20Ni(wt.%) with commercially pure Ti powder to enhance $Ni_3Ti$ precipitation kinetics compared with that of 18Ni300 by incorporation of a higher amount of Ti. They could successfully increase the yield strength and ductility by adjusting the thermal history of parts by applying interlayer dwell time, leading to the cooling of deposited layers below $M_s$ temperature during the dwell time and reheating them to the aging temperature interval as a result of the deposition of successive layers. In another research [142], this effect has been investigated on ternary Fe-Ni-Al alloy by mixing $Fe_{20}Ni$(wt.%) with Al powders with varying amounts of Al up to 12 at.% to exploit the strengthening effect of coherent NiAl nano-precipitates inside martensite [143] during LDED. However, given the high affinity of Ti and Al for O, pre-alloyed powders with the aforementioned compositions might not be easy to process through some standard powder processing routes (e.g. gas atomization), as well as during the deposition of the material due to O and N pick-up.

# Chapter 2

# Motivations and Aim of the Work

In recent years, the application of AM in some industrial sectors has substantially impacted production paradigms. One of the sectors that can hugely benefit AM technologies is tooling. Laser Directed Energy Deposition is one of the most practiced Laser-based AM technologies due to its high production rates, large building volumes, design freedom, and ability to use multiple feedstocks simultaneously. LDED opens new ways for the fabrication of tools with intricate designs as well as for dies and mold repair. Some surveys have revealed that DMD can reduce the time for die production by 40 percent[62] and increase the life cycle of the tool (through remodeling and introducing conformal cooling channels) by up to 40 percent[19]. The global molds and dies market size was valued at $200.8 billion in 2018 and is forecasted to reach $368.5 billion by 2026[144]. Hence, considering the size of the tooling market and the great advantages that AM can bring to this sector, and given the limited knowledge of the tool steels in AM, this work aims to contribute to deepening the knowledge of tool steels manufactured by AM and explore some advantages of AM in tooling.

As described in chapter 1, the tool steels in AM are divided into two categories of carbon-bearing tool steels and carbon-free maraging steels. The present work is accordingly divided into two parts. In the first section, it has been tried to investigate heat treatment scenarios for carbon-bearing tool steels. For carbon-bearing tool steels, quenching yields a hard, brittle martensitic matrix devoid of precipitates, and tempering helps restore some ductility by precipitating carbon from the martensite matrix as carbides. Despite the well-known advantages of the process, it is known that parts built by LDED often exhibit non-uniform microstructure and properties which can confine their application[145]. Yet, this AB microstructure is almost fully martensitic and resembles the quenched microstructure. Therefore, the elimination of the costly and time-consuming austenitization step can be a dream goal for part manufacturers. Few works have been conducted to study this scenario [146], [147]. Therefore, the first part of the current work aims to comprehensively study the effect of these two different heat treatment strategies on the microstructure and mechanical properties. To this aim, samples' fracture toughness and tempering resistance are compared for the two

scenarios. The last part of the work regarding the carbon-bearing tool steels is dedicated to investigating the properties of X35CrMoMn7-2-1 steel, which has been recently proposed as an alternative to H13 for some tooling applications, e.g. plastic injection molding tools. The tempering behavior of the material and the fracture toughness are investigated and compared to those of H13. Moreover, since die steels are typically exposed to temperatures ranging from 315 to 650 °C[148], hence resistance to thermal softening is an important property for these steel; therefore, the tempering resistance of the two aforementioned tool steels are studied and compared in the two heat treatment scenarios.

Austenitization and quenching are expected to dissolve microsegrations, eliminate the prior solidification structure and homogenize the microstructure. The research question in the first part of this study was to investigate the influence of eliminating the costly quenching step in the heat treatment of L-DEDed carbon-bearing tool steel H13, and in particular, the newly employed grade X35CrMoMn7-2-1 that has not been investigated before, on tempering behavior, and material's properties, namely fracture toughness and tempering resistance.

The second part of this work is dedicated to directed energy deposition of carbon-free maraging tool steels. One of the disadvantages of maraging steels in comparison to high alloy tool steels is their lower hardness (typically 50-57HRC)[149], which results in lower wear resistance and confines their application for some tooling purposes, e.g., blanking and trimming of high- strength steels[150]. In this regard, a newly developed grade of maraging steels with higher Co and Mo content compared to that of 18Ni300 was chosen for laser directed energy deposition. As discussed in chapter 1, this results in a higher martensite start (Ms) temperature and might reduce the risk of RA and give rise to a faster aging response, making the alloy a good candidate for investigating IHT. Successful application of IHT can be substantially beneficial since costly post-processing aging heat treatment can be avoided. Moreover, this can be greatly advantageous for the repair of tools, where only localized heat treatment is required.

Increasing surface hardness is one of the most practice ways to improve the wear resistance of maraging steels and in particular to deal with abrasive wear [113]. In some studies, plasma nitriding has been employed to increase the surface hardness, but due to limitations with temperature and time for the nitriding process (to avoid overaging maraging), the outcomes are not so satisfactory. This is mainly because high nitriding temperatures or times should be avoided in maraging steels (overaging), and therefore the thickness of the nitrided layer is often very limited. Another approach is the fabrication of metal matrix composites (MMC) by introducing high melting point particles such as TiC or WC. The main disadvantage of this approach is introducing an extra step in preparing the powders, which is

costly and increases the risk of contamination. Alloy modification can also be applied to increase the hardness. The combined effect of Co and Mo can give rise to higher hardness in maraging steels. However, hardness has an inverse relation with fracture toughness which is another important factor in tooling applications.

Therefore, the contribution of the second part of this work was first to study the heat treatment behavior and properties of a newly developed grade that possesses considerably higher hardness in comparison to the well-established 18Ni300 grade. Secondly, given the fast aging response of this commercially available grade, the feasibility of the application of intrinsic heat treatment for Osprey® Mar-60HRC is studied. Lastly, given the potential capability of powder mixing in the LDED process, various solutions for increasing the surface hardness by preparing bimetal or compositionally graded specimens with Osprey® Mar-60HRC and Osprey®18Ni300 were investigated, taking their fracture toughness into account.

# Chapter 3

# Materials and Experimental Procedures

## 3.1 Powders

As mentioned in chapter 2, two types of maraging steels and two medium carbon tool steels are used in this study. The powders used in this work are all commercially available gas-atomized powders. The first powder is Osprey ® H13 powder (Sandvik Osprey). The particle size distribution of the powder is measured using the laser diffraction analysis (LD) method with a 1064 CILAS analyzer, and the volume-weighted percentiles of the powder were $D_{10}$ = 57 µm, $D_{50}$ = 81 µm, and $D_{90}$ = 109 µm. The SEM micrograph of the powder and the PSD results are presented in Figure 3-1.

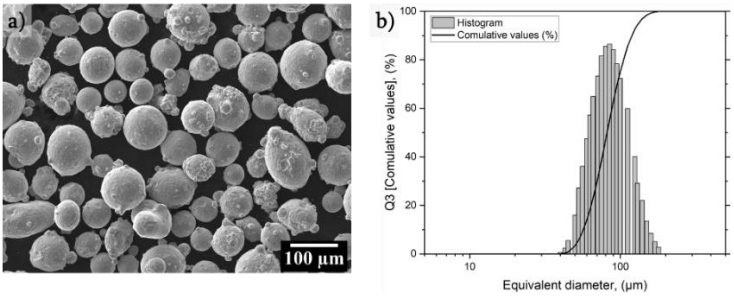


Figure 3-1 a) SEM micrograph of AISI H13 powder, b) PSD of the powder.

The second powder is PLASweld Ferro55 (X35CrMoMn7-2-1), developed by Voestalpine Böhler. For the sake of simplicity, it is hereafter referred to as Fe55. The volume-weighted percentiles of the powder were $D_{10}$ = 63 µm, $D_{50}$ = 96 µm, and $D_{90}$ = 145 µm. Figure 3-2 illustrates the SEM micrograph of the powder as well as the PSD results.

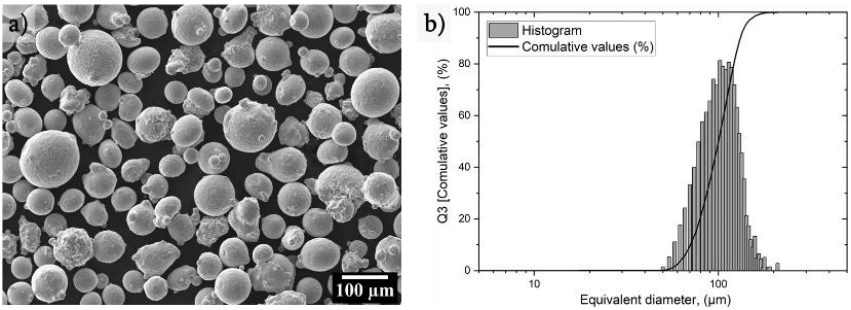


Figure 3-2 a) SEM micrograph of Fe55 powder, b) PSD of the powder.

Two classes of maraging steels were used, both provided by Sandvik Osprey. The first powder is the well-established Osprey® 18Ni300 type, while the second one is a recently developed type specifically tailored for additive manufacturing that, due to higher Co and Mo content, can provide better hardness and strength and resembles the M350 category. The powder is commercially known as MAR60-HRC-AM, which hereafter will be referred to as Osprey ® MAR-60HRC for brevity. Both powders have a PSD in the range of -105µm +50µm. The SEM micrographs of the powders are presented in Figure 3-3.

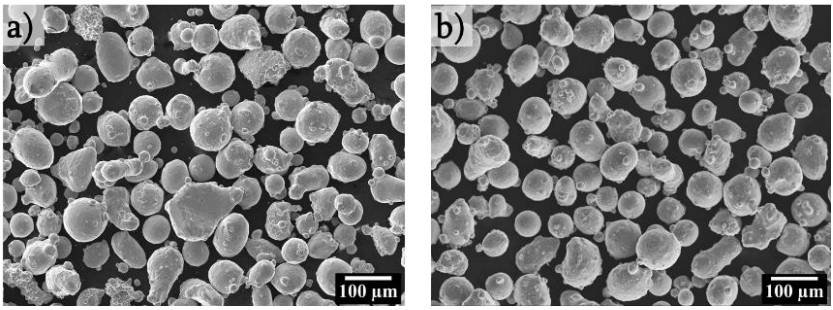


Figure 3-3 SEM Micrographs of maraging steels, a) Osprey® 18Ni300 and b)Osprey® MAR-60HRC.

The chemical compositions of all the powders are presented in Table 3-1.

Table 3-1 Chemical composition of the powders (wt.%)

| element | Osprey ® H13 | Ferro55 | Osprey ® 18Ni300 | Osprey ® MAR-60HRC |
|---|---|---|---|---|
| C | 0.4 | 0.3 | <0.03 | <0.03 |
| Cr | 5.2 | 6.9 | - | - |
| Mn | 0.5 | 1.0 | - | - |
| Si | 1.0 | 0.4 | - | - |
| V | 1.2 | - | - | - |
| Mo | 1.6 | 2.0 | 4.7 | 10.0 |
| Ni | - | - | 18.0 | 13.0 |
| Co | - | - | 9.5 | 15.0 |
| Ti | - | - | 0.7 | <0.2 |
| Al | - | - | <0.1 | <0.1 |
| Fe | Bal. | Bal. | Bal. | Bal. |
| O | 0.037 | 0.022 | - | - |
| N | 0.052 | 0.021 | - | - |

## 3.2 Additive manufacturing

All the depositions were carried out using a LASERTEC 65 3D hybrid machine (DMG MORI AG). The machine is equipped with a 2500W diode laser (λ = 1020 nm) and a Coax 14 nozzle. The laser has a top-hat beam profile with a spot diameter of 3 mm at a focal length of 13 mm. The machine has a pneumatic powder handling system with dual powder containers that allow simultaneous use of the powders. Commercial pure Argon (grade 4.8) was employed as both carrier gas and shielding gas with a flow rate of 5 and 5.5 l/min, respectively.

A work process, as represented in Figure 3-4, was followed in order to obtain appropriate processing parameters for each material. Depositions of medium carbon tool steels were performed on C40 mild steel plates of 120x120x20 $mm^3$, while maraging steel depositions were made on 415 martensitic stainless steel baseplates (110x110x20 $mm^3$).

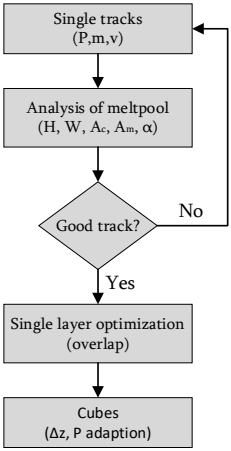


Figure 3-4 The flowchart for process optimization in LDED

As discussed earlier, due to the substantial amount of bulk heating in parts, the laser power should decrease with each successive layer to achieve better control of the melt pool shape. A 5% decrease in the power is suggested by means of simulation methods [145], and accordingly, the laser power was adjusted for the process by a 100W decline in laser power after each layer at the beginning of the process until a stable melt pool was achieved. A summary of the processing parameters and the initial laser powers for all the utilized materials are presented in Table 3-2.

Table 3-2 Process parameters utilized for deposition of the studied materials, where P is laser power, m′ is powder feed, v is scan rate, and Δz is the layer height.

| **Material** | **P (W)** | **m′ (g/min)** | **v (mm/min)** | **Overlap (%)** | **Δz (mm)** |
|---|---|---|---|---|---|
| **H13** | 2000 | 12 | 1000 | 50 | 0.9 |
| **Ferro55** | 2000 | 12 | 1000 | 45 | 0.7 |
| **Osprey® 18Ni300** | 1800 | 14 | 1200 | 55 | 0.8 |
| Osprey **® MAR-60HRC** | 1700 | 14 | 1300 | 55 | 0.8 |

An example of the workflow for processing parameter development for Osprey® MAR-60HRC is presented in Figure 3-5.

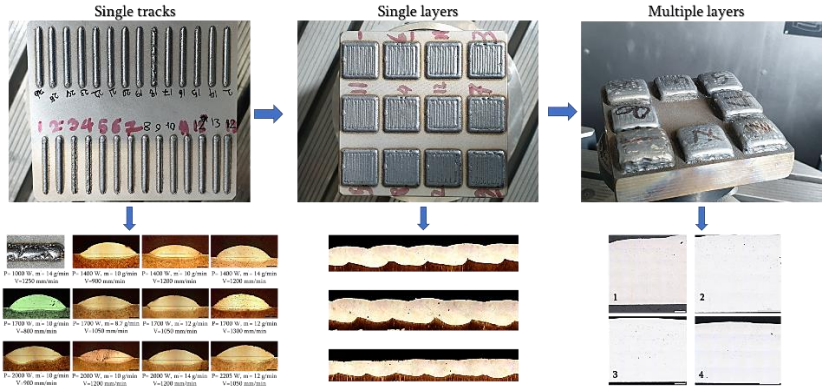


Figure 3-5 examples of workflow for process development for Osprey® MAR-60HRC

For dilatometry and heat treatment experiments, cuboids of 40×30×25mm were deposited for each material, and specimens were extracted from them. For fracture toughness specimens cuboids of 60×45×20 mm were deposited while for the Charpy impact test a block of 100×60×60 mm was prepared. In all cases, due to the difference in baseplate material and the depositions, specimens were cut 5 mm away from the baseplate.

## 3.3 Heat treatments

### 3.3.1 Dilatometry

Dilatometric investigations were carried out utilizing a quenching dilatometer (BÄHR DIL 805A/D, Germany) equipped with an induction heating system (max 100 ˚C /min) with a resolution of 0.01 µm/0.05˚C. Measurements were carried out on standard cylindrical dilatometric specimens $\emptyset 4 \times 10$mm. Specimens were cut out using wire-cut electro-discharge machining (W-EDM). To minimize the effect of height on the inhomogeneity of microstructure due to different thermal histories, cuts were made transversally concerning the build direction. The curves were differentiated with respect to temperature to highlight better the phenomena that occur during heating: $d(\Delta\%)/dT = \Delta(\Delta L/L_0)/\Delta T$, where $L_0$ is the initial length, and ΔL and ΔT are the absolute change in length and temperature, respectively. The curves were smoothed using the LOESS method [151].

### 3.3.2 Austenitization

A set of experiments was performed to obtain the optimum austenitization condition to obtain a homogenized microstructure with the recovery of micro-segregation and partial dissolution of primary carbides. Experiments were conducted using a quenching dilatometer (BÄHR DIL 805A/D). Austenitization temperature was varied between 1020-1100 ˚C for holding times from 15 to 40 minutes under a vacuum atmosphere. Samples were vacuum quenched using 5 bar Argon. The heating and cooling rates for these experiments were 13 ˚C/min and 40 ˚C/min, respectively.

### 3.3.3 Tempering

Tempering was performed on both as-built and quenched specimens, and the specimens are referred to as DT (directly tempered) and QT (quenched and tempered), followed by the tempering temperature (e.g., DT-500˚C) throughout this document. Experiments were performed using the DIL 805 dilatometer in Ar atmosphere. Specimens were tempered twice at temperatures ranging from 450˚C to 700˚C for 2h. The heating rate was set to 12 ˚C /min, while a cooling rate of 30 ˚C /min was utilized. A summary of the heat treatment strategies and the relative acronyms are presented in Figure 3-6.

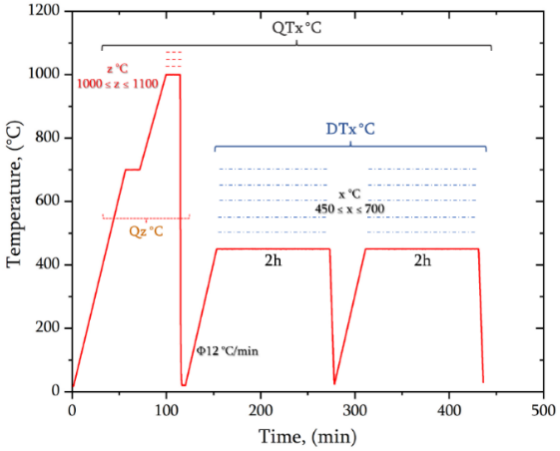


Figure 3-6 Summary of heat treatment strategies and the relative acronyms.

Cryogenic treatment was carried out by immersing the sample in liquid nitrogen (–196 ℃) for 4 h. This sample was then tempered at 600 ℃. A summary of all the

acronyms used throughout this document for the heat treated specimens and their descriptions are presented in Table 3-3.

Table 3-3 Summary of acronyms used for heat treated specimens

| Code | Description |
|---|---|
| **AB** | As-built |
| **CT** | Cryogenic treated |
| **CTT** | Cryogenic treated and tempered |
| **QTx˚C** | Quenched and tempered at x ˚C |
| **DTx˚C** | Directly tempered AB at x ˚C |
| **Q z˚C** | Quenched after austenitization at z ˚C |

### 3.3.4 Aging

Aging treatments to obtain aging curves for the LDED Osprey® MAR-60HRC and Osprey® 18Ni300 were carried out in a BAHR DIL850 A/D dilatometer in an Argon atmosphere. The aging curves correspond to the direct aging of the as-built specimens. Specimens were age hardened at temperatures from 480-600 ˚C and for the time span of 1min to 17h. The aging temperatures were selected based on the dilatometric studies on the materials (precipitation temperatures) and literature review[96]. Aging treatments of the fracture toughness specimens were carried out in an L75 Platinum LINSEIS dilatometer in an Argon atmosphere. Another set of specimens was also prepared by aging the specimens after a solution annealing treatment (at 1020˚C-60 min, followed by air-cooling to room temperature).

### 3.3.5 Tempering resistance

For evaluating the tempering resistance, two sets of specimens were prepared to obtain equal initial hardness values of 500 HV1 and 420 HV1 for each of the heat treatment strategies (QT and DT). These hardness levels are the most recommended values for H13 tool steel in its intended applications (e.g., Al high-pressure die casting dies, tool holders, forging, and extrusion dies). Specimens are coded with the heat treatment strategy followed by the initial hardness, e.g., DT500HV. Specimens were placed in a muffle furnace at 600˚C/650˚C, and hardness measurements were undertaken after soaking for 1, 5, 20, and 40 hours.

## 3.4 Materials characterizations

### 3.4.1 Microstructural analysis

Deposited specimens were cut along the building direction using W-EDM. To eliminate the effect of EDM on the microstructure, a thickness of 300 microns was ground away. Standard metallographic preparations were performed subsequently on the cross-sections by grinding samples using sand papers up to 2000 grit, followed by polishing with the diamond paste of 3μ and 1μ. An extra preparation step of polishing with oxide polishing suspension (OPS) was conducted on specimens for scanning electron microscopy (SEM) and electron backscatter diffraction (EBSD). EBSD combined with electron dispersive x-ray spectroscopy (EDS) elemental mapping was carried out using a Symmetry EBSD detector on a Field Emission Gun Scanning Electron Microscopy (FE-SEM, Zeiss Sigma, Germany) on oxide-polished cross-sections to investigate the phase constitutions and semi-quantitative elemental analysis, respectively. For microstructural analysis, samples were etched using Villella's reagent (1g picric acid, 100 ml ethanol, and 5 ml HCl) or Nital (2% nitric acid in ethanol solution).

### 3.4.2 Density measurements

Density measurements were performed using Archimedes principle and according to ASTM B962-08. Three pieces from different locations of each specimen were cut and measured for each material.

### 3.4.3 Hardness measurements

Microhardness measurements were performed utilizing an FM310 (FUTURE-TECH CORP., Japan) on metallographic cross-sections and according to ASTM E92-17, using a load of 1kg and dwell time of 10s.

### 3.4.4 X-ray diffraction

An Italstructures IPD3000 apparatus equipped with a Co anode source (line focus, $K_\alpha$=0.17889 nm). An Inel CPS120 detector was used to collect diffraction patterns across the omega +120° two-theta range on specimens positioned in reflection geometry with a fixed omega angle and applying an acquisition time of 1800s. Subsequently, MAUD (Materials Analysis Using Diffraction) software[152] was used to elaborate the data using the Rietveld method.

### 3.4.5 Impact toughness

Charpy V-notch (CVN) specimens ($55 \times 10 \times 10\ mm^3$) were cut out of cuboid using W-EDM for evaluating the impact toughness following ASTM E23-16 standard. Moreover, the notch (a=2mm, $\rho$=0.25mm) was introduced in the samples by EDM. It is known that W-EDM cutting can introduce tensile residual stresses in the part. This residual stress is affected by the material and cutting parameters[153]. Kruth & Bleys [154] measured a maximum tensile residual stress in order of 400 $N/mm^2$ at a depth of 100 microns for tool steels, but they demonstrated that by increasing the number of finishing steps the residual stress becomes much lower and limited to a smaller depth. Moreover, it is known that grit blasting can introduce compressive residual stresses on the substrate that mainly depends on the substrate material, grit size, and blasting parameters (pressure impingement angle, gun distance, time) and can be in the order of a few hundred MPa and a profile depth of few hundred microns. [155], [156]. Guilemany et. al demonstrated that reducing the blasting angle and increasing the time resulted in a decrease in residual compressive stresses on the surface of tool steel[152].

Therefore, for introducing the notch in the Charpy specimens two extra finishing steps were applied. Additionally, samples were grit blasted for 90 s with at a 45° angle with respect to the notch surface. Therefore, not only the white layer on the surface was removed, but it was also tried to minimize and compensate for the effect of tensile residual stresses introduced by sand W-EDM through grit blasting. Figure 3-7 presents the cross-section of a W-EDMed surface before and after grit blasting.

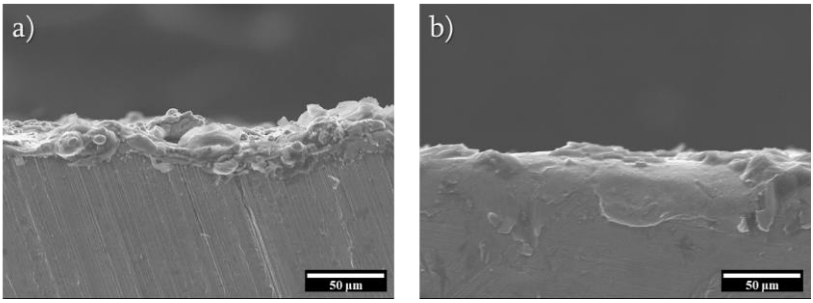


Figure 3-7 Cross section of a specimen after W-EDM a) before and b) after grit blasting.

### 3.4.6 Fracture toughness

Single-edge notched bend (SENB) specimens ($6 \times 3 \times 30\ mm^3$) were cut out of the cuboids using W-EDM to evaluate the fracture toughness for each heat treatment

scenario. Moreover, the notch (a /w= 0.5, $\rho = 90\ \mu m$) was introduced in the samples by EDM. Plane strain fracture toughness testing was performed using 3-point bending tests were under stroke control at a rate of 0.5 mm·min$^{-1}$ using a 1343 Instron machine equipped with a 5 kN load cell. W-EDM may affect the microstructure in the vicinity of the crack tip, especially due to the development of a heat affected zone (HAZ). The same measurements described in section 3.4.5 were applied to minimize these effects. It should also be noted that fracture toughness data obtained in this thesis are only used to compare the toughness of the different samples, which have all undergone identical EDM processes.

### 3.4.7 Compressive Strength

Compression tests were performed using a quenching and deformation dilatometry (BÄHR DIL 805A/D, Germany) equipped with a 20 kN load cell. Sub-size specimens of Ø2.5×5mm were used to achieve the necessary high stresses for the experiments with the equipped load cell. Specimens were cut out of deposited cubes using EDM). The strain rate was set to 0.005/s. In order to prevent damage to deformation rods and for the machine's safety, deformation was limited to 5% true strain for the aged specimens.

## 3.5 Simulations

### 3.5.1 Thermodynamic simulations

Thermodynamic simulations were conducted by Thermocalc software and using the TCFE11 database. Using the Scheil model for simulating the non-equilibrium solidifications, the primary phase for solidification was set to austenite since no trace of delta ferrite was observed in microstructural analysis, neither in Osprey® H13 nor in Fe55.

### 3.5.2 Thermal history simulations

Simulations of thermal history were performed using SIMUFACT Welding MSC software (Simufact Engineering GmbH, Germany). The laser efficiency parameter (i.e., the fraction of the nominal laser power considered for heat input calculations to take into account losses due to reflection, fume, etc.) was set to 0.5 based on experimental measurements, and the gaussian distribution parameter for the laser was set to zero to simulate top-hat beam profile. Moreover, the convective heat transfer coefficient for the deposition material and baseplate was set to 30 and 20 W/(m$^2$K), respectively. A K-Type thermocouple was fixed in a hole drilled 5mm below the surface of the substrate to measure the base-plate temperature and the results were compared to simulation values of the same position for validation.

# Chapter 4

# Results and discussions

Parts of this section have been published in:

[1] S. Amirabdollahian, F. Deirmina, M. Pellizzari, P. Bosetti, and A. Molinari, "Tempering behavior of a direct laser deposited hot work tool steel: Influence of quenching on secondary hardening and microstructure," Mater. Sci. Eng. A, vol. 814, p. 141126, May 2021, doi: 10.1016/j.msea.2021.141126.

[2] S. Amirabdollahian, F. Deirmina, L. Harris, R. Siriki, M. Pellizzari, P. Bosetti, A. Molinari, "Towards controlling intrinsic heat treatment of maraging steel during laser directed energy deposition," Scr. Mater., vol. 201, p. 113973, Aug. 2021, doi: 10.1016/j.scriptamat.2021.113973.

[3] S. Amirabdollahian, F. Deirmina, M. Pellizzari, A. Molinari, and P. Bosetti, "Heat Treatment Behavior of a Hot Work Tool Steel Produced through Direct Laser Metal Deposition," in Proceedings of EuroPM 2020 Virtual Congress, Oct. 2020.

[4] S. Amirabdollahian, F. Deirmina, M. Pellizzari, P. Bosetti, M. Benedetti, and A. Molinari, "The effect of different post-processing thermal treatments on the mechanical properties and tempering resistance of additively manufactured H13 hot work tool steel," in Proceedings of Tooling 2022, Orebro, Sweden, Apr. 2022.

[5] S. Amirabdollahian, M. Perini, T. Tekin, P. Bosetti, and A. Molinari, "Characterization and Heat Treatment of an Additively Manufactured Tool Steel Fabricated by Laser Directed Energy Deposition," in Proceedings of Tooling 2022, Orebro, Sweden, Apr. 2022.

# Part 1- Carbon containing tool steels

## 4.1 AISI H13 tool steel

### 4.1.1 As-built microstructure of the LDED H13

The as-built microstructure of LDED Osprey® H13 is a layered structure composed of rather large melt pools in the millimeter range, as is typical of DED methods. The optical micrograph at low magnification shows melt pool structures along the build direction (Figure 4-1. a). As depicted in Figure 4-1. b, using Vilella's reagent, it was possible to highlight the large columnar PAG morphology traversing the melt pools.

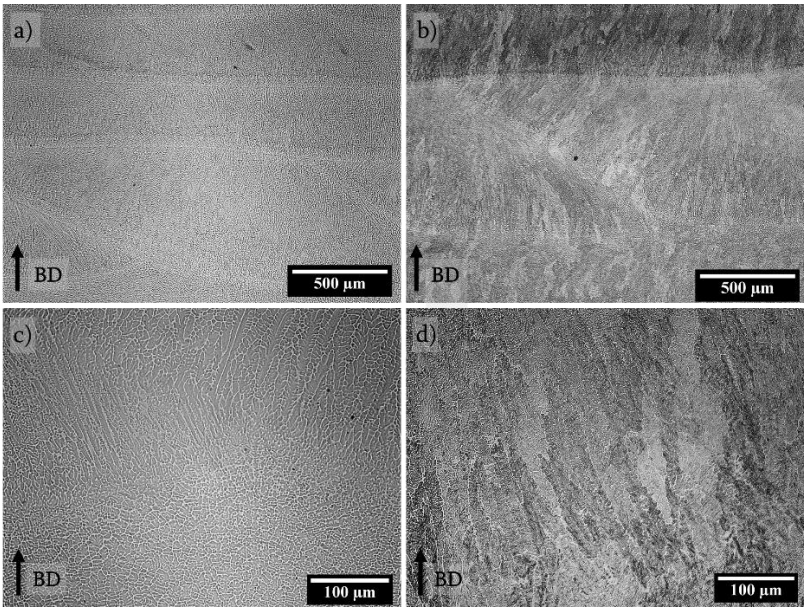


Figure 4-1. An illustration of the AB microstructure of LDED Osprey® H13. Low magnification LOM of the cross-section a) using Nital 2%, b) using Vilella's reagent to show columnar PAG. Higher magnification LOM, revealing c) the cellular/dendritic solidification (Nital 2%), d) the columnar grain morphology (Vilella's reagent).

The dendritic/cellular structure can be observed clearly inside the melt pools, and the growth direction of dendrites is normal to the solid-liquid front and opposite to the local predominant heat flow direction at melt-pool boundaries (Figure 4-1c). A higher magnification view of the large columnar grain morphology is presented in Figure 4-1.d.

The SEM micrographs in Figure 4-2 clearly highlight the inter-cellular and inter-dendritic areas. Inside the inter-cellular areas, particles with a size of 0.5-3 μm were evident (marked by arrows). These features were common in samples extracted from the middle and topmost regions of the as-built part.

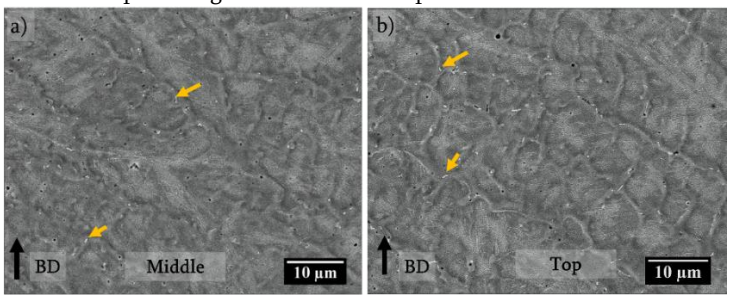


Figure 4-2. SEM micrographs highlighting the presence of particles on the cellular boundaries in specimens extracted from a) middle and b) top of a sample.

EDS elemental mapping corresponding to the backscatter electron (BSE) micrograph shows the enrichment of alloying elements at the cell boundaries, indicative of the heavy micro-segregation of alloying elements caused by the fast non-equilibrium solidification, and lath martensite microstructure and some bainite shaves are evident within the matrix in BSE micrograph (Figure 4-3 a-f).

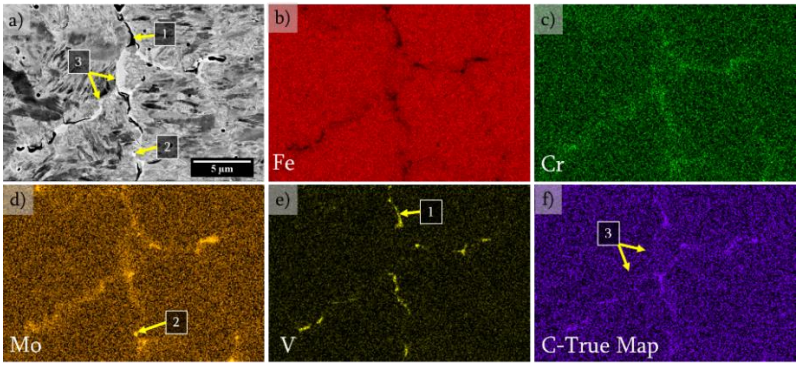


Figure 4-3. a) BSE micrograph of AB sample highlighting cell boundaries and corresponding EDS elemental mapping for b) Fe, c) Cr, d) Mo, e) V, and f) C (true map)

Three distinct regions marked by numbers at the cell boundaries could be revealed by EDS spot analysis. V-rich particles (marked as 1 in Figure 4-3e) were characterized as V(C, N) carbonitrides (Figure 4-3a and Table 4-1 EDS spot analysis

results on points 1, 2, and 3 in Figure 4-3 and Figure 4-4). The high nitrogen content in V(C, N) in some works has been related to the nitrogen pick-up during the LDED process[157]. To verify this, an analysis of interstitial elements N and O were performed on the powder and the as-built material. The initial powder contained 0.037 wt.% O and 0.052 wt.% N, while for the as-built material, the values were 0.045 wt.% and 0.053 wt.%, respectively. Considering the identical values for the powder and the deposited part, no nitrogen pick-up is assumable during the deposition and the quite high amount of N in the powder is probably due to the storage condition of the powder. Particles marked as number 2 were richer in Mo (Figure 4-3d). A higher magnification BSE micrograph showed that those particles consisted of two different phases (Figure 4-4b). The EDS spot analysis (Table 4-1 EDS spot analysis results on points 1, 2, and 3 in Figure 4-3 and Figure 4-4) revealed that the darker phase (i.e., 2-1) was rich in Cr, Mo, and V (i.e., 25.5, 8.8, and 3.8wt.%, respectively). If the at.% of carbon is considered, it can be concluded that these particles are $M_7C_3$ type carbides. On the other hand, the brighter particles (2-2) were heavily enriched in Mo (i.e., 29.1 wt.%) with a lower concentration of Cr (i.e., 12.7 wt.%) compared with that of (2-1) (Table 4-1 EDS spot analysis results on points 1, 2, and 3 in Figure 4-3 and Figure 4-4). These particles can be characterized as $M_6C$ type carbides, although given the small size of the particles, the conclusions shall be further validated by transmission electron microscopy (TEM). It can be postulated that Mo-rich carbides precipitated first at the inter-dendritic / intercellular areas. Consequently, due to the depletion of Mo at the vicinity of these carbides, Cr-rich carbides preferentially precipitated at the $M_6C$/micro-segregation interface. The size of the observed carbides is in the range of 0.5-3 μm, implying that they should have precipitated either during the solidification or at lower temperatures, in the solid state, as a result of thermal cycling due to the deposition of successive layers.

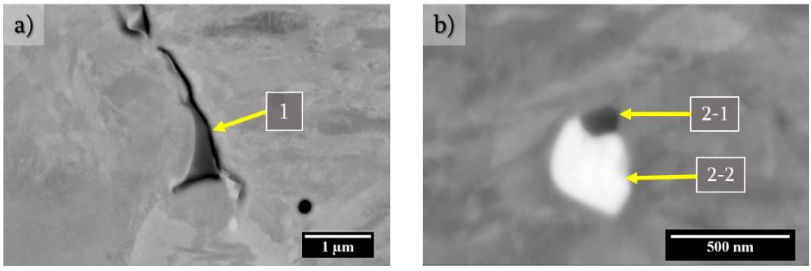


Figure 4-4 Higher magnification micrographs of carbides in Fig. 4.3, a) region 1 showing V(C, N) and b) region 2 showing Cr rich (2-1) and Mo rich (2-2) carbides

Table 4-1 EDS spot analysis results on points 1, 2, and 3 in Figure 4-3 and Figure 4-4

| | Spot 1 | | Spot 2-1 | | Spot 2-2 | | Spot 3 | | Matrix |
|---|---|---|---|---|---|---|---|---|---|
| | Wt.% | At.% | Wt.% | At.% | Wt.% | At.% | Wt.% | At.% | Wt.% |
| **C** | - | 21.0 | - | 22.8 | | 21.2 | - | - | - |
| **N** | 5.6 | 15.8 | - | - | - | - | - | - | - |
| **Si** | 0.7 | 1.0 | 0.6 | 1.0 | 1.2 | 2.1 | 0.9 | 1.7 | 0.8 |
| **V** | 29.0 | 22.5 | 3.8 | 3.5 | 3.2 | 3.2 | 2.0 | 2.0 | 0.9 |
| **Cr** | 9.7 | 7.4 | 25.5 | 22.6 | 12.7 | 12.4 | 8.2 | 8.0 | 5.0 |
| **Mo** | 7.4 | 3.1 | 8.8 | 4.1 | 29.1 | 15.5 | 5.0 | 2.7 | 1.4 |
| **Fe** | 41.2 | 29.2 | 54.9 | 45.3 | 47.3 | 43.1 | 81.1 | 73.9 | 89.5 |

However, the second hypothesis seems to be unlikely since coarse carbides were found in the topmost areas as well, which did not experience thermal cycling (see Figure 4-1c-d). Finally, region 3, appearing brighter than the matrix, was characterized by a high concentration of alloying elements (i.e., Cr, Mo, and V) (Table 4-1); however, Carbon concentration was significantly lower than those of carbides, which can also be appreciated qualitatively from elemental mapping in Figure 4-3f, and therefore these regions can be characterized as RA (Table 4-1).

EBSD analysis highlights that RA islands are preferentially located at the cellular/dendritic boundaries (Figure 4-5). These results are in line with the microstructural observations in Figure 4-3.

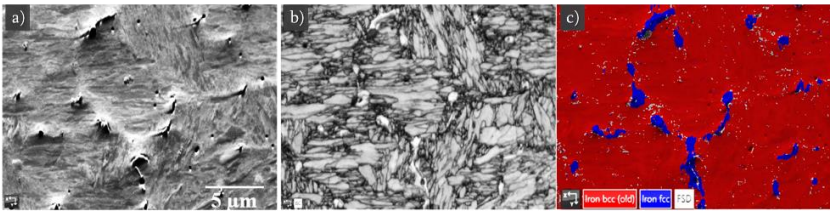

Figure 4-5 EBSD analysis results on AB sample, a) fore-scatter (FSD) microstructure image revealing a cell boundary, b) corresponding band contrast image, and c) phase map, martensite (red), austenite (blue)

Calculations of the non-equilibrium solidification were carried out using the Scheil model (Figure 4-6a), involving complete diffusion in the liquid while no diffusion

in solid material. The primary solid phase, in this case, was set to austenite (FCC) instead of delta ferrite as no traces of delta ferrite were evident in the AB microstructure. The simulation predicts the formation of $M_6C$, followed by the $M_7C_3$ and finally MC-eta type carbides precipitation, where MC-eta represents MC carbides rich in V and Mo, at the end of solidification. The composition of these carbides at the end of solidification (i.e., 0.99 mole fraction of solid) is listed in Table 4-2. The results are fairly in agreement with those of experimental data (Table 4-1). However, it should be noted that due to nitrogen pick-up during deposition, MC-type carbides are expected to be replaced by M(C, N) carbonitrides. Moreover, one has to note that the experimental EDS spot analysis data represents a larger interaction volume, especially in the case of fine carbides, which might include the data collected from the surrounding matrix. The micro-segregation of alloying elements resulting from non-equilibrium solidification (Figure 4-6b) is also responsible for the chemical stabilization of RA at the cellular/dendritic boundaries because of lowering the martensite start (Ms) and Martensite finish (Mf) temperatures.

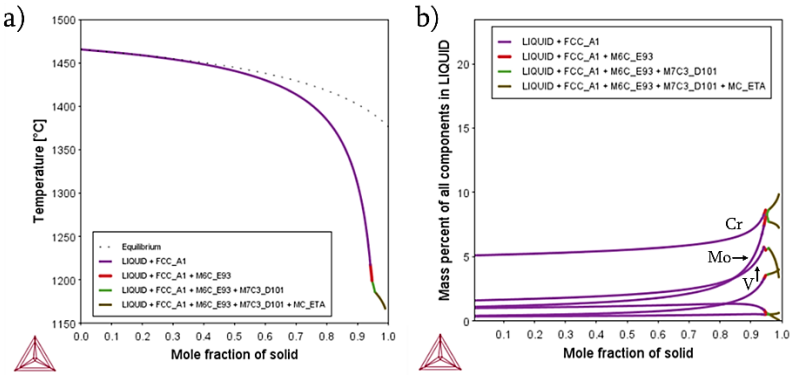


Figure 4-6 a) Mole fraction of solid vs. temperature and b) mass fraction of alloying elements in liquid vs. mole fraction of solid calculated using the Scheil model

To simulate the Ms temperature of the micro-segregated regions, firstly, the vol.% of the micro-segregated areas was estimated by performing image analysis on five SEM micrographs (see Figure 4-6a). The microstructure contained around 12±1 vol.% of micro-segregated regions with the exclusion of carbides (green areas in Figure 4-7a). Afterward, the average composition of the last 12 mol% of liquid to solidify up to the point at which carbides start to form (i.e., 0.85 to ~0.97 mole fraction in Figure 4-7b) was considered in the Scheil simulations. In these

calculations, an austenite grain size of 5μm was employed. As depicted in Figure 4-7b, the Ms temperature of micro-segregated regions can be as low as 40°C, and the transformation cannot be completed even at liquid Nitrogen temperature (-196°C). The nominal martensite fractions of H13 (i.e., matrix) vs. temperature is also depicted for comparison.

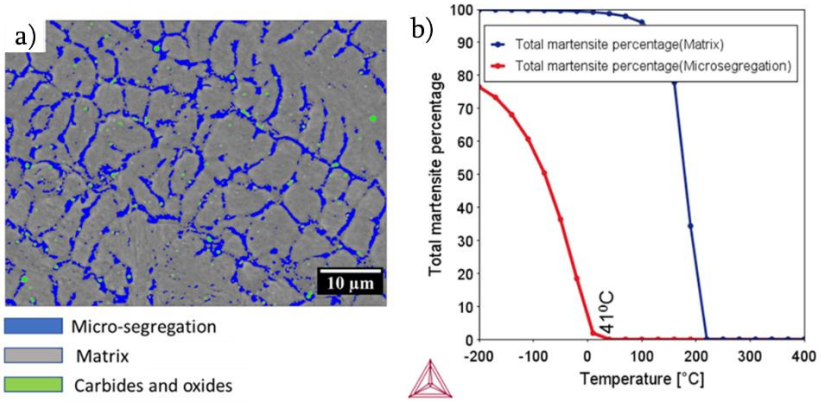


Figure 4-7 a)Image analysis revealing the area fraction of cellular boundaries and b) Ms and martensite fraction modeling: micro-segregated regions vs. nominal Osprey Osprey® H13 composition

Table 4-2 Carbides chemical composition calculated by Scheil model

| | $M_6C$ | | $M_7C_3$ | | MC-ETA | |
|---|---|---|---|---|---|---|
| | Wt.% | Mole% | Wt.% | Mole% | Wt.% | Mole% |
| **C** | 2.8 | 14.3 | 8.6 | 30.0 | 15.6 | 49.3 |
| **Si** | 1.0 | 2.1 | - | - | - | - |
| **V** | 5.8 | 6.8 | 18.2 | 13.0 | 49.7 | 36.9 |
| **Cr** | 2.8 | 3.3 | 30.3 | 26.8 | - | - |
| **Mo** | 48.0 | 30.3 | 3.6 | 2.6 | 34.6 | 13.7 |
| **Fe** | Bal. | Bal. | Bal. | Bal. | Bal. | Bal. |

XRD analysis evidenced ~10 vol.% RA in as-built steel (Figure 4-8), which is fairly in line with the area fraction of the micro-segregation at the inter-dendritic regions (i.e., 12±2%). A cryogenic treatment (CT) at -196°C on the AB sample led to a partial transformation of RA to martensite (i.e., ≤ 4 vol.% vs. 10 vol.% RA in AB). This is

in good agreement with the predicted values in Figure 4-7b. It should be noted that below 2 vol.% RA is expected in the absence of micro-segregation in an austenitized and quenched Osprey® H13.

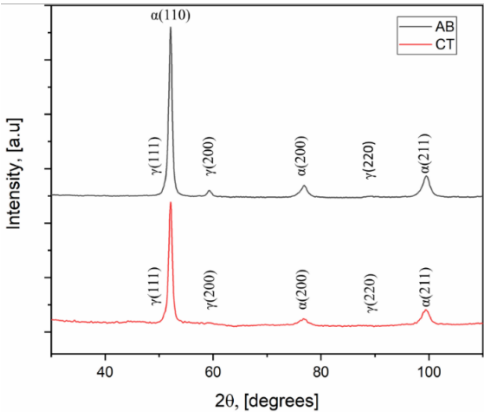


Figure 4-8 XRD diffraction patterns collected from AB sample before and after cryogenic treatment

### 4.1.2 Hardness profiles: As-built condition

Hardness profiles at the melt pools along the building direction and three different locations at the bottom, middle, and top of the sample are presented in Figure 4-9a-c, respectively.

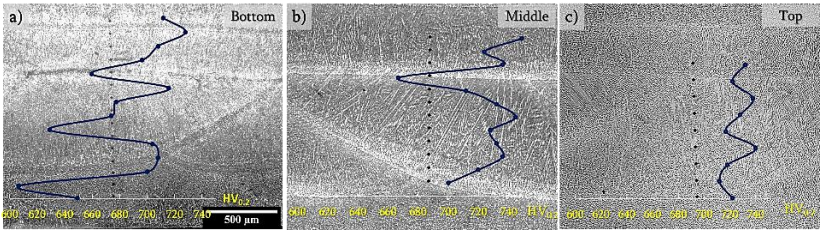


Figure 4-9 Microhardness profile along melt-pools at a) bottom, b) middle and c) top of the specimen

A considerable inhomogeneity of hardness can be observed across the melt pools, which can be attributed to the different cooling rates at their top and bottom positions. It has been demonstrated that the cooling rate (GR) increases from the bottom to the top of the melt pool while G/R values decline in the same direction. Therefore a finer microstructure is expected at the top zone [158]. It is also

noteworthy that the average values for microhardness of the sample at the bottom, middle, and top of the sample's height were 610±6, 665±4, and 730±4 HV0.2, respectively. This can be attributed to the partial tempering of the rapidly solidified martensitic structure in the bottom layers as a result of heat transfer from the above solidifying layers. These features will be discussed further in section 4.1.4, where the tempering behavior of the material is described. The local inhomogeneity of hardness, as well as the non-uniform hardness profile along the build direction, might underline the need for homogenizing the microstructure through post-processing thermal treatments [70].

### 4.1.3 Austenitization and Quenching

#### 4.1.3.1 Austenitization at 1020°C x 20 min

Some previous studies on austenitization and quenching of laser powder bed fusion (LPBF) processed H13 had shown that austenitization at 1020°C for 15-30 min would result in a fine-grained and fully martensitic microstructure. Considering LPBF H13, partial recovery of the solidification structure and achievement of a fully martensitic microstructure with a small vol.% of VC at the prior cell boundaries or prior austenite grain (PAG) boundaries have been documented [70]. The dilatometry curves of quenching experiments for LDED Osprey® H13 showed that the onset of martensitic transformation (i.e., Ms temperature) after quenching from 1020°C for 20 min was around 300°C (Figure 4-10a), which is higher than reported values for LPBF processed H13 (i.e., ~260°C) [70], this difference will be discussed shortly in the current section. The quenched specimen did not contain any RA, and the only detected phase by XRD quantitative phase analysis was martensite (Figure 4-10b). Although peaks pertaining to MC and $M_8C_7$ [159], [160] carbides were observed, quantitative analysis was not successful due to the very low vol.% of these phases.

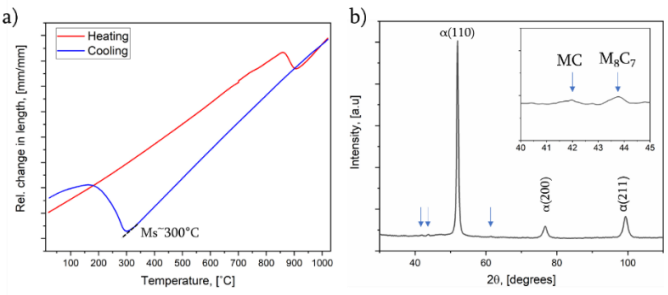


Figure 4-10 a) dilatometry records for austenitization and quenching at 1020°C and b) XRD diffraction pattern of the quenched sample

As shown in Figure 4-11a, the cellular/dendritic structure was still detectable in the quenched sample.

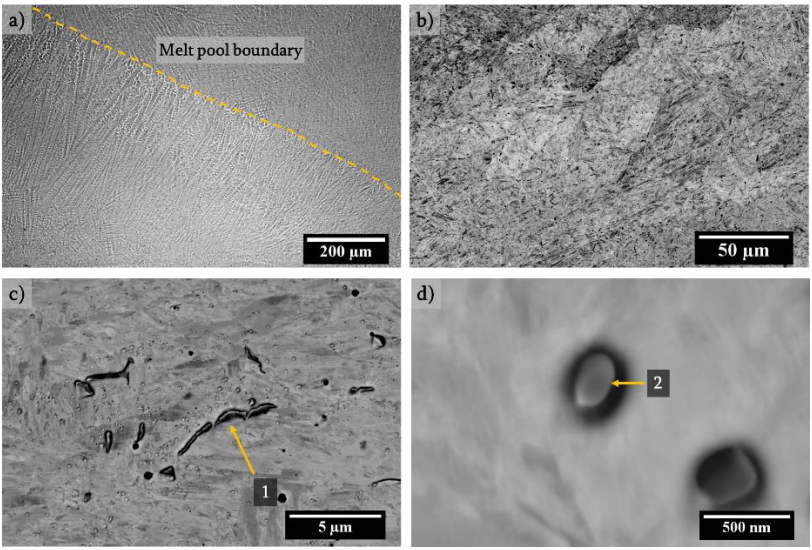


Figure 4-11 a) Optical micrograph of the Q1020°Cx20min, b) BSE, SEM micrograph showing the columnar grain morphology, c) higher magnification BSE micrograph showing the V(C, N) at prior cell boundary and precipitation of fine carbides, and d) higher magnification micrograph showing fine carbides

Columnar prior austenite grains (PAGs), characteristic of the LDED process, were observed at higher magnification SEM micrograph, indicating that the micro-segregations impede recrystallization, and recrystallization was not completed during austenitization (Figure 4-11b). Moreover, a larger number of vanadium-rich carbonitrides containing Mo and Cr were found at the prior cells/dendrites boundaries (Point 1 in Figure 4-11c and Table 4-3), which were slightly larger than those in the AB sample (see Figure 4-3a). Furthermore, precipitation of fine V-rich carbonitrides in the vicinity of coarse carbides was evident (Point 2 in Fig.9d and Table 4-3).

Table 4-3 EDS analysis on particles marked by arrows in Figure 4-11 in at.%

| Spot | C | N | V | Cr | Mo | Fe |
|---|---|---|---|---|---|---|
| 1 | 23.2 | 15.9 | 42.0 | 6.0 | 2.7 | 10.0 |
| 2 | 24.8 | 16.0 | 37.3 | 4.0 | 1.0 | 15.9 |

The microstructural observations and dilatometry records (i.e., high Ms temperature) convey that at least part of the C and alloying elements (e.g., V & Mo) contribute to the precipitation and/or coarsening of the carbides formed upon solidification during soaking at 1020°C. Therefore, the austenite formed at 1020°C contains less carbon and alloying elements in the solid solution leading to an increased Ms temperature recorded by dilatometry. Consequently, the martensite formed upon quenching contains less C and alloying elements in the supersaturated solid solution.

One reason for the different responses to austenitization at 1020°C in LDED and LPBF samples can be related to the presence of the coarse carbonitrides in the AB state in the former, which was not observed in LPBF samples, at least by SEM analysis [70]. This can be either due to the faster cooling rates in the LPBF processing route compared with LDED suppressing carbides growth or the higher nitrogen pick-up in the case of LDED due to the less protective atmosphere. Nitrogen decreases the solubility of the V(C, N) in austenite compared with VC [161]. Since V(C, N) is an equilibrium phase at the austenitization temperature range [162], carbonitrides might grow further during low-temperature austenitization by Ostwald ripening and somehow grain boundary diffusion mechanism [161], [163], [164]. This process is aided by the localized micro-segregation at the cellular boundaries (i.e., RA islands), with a higher concentration of alloying elements than that of nominal H13 composition, acting as preferential sites for the precipitation or growth of carbides. This becomes important during tempering where less available C and alloying elements inside martensite lead to a smaller vol.% of fine secondary carbide precipitates, resulting in lower achievable hardness in the technically significant tempering range (i.e., 575°C to 650°C) and thus lowering the tempering resistance. Moreover, the growth rate of secondary V(C, N) in martensite is much lower than that of VC [165]. Therefore, to exploit the positive effect of the N in V(C, N), the dissolution of V(C, N) during austenitization through diffusional processes is beneficial since it gives rise to the precipitation of extremely fine secondary V(C, N) during tempering, which leads to enhanced strengthening. The tempering behavior will be discussed in detail in section 4.1.4.

#### 4.1.3.2 Optimization of austenitization treatment

Obtaining a homogenized microstructure with the partial recovery of micro-segregation and partial dissolution of the V(C, N) via diffusional process requires higher temperature austenitization treatments for longer times to enhance the diffusivity of micro-segregated elements inside the matrix. For this purpose, austenitization temperatures ranging from 1040 to 1100°C were used, and the

soaking time was extended to 40 min. An additional austenitization treatment at 1200°C for 15 min was also performed (Figure 4-12). The microstructure of the quenched sample after austenitization at 1040°C was significantly different from that of 1020°C (Figure 4-12a). Some newly formed PAGs are evident. However, some columnar grains are still detectable, and traces of micro-segregation resembling the intercellular/inter-dendritic areas still exist and are marked by arrows in the inset. The micro-segregation was mostly recovered at Q1060°C, while grains were slightly larger than the Q1040°C (Figure 4-12b). A full homogenization seems to be achieved at 1100°C, where a fully equiaxed grained but coarser microstructure is achieved (Figure 4-12c). Austenitization at 1200°C resulted in abnormal grain growth (Figure 4-12d). It has been shown that in Osprey® H13, with V: C ratios close to stoichiometric, significant grain growth occurs after the full dissolution of VC, which is responsible for grain pinning at temperatures higher than 1100°C [166]. SEM micrograph at higher magnification (Figure 4-12e) revealed the martensite lath structure within fully equiaxed PAGs in Q1100°C. Coarse V(C, N) were hard to find within the microstructure, and a limited number of Mo and Cr-rich carbides were still detected (Figure 4-12f & Table 4-4), and coarsening of lath martensite is also evident compared with that of Q1020°C (Figure 4-11c).

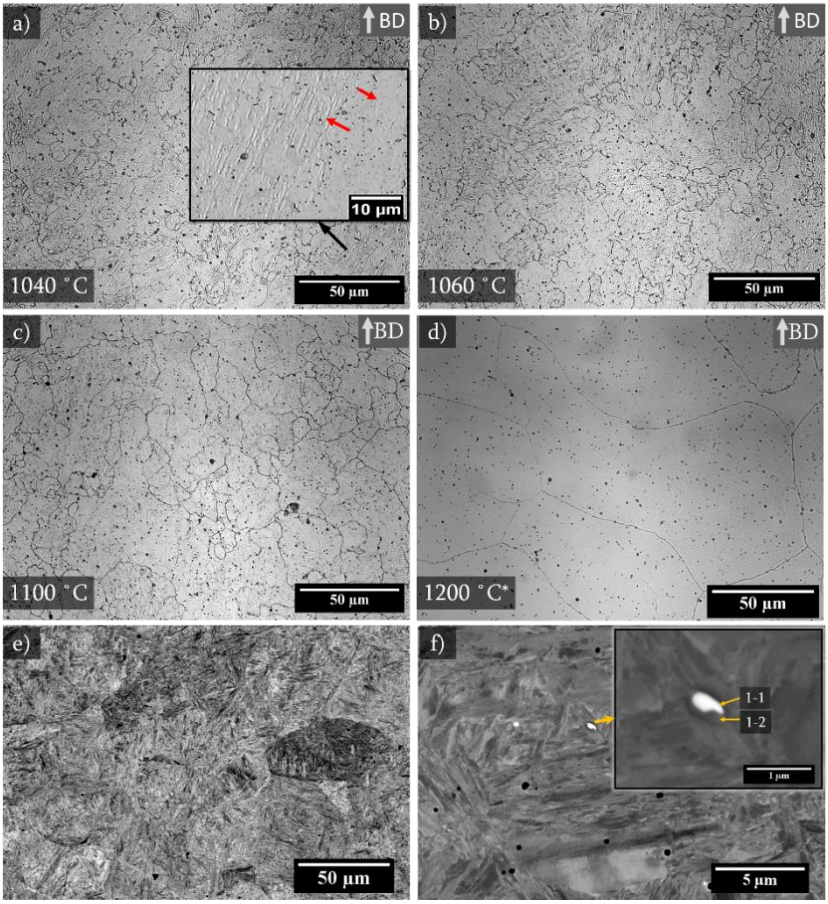


Figure 4-12 Micrographs of samples quenched from different austenitizing temperatures, a) Q1040°Cx40min (OM), b) Q1060°Cx40min (OM), c) Q1100°Cx40min (OM), d) Q1200°Cx15min (OM), e) Q1100°Cx40min (SEM), and f) a higher magnification BSE micrograph (insert showing Mo, Cr-rich carbide)

Table 4-4 EDS analysis results on spots marked by arrows in Fig.10f, in at.%

| Spot | C | Cr | Mo | Fe |
|---|---|---|---|---|
| **1-1** | 23.6 | 8.4 | 22.0 | 44.2 |
| **1-2** | 24.0 | 30.2 | 6.3 | 42.5 |

The experimental Ms temperatures and hardness data (Figure 4-13) indicate that as the austenitization temperature is increased up to 1060°C, the Ms temperature decreases almost linearly while the quenched hardness increases linearly. In comparison to Q1060°C, increasing the austenitization temperature to 1100°C results in an increase in hardness and a negligible drop in Ms. By further increasing the austenitization temperature to 1200°C, no obvious changes in Ms can be observed, and the hardness increase rate diminishes. The noticeable drop in Ms and increased hardness levels can be correlated to the larger amount of C and alloying elements inside parent austenite as a consequence of increasing the austenitization temperature, leading to the dissolution of the carbides observed in AB microstructure as well as recovery of the micro-segregation by diffusion. However, from 1100°C onwards, the counteracting effect of grain growth, which increases the Ms temperature and opposes the increase in the strength (hardness) according to the Hall-Petch relation, becomes evident. This is consistent with microstructural observations and diminishing the pining effect of V(C, N) due to their dissolution.

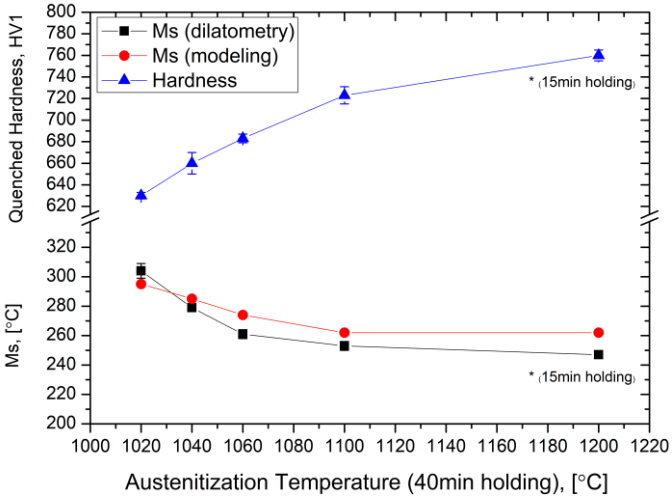


Figure 4-13 Hardness and Ms temperature vs. austenitization temperature

The obtained results are fairly in-line with the Ms simulations carried out by Thermocalc (Figure 4-14).

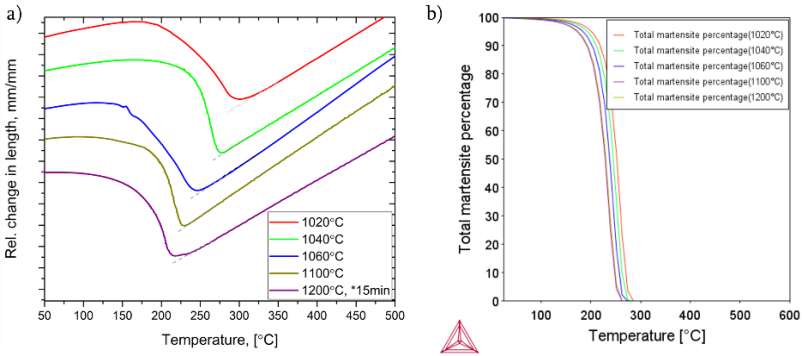


Figure 4-14 a) experimental dilatometry curves of quenching after austenitization at different temperatures, b) corresponding martensite fractions, and Ms temperature modeling results

In these simulations, PAG size was derived from a set of optical micrographs similar to those in Figure 4-12. Moreover, austenite composition in the equilibrium condition at the given austenitization temperature was considered. The alloying content of the equilibrium austenite increases by increasing austenitizing temperature as a result of the dissolution of VC carbides. Since at a given temperature, the equilibrium VC phase (i.e., maximum possible vol.%) is considered to form, Ms temperatures calculated by simulations are slightly higher than those of experimental values, with the exception of austenitization at 1020°C. The reason can be due to the precipitation or growth of a considerable vol.% of carbides from the highly alloyed RA (i.e., micro-segregated areas) or readily precipitated carbides during the solidification process, respectively.

Considering the microstructures, Ms temperatures, and the quenched hardness, it can be concluded that the optimum homogenization might be achieved somewhere between 1060-1100°C. However, since coarse grain size is known to be detrimental to toughness [166], temperatures closer to 1060°C are suggested.

### 4.1.4 Tempering Curves

#### 4.1.4.1 Isothermal Tempering

The tempering curves for DT, Q1020°C-T, and Q1060°C-T specimens are depicted in Figure 4-15. Single hardness data for the CTT, as well as Q1100°C-T, both tempered at 600°C, are also included for comparison.

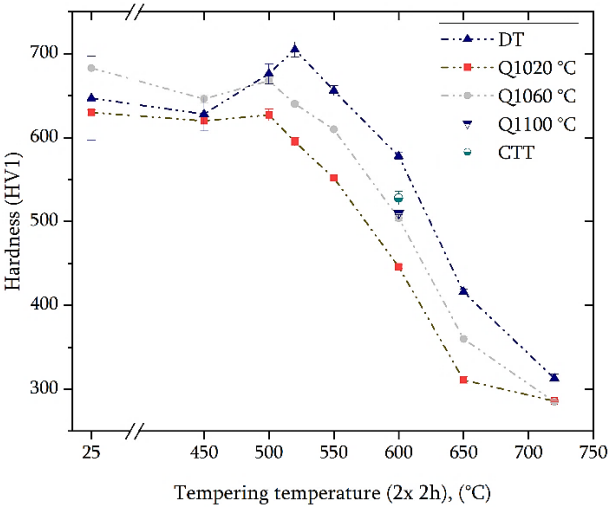


Figure 4-15.Tempering curves for the LDED Osprey® H13 specimens.

The starting hardness of the as-built material extracted from the middle regions of the printed part is around 650 HV1. The AB sample contains up to 10% RA, softer than martensite, and coarse carbides, which reduce the amount of alloying elements in supersaturated martensite. Therefore, the observed high hardness can be attributed to the extremely fine martensite substructure and high dislocation density as a result of rapid solidification [167]. In the case of quenched specimens, as discussed earlier, the starting hardness of Q1060°C (i.e., 685 HV1) is higher than that of Q1020°C (i.e., 630 HV1).

A secondary hardening peak is found at 500°C in both sets of quenched samples, comparable to those reported in the literature for sintered or forged H13[168], [169]. Above the secondary hardening peak temperature, secondary carbides progressively coarsen, and dislocation recovery occurs. This leads to a gradual decrease in hardness [168]. The hardness of Q1060°C-T is systematically higher compared with Q1020°C-T in the whole tempering range except for 720°C. This behavior can be ascribed to the higher C and alloying elements in supersaturated martensite in Q1060°C. The higher available C and alloying elements give rise to a larger number density ($\rho_N$) and vol.% of precipitated carbides during tempering (especially secondary M(C, N)), leading to increased hardness and consequently enhanced tempering resistance. At tempering temperatures over 650°C, the difference between hardness values becomes smaller. This is due to a more pronounced dislocation recovery, coarsening of the martensite lath, and coarsening of the alloy

carbides by Ostwald ripening mechanism [170], [171]. It is worth mentioning that the hardness of the Q1100°C-T (2x2h-600°C) is equal to that of Q1060°C-T in the same tempering scenario. This reinforces the discussions on Ms observations (Figure 4-13), where Ms temperatures were not significantly different in the austenitization range of (1060 to 1200°C). Therefore, given the finer grain size of Q1060°C, which can improve the toughness, it appears that the optimum austenitization temperature and time can be ~1060°C for 40 min, even from a tempering resistance perspective.

The secondary hardening peak in the direct tempering condition is much stronger than those of quenched parts, and the secondary hardening temperature is shifted to higher temperatures (i.e., ~520°C). The tempered hardness of the DT samples in the whole technically significant tempering range is higher than those of quenched and tempered counterparts leading to a significantly enhanced tempering resistance. Hardness approaches those of quenched counterparts at 720°C.

In previous works on LPBF-H13 [67], [70], [167], the increased hardness, stronger secondary hardening peak, and the shift of this peak were attributed to two main factors;

1. Highly alloyed RA ($\gamma^{\uparrow C_{eq}\ wt.\%}$) decomposed to carbides ($K$) and low alloyed austenite ($\gamma^{\downarrow\downarrow C_{eq}\ wt.\%}$) during the 1st cycle of tempering (Eq. 4-1), low alloyed austenite was then transformed to fresh martensite by cooling to room temperature (Eq. 4-2), contributing to the increased hardness of the parts.

$$\gamma^{\uparrow C_{eq}\ wt.\%} \rightarrow \gamma^{\downarrow\downarrow Ceq\ wt.\%} + K \qquad \text{(Eq. 4-1)}$$

$$\gamma^{\downarrow\downarrow C_{eq}\ wt.\%} \rightarrow \alpha' \qquad \text{(Eq. 4-2)}$$

The decomposition of RA and subsequent martensitic transformation in AB samples during the first tempering cycle was also studied with the aid of dilatometry (Figure 4-16a). By increasing the tempering temperature, the Ms temperature increases while the expansion due to martensite transformation decreases. This can be explained by the increasing vol.% of carbide precipitation from RA by increasing the tempering temperature as a result of enhanced diffusivity of the alloying elements causing a larger depletion of C and alloying elements in RA (see Eq. 4-1). Consequently, the transformation shown in $\gamma^{\downarrow\downarrow C_{eq}\ wt.\%} \rightarrow \alpha'$ (Eq. 4-2 takes place at a higher temperature with a lower expansion. It is evident that the austenite decomposition is not completed at 500 and 520°C, so a partial martensitic transformation is possible upon cooling. A full RA decomposition is observed at 720°C, where no more visible expansion upon cooling was evident.

For describing the shift in the secondary hardening peak, Koistinen and Marburger's (K-M) empirical equation (Eq. 4-3) was plotted on semilogarithmic coordinates (Figure 3-5b) [172].

$$V_\gamma = \exp(-1.10 \times 10^{-2}(Ms - Tq)); \; Ms > Tq > -80°C \qquad \text{(Eq. 4-3)}$$

K-M equation correlates the vol.% of retained austenite (Vγ) to Ms and Tq (i.e., the lowest temperature reached during cooling, 20°C in current experiments). It can be observed that the vol.% of RA after the first tempering cycle at 500°C is only around 50% of the initial content (i.e., 5 vs.10 vol%), while at 520 and 550°C, the majority of RA (i.e.,70 and 80 vol.%, respectively) can be transformed to fresh martensite. A full transformation is expected at higher tempering temperatures. By looking at the dilatometry curves (Figure 4-16a), it is evident that the resultant expansion due to martensitic transformation after 520°C tempering is significantly larger than that of 550°C. This simply means fresh martensite formed by cooling from 520°C is more supersaturated in C and alloying elements, which contributes more effectively to the secondary hardness peak during the second tempering cycle.

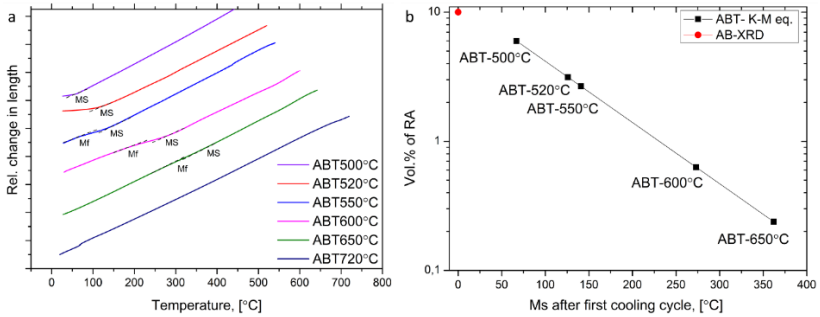


Figure 4-16 a) Cooling curves after the first cycle of tempering (2h-x°C) for DT, $M_f$ (Martensite finish temperature), and b) vol.% of RA calculated by K-M empirical equation after first tempering cycle ( 2h-x°C) for DT

The strengthening effect of RA decomposition during tempering can be recognized better by looking at the tempered hardness of the CTT sample with much lower RA (Figure 4-15). The hardness is lower than that of the DT sample, implying that RA decomposition during tempering contributes to the hardness increase more significantly than that of transformed to martensite by cryogenic treatment before tempering.

2. Enhanced hardness in directly tempered samples was also ascribed to the extremely fine martensite sub-structure and high dislocation density in the AB material. Sub-grain boundaries of the martensite are the major obstacle against the gliding of mobile dislocations [170], [173]. In fact, the sub-grain strengthening is the highest strength component for the tempering range up to 600°C [170]. Moreover, martensite sub-structure boundaries (i.e., lath boundaries) and dislocations pile-ups serve as preferential nucleation sites for secondary carbide precipitation [174]. The larger number of sub-grain boundaries in the directly tempered samples might lead to the larger number density and finer carbide size within the martensitic matrix.

To summarize, in the direct tempering experiments, the decomposition of highly alloyed RA, high dislocation density, and fine martensite substructure significantly enhance the hardness and tempering resistance of LDED- Osprey ® H13 over the quenched and tempered counterparts within the whole technically significant tempering range. The RA decomposition contribution to strength at 600°C tempering scenario can be simply derived by the difference between the hardness of DT (10 vol.% starting RA) and CTT ( ≤ 4 vol.% RA). This value is ~50 HV (i.e., 580 HV vs. 530 HV). On the other hand, at the same tempering temperature (i.e., 600°C), the difference between Q1060°C-T and CTT (i.e., 505 HV and 530 HV, respectively) accounts for the hardening by the high-dislocation density and fine sub-substructure, characteristic of the LDED process. However, this contribution might be somehow underestimated, as the effect of the presence of coarse solidification carbides in the CTT sample and their smaller vol.% in Q1060°C samples is neglected.

#### 4.1.4.2 Tempered Microstructure

At 500°C, the tempered microstructure of the DT sample is characterized by the presence of primary carbides on the prior cellular boundaries, which seem to be intact (arrows in Figure 4-17a). The carbides inside the matrix are extremely fine. At 650°C tempering, the cellular boundaries are replaced by an interconnected network of carbides, another indication for the decomposition of RA, and carbides precipitation within the martensitic matrix is also evident (Figure 4-17b). By increasing the tempering temperature to 720°C, carbides become coarser (Figure 4-17c), in line with the hardness drop observed in Figure 4-15.

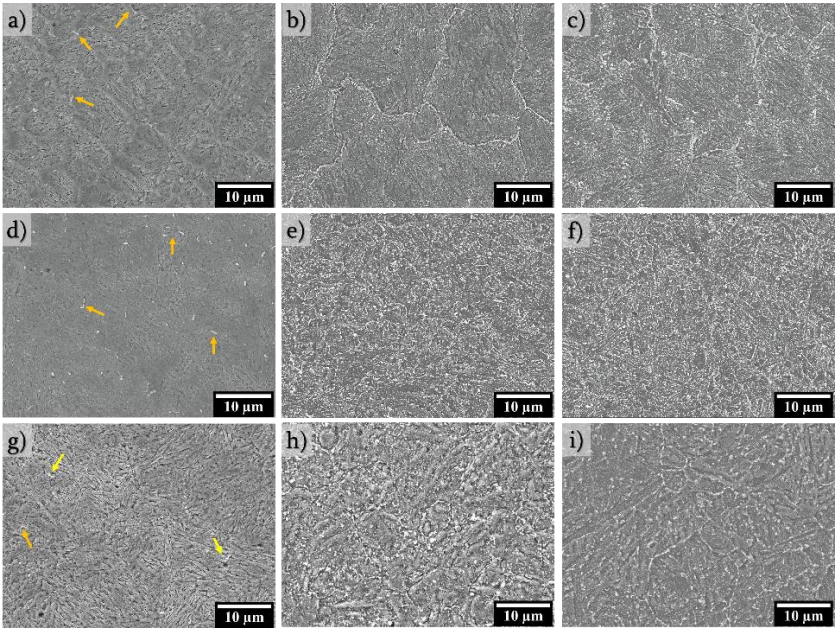


Figure 4-17 SEM micrographs of a) DT-500 °C, b) DT-650 °C, c) DT-720°C, d) Q1020°C-T500°C, e) Q1020°C-T650°C f) Q1020°C-T 720°C, g) Q1060°C-T 500°C, h) Q1060°C-T650°C), and i) Q1060°C-T 720°C

In Q1020°C-T, tempered at 500°C, undissolved solidification carbides on prior cell boundaries are evident (arrows in Figure 4-17d). The size of the solidification carbides did not change compared to the quenched sample. Coarsening of the secondary carbides by increasing the temperature to 650°C is evident (Figure 4-17e). Further coarsening occurred at 720°C temperings (Figure 4-17f). In Q1060°C-T, the number of primary carbides seems to be decreased (arrows in Figure 4-17g). In particular, V(C, N) (white particles in secondary electron micrographs Figure 4-17a, d &g) are dissolved. Carbide coarsening by increasing the tempering temperature is evident (Figure 4-17h-i). Moreover, the martensite substructure is coarser in Q1060°C-T compared with Q1020°C-T because of the higher austenitization temperature. Generally, carbide size within the martensitic matrix is finer in DT samples than in the quenched counterparts (e.g., Figure 4-17b, e & h). This is consistent with hardness measurements and previous discussions on the effect of extremely fine sub-grains on the size of secondary carbide precipitates.

#### 4.1.4.3 Isochronal tempering: Tempering kinetics

In order to better understand the tempering behavior and hardness differences, Isochronal tempering experiments were performed on samples. These curves can give clear indications of the tempering response of the samples with different in-situ as well as post-processing thermal histories (Figure 4-18).

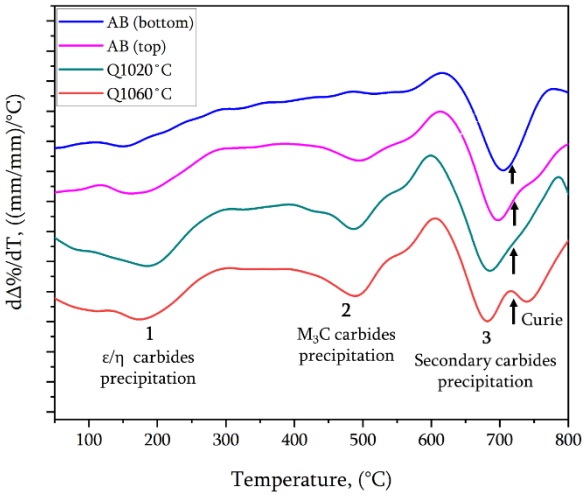


Figure 4-18 isochronal tempering curves (heating rate 15°C/min)

The dilatometry curves during heating of both quenched specimens show an evident contraction (peak 1) between RT and 300°C corresponding to the precipitation of transition carbides (ε/η types) in the first stage of tempering. This is followed by one more contraction (peak 2) between 400 and ~600°C, which is related to the transformation/ precipitation of $M_3C$ carbides in the third stage of tempering [175]. The 3rd and most intense contraction starts at ~620°C. In quenched samples, the 3rd contraction can be representative of the precipitation of secondary alloy carbides from martensite in the fifth stage of tempering (i.e., $M_{23}C_6$, $M_7C_3$, MC, and $M_2C/M_6C$) [67].

Looking at the 3rd contraction for Q1060°C, the isochronal tempering curve clearly shows a peak split. This is the effect of Curie temperature, causing an expansion at ~720°C. The split can also be appreciated in Q1020°C; however, the intensity of the contraction after the Curie point is significantly lower than that of Q1060°C, implying that the 3rd contraction has a higher intensity in Q1060°C.

As elaborated by Theisen and Eser et al. [67], [170], the maximum volume fraction of metastable Mo-rich $M_2C$ (and/or equilibrium $M_6C$) and MC-type Vanadium rich alloy carbides is achieved at a later stage of isothermal tempering range (i.e., 600 and 650°C, respectively). As discussed above, given the considerable vol.% of undissolved coarse carbides & carbonitrides containing V and Mo in Q1020°C, it is reasonable that the intensity of the 3rd carbide precipitation peak in this sample becomes smaller than that of Q1060°C. More precisely, in the Q1020°C sample, less available V and Mo in supersaturated martensite lead to smaller vol.% of M(C, N)-type Vanadium rich secondary carbides. Therefore, the larger peak intensity in Q1060°C can be considered as a representative of a larger vol.% of secondary M(C, N) precipitation. For tempering temperatures of 600 to 650°C, the secondary MC and/or M(C, N), which show the highest resistance to coarsening, have the largest contribution to the overall yield strength and hardness in H13 steel [170]. Therefore, isochronal tempering curves could further explain the origin of the higher tempered hardness of Q1060°C-T in the whole technically significant tempering range.

In the case of the AB sample, extracted from the middle to bottom part of the LDED Osprey® H13 (as-built bottom), the isochronal tempering curve is characterized by a less intense 1st contraction peak. The second peak (peak 2) is missing in this curve, while the 3rd contraction peak is almost identical to those of quenched samples. Similar behavior has been documented on LPBF H13 [70]. The lower intensity of peak 1 and the absence of peak 2 can be discussed, given the multiple thermal cycles LDED Osprey® H13 undergoes during the build process (IHT). It seems that early-stage tempering has been partially accomplished already during the build process as a result of thermal cycling. A recently published research by Zhao et al. [176] clearly demonstrated the in-situ-precipitation of Cr-rich nano-sized carbides (~50nm) and partial tempering of martensite in the middle and bottom layers (i.e., layers subjected to the most intense thermal cycling) in LDED Osprey® H13. One has to distinguish the carbides precipitated by low-temperature intrinsic heat treatment at low temperatures and coarse carbides formed during solidification at the micro-segregated regions of the AB part. The formers are nano-sized and cannot be detected by SEM. The 3rd contraction peak is representative of the secondary alloy carbide precipitations either from martensite or RA in agreement with dilatometric and microstructural studies in sections 3.4.1 & 3.4.2.

Interestingly, the isochronal tempering behavior of the dilatometry sample extracted from the top region of the as-built part (as-built top) shows three distinct peaks similar to those of quenched parts. The top layers of the built sample are the ones that have not experienced successive thermal cycling. This conveys the fact that those areas are only subjected to fast cooling. This can explain the emergence

of low-temperature transformation events during isochronal tempering, which further explains the higher as-built hardness of top parts shown in section 3.2. The 3rd contraction peak is still less intense compared with that of Q1060°C, meaning that coarse solidification carbides exiting in AB microstructure reduce the available C and alloying elements for the precipitation of secondary carbides during tempering. These results highlight that in order to get a uniform hardness profile along the build height after direct tempering, the samples should be tempered above the secondary hardness peak. This can ensure that the entire material is subjected to tempering at a temperature higher than what the bottom and middle layers experience locally during the LDED process. This was clearly confirmed by the previous works on laser powder fusion processed H13 [70].

### 4.1.5 Fracture toughness

Two different tempering scenarios were selected so as to achieve a target hardness of ~500 HV1 for the QT and DT samples. As discussed in the previous section, in order to achieve the same hardness values, the as-built specimens were directly tempered at slightly higher temperatures compared to their quenched counterparts, i.e., at 625°C and 600°C, respectively.

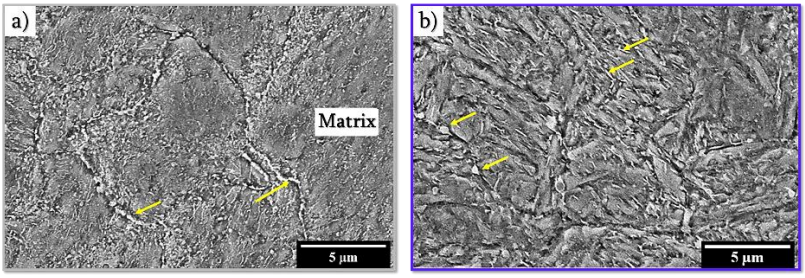


Figure 4-19 SEM micrographs of specimens a) DT-625˚C and b) QT-600˚C

It can be observed that for the DT specimens, RA at the cellular boundaries is decomposed into secondary carbides (arrows in Figure 4-19a). Moreover, the precipitation of secondary carbides within the martensitic matrix is evident. While in the QT specimens, the cellular structure has been eliminated, and the coarse V(C, N) carbides have been dissolved. Upon tempering, the secondary carbides are distributed along the martensite lath boundaries and on the PAGBs (arrows in Figure 4-19b) and are significantly less interconnected than in DT. It can be clearly observed that the tempered martensite microstructure, i.e., the size of laths within the martensitic matrix, is significantly finer in DT samples than that in QT ones.

Results of the fracture toughness test are presented in Table 4-5.

Table 4-5 Hardness and apparent fracture toughness values for the DT and QT specimens

| Sample | Hardness (HV1) | Kapp ($MPa.m^{1/2}$) |
|---|---|---|
| LDED Osprey® H13-DT⊥ | 490 ± 5 | 70 ± 1.8 |
| LDED Osprey® H13-QT⊥ | 491 ± 4 | 89 ± 3.8 |
| LPBF H13 – QT⊥ **[177]** | 460 ± 5 | 67.5 ± 2.8 |
| HIP H13 - QT⊥ **[178]** | 420 ± 1 | 75 ± 1.0 |
| Wrought H13-QT **[179]** | 450 ± 10 | *$K_{IC}$ = 66 |

⊥ Notches perpendicular to the build plate

It shall be mentioned that the notch root radius in the pre-notched samples realized by W-EDM is higher than the standard pre-cracked samples ($\rho \rightarrow 0$), which leads to lower stress concentration at the notch tip and an increased plastic zone radius at the crack tip. Therefore, the critical stress intensity factor is generally higher than that measured for a pre-cracked sample, and an apparent fracture toughness value, $K_{app}$, is reported instead of $K_{IC}$ [177]. It could be proved that the larger the notch tip radius, the higher $K_{app}$ than $K_{IC}$ [180]. The apparent fracture toughness value for DT (70 ± 1.8 $MPa.m^{1/2}$) was smaller than that of QT specimens (89 ± 3.8 $MPa.m^{1/2}$), but it is still comparable to the values for powder metallurgical and LPBF H13, as well as the wrought product and tempered to slightly lower hardness levels.

The crack propagation paths and fracture surfaces are depicted in Figure 4-20.

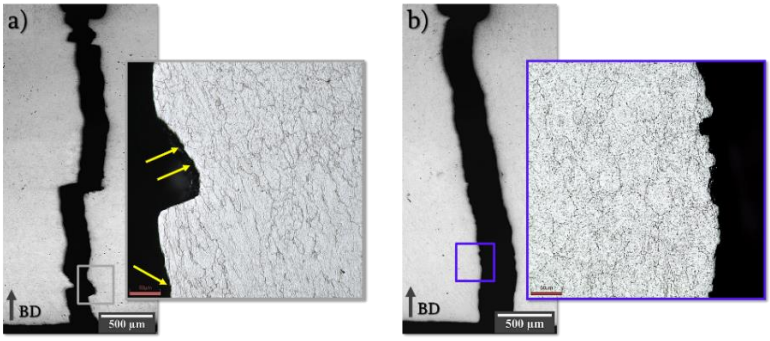


Figure 4-20 LOM images from fracture paths for a) DT and b) QT specimens

The crack propagation in DT is generally trans-granular. However, crack propagation along the cellular/dendritic boundaries is also evident (shown by arrows). The cellular boundaries are hard to distinguish from the PAGs due to the similar response to chemical etching. The intercellular fracture is plausible because the cellular boundaries are characterized by a large density of interconnected networks of carbides that are harder than the matrix, and their coherency with the martensitic matrix reduces by tempering at high temperatures. The dense grain boundary/intercellular precipitation of carbides is the main cause of the lower toughness of DT compared to QT. Moreover, PAGs are elongated parallel to the crack propagation direction in DT samples (Figure 4-20a), and crack propagation may easily occur along this direction without deviations or branching phenomena promoting toughening [5,13]. Whereas in the QT sample, the fracture path seems to be solely dominated by a trans-granular fracture Figure 4-20b). The PAGs are equiaxed because of austenitization treatment leading to recovery and recrystallization.

The fracture surface of DT samples is governed by cleavage facets with just very limited and localized plasticity (see small micro-voids in the inset of Figure 4-21a). Moreover, traces of the fusion line (melt pool boundaries), caused by the partial remelting between two successive layers, were evident in the DT samples and are highlighted by yellow arrows in Figure 4-21a. This could probably cause a crack deflection as observed in fracture path images (Figure 4-20a). In QT samples, the fracture surface indicates a more quasi-cleavage behavior, with the presence of a larger density and finer distribution of dimples on the fracture surface (see inset in Figure 4-21b), which is typical in quenched-and-tempered steels [182].

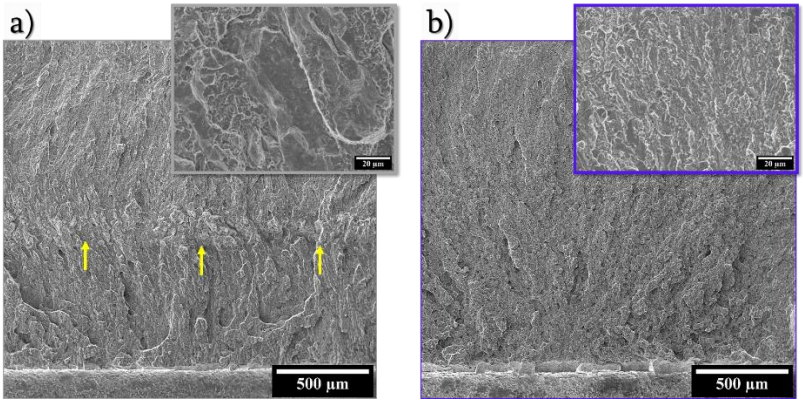


Figure 4-21 SEM images from fracture surfaces for a) DT and b) QT specimens

### 4.1.6 Tempering resistance

The tempering response of the DT and QT samples at 600°C and 650°C are presented in Figure 4-22. As discussed in section 4.1.4, the tempered hardness in DT samples at temperatures higher than the secondary hardening peak is always systematically higher than that of QT samples. Moreover, after the secondary hardening is reached, the difference between the hardness of DT and QT is relatively constant (i.e., ~50 HV) at any tempering temperature. This systematically higher hardness of DT specimens was ascribed to the finer martensite substructure and larger defect density (e.g., dislocations) in rapidly solidified material. These pair of samples (i.e., (DT500 HV, QT500 HV), and (DT420 HV, QT420 HV)), each having the same starting hardness, are tempered well above the secondary hardening temperature (i.e., ≥600°C). The dislocation recovery is almost complete at these temperatures, and the secondary carbides are already precipitated in the tempered martensite matrix. Therefore, any differences in the thermal softening behavior can be theoretically ascribed to the martensite substructure size and resistance to carbide coarsening.

The starting hardness for the samples was ~520 HV1. At 600°C, a substantial drop in hardness to 475 HV1 after 5h is observed for both samples. This is attributed to a drop in dislocation density of the lath martensite in the initial stages of the test [183]. For longer tempering times, the softening rate decreases for both samples, particularly for DT. The hardness of DT decreased to 460 HV1 after 40h, while that of QT to 425 HV1, confirming the higher tempering resistance after direct tempering. Clearly, this result has to be directly correlated to the higher tempering temperature used for DT (625°C) than QT (600°C) and the higher thermal stability induced. At 650°C, the hardness drop in the early stages of tempering is even more pronounced. After merely 1h, the hardness declines from 520 HV1 to around 460 HV1 for both samples. At 5h, the difference in hardness for DT and QT samples becomes more evident. The DT sample (425 HV1) is showing significantly higher temper back resistance compared with QT (~390 HV1). The hardness difference between DT and QT increases up to 20h, then remains constant for longer soaking times: after 40 h, the hardness is 360 HV1 and 300 HV1 for DT and QT, respectively. Hence, the higher tempering resistance of DT can be confirmed even at a rather high temperature, in line with the tempering curves showing that the hardness of the DT remains higher compared with QT up to temperatures exceeding 700°C. At higher temperatures (i.e., 650°C vs. 600°C), the kinetics of dislocation recovery and carbide coarsening are faster. Moreover, except for fine and stable V-rich MC secondary carbides, which are present at both tempering temperatures, at 600°C, needle-like Mo-rich $M_2C$, and Cr-rich $M_7C_3$ have the highest phase fraction among alloy carbides, while at 650°C Cr-rich $M_{23}C_6$, at the expense of $M_7C_3$, is the

prevailing type of carbide, and by increasing the soaking time (i.e., moving towards equilibrium), this transformation becomes even more pronounced [170]. Given the considerably higher coarsening rate of $M_{23}C_6$, their contribution to precipitation hardening becomes less effective, and hence the hardness declines more severely.

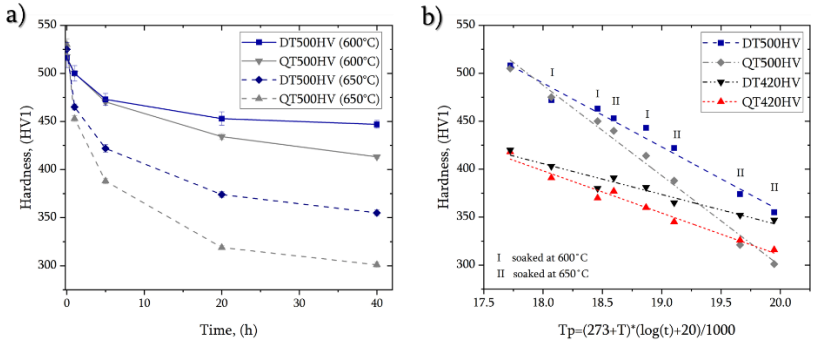


Figure 4-22 a)Tempering resistance as hardness vs. holding time at 600°C and 650°C for DT and QT specimens, b) hardness vs. L-M parameter

One of the most well-known numerical relationships to estimate the hardness of various alloy steels after tempering is the Holloman-Jaffe equation[184] (also generally known as the Larson-Miller equation[185]). The general form of the equation is $T_p = T(logt + C) \times 10^{-3}$, where $T_p$ is tempering parameter, T is temperature (Kelvin), t is tempering time (h) and C is a constant parameter depending on the material, which for low carbon alloy steels ($0.25 \leq \%C \leq 0.4$) is generally considered as 20[186]. By plotting the hardness numbers against the Larsson-Miller parameter and looking at the slope of the fitted lines, it is evident that DT samples systematically show a significantly higher tempering resistance compared to their QT counterparts (Figure 4-22b). For instance, the DT500 HV, after soaking for 40h at 650°C, shows a hardness of ~350 HV1, while this value drops to 301 HV1 for the QT500 HV. This condition holds for the samples with a starting hardness of 420 HV1 as well (i.e., DT420 HV vs. QT420 HV, see the set of data points marked as i). Similar behavior can be observed for the samples soaked at 600°C, up to 40h (i.e., set of data points marked as ii).

It has been demonstrated that tempering temperatures between 500 to 600˚C do not affect the martensite lath size significantly [187]. The governing softening mechanism observed in prolonged soaking times is mostly related to the coarsening/transformation of the fine secondary carbides [183]. This depends on the carbide type and initial carbide size.

Microstructure in DT samples can be divided into two zones (i.e., cell boundaries, and matrix, as shown in Figure 4-23a), while the QT shows a more uniform microstructure.

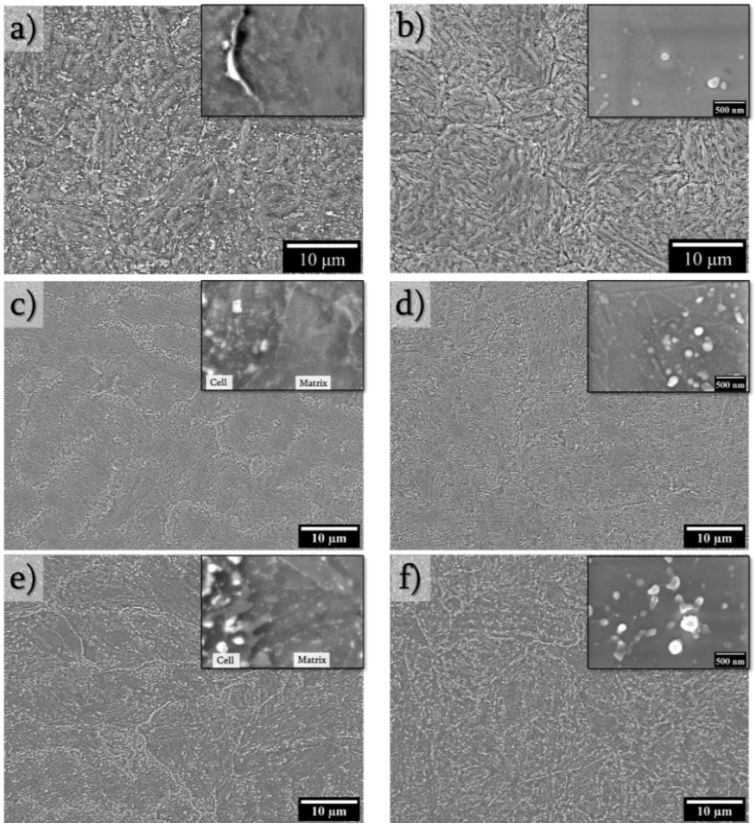


Figure 4-23 Microstructure of the a)DT500 HV, and evolution after 40 h isothermal tempering at c) 600˚C, e) 650˚C; b) microstructure of QT500 HV and evolution after 40h isothermal tempering at d) 600˚C, and f) 650˚C

The presence of V (C, N) carbides is also highlighted in both samples. In the DT sample, the decorated carbides on the prior cell boundaries seem to be interconnected and coarser than those within the matrix. Lath boundaries are known to be the preferred sites for carbide precipitation. Given the finer substructure (lath size) and higher initial dislocation density in DT samples, a finer distribution of small and stable secondary carbides was observed within the matrix

compared with QT counterpart, excluding the ones precipitated on the intercellular boundaries (Figure 4-23c and d, after holding at 600°C, 40h). The situation is more evident at 650°C after 40h (Figure 4-23e and f), where the carbides within the martensitic matrix are finer in DT compared with the QT. Therefore, one probable reason for the better tempering resistance of the DT samples, which is also reflected in the tempering curves (Figure 4-15), can be related to the high initial dislocation density and finer lath size leading to the precipitation of finer secondary carbides in the martensitic matrix by providing a larger number of the energetically favorable sites for their precipitation.

As a remark, it has to be mentioned that the role of Mo-rich carbides and V(C,N), extremely resistant to coarsening, is very significant in terms of thermal softening resistance [166]. The as-built material contained a large number of coarse solidifications V(C, N) on the cellular boundaries (Figure 4-3a). These carbides were partially dissolved during the austenitization treatment (see Figure 4-12f). This leads practically to a larger population of the fine and stable secondary V(C, N) after tempering. The absence of fine vanadium carbonitrides can counteract, at least partially, the positive effect of the fine substructure size in DT. However, a detailed analysis of the carbide type within the martensitic matrix and the ones precipitated on the cellular boundaries is ongoing. The locally higher concentration of alloying elements on the cellular boundaries, due to the microsegregation, might affect the kinetics of carbide precipitation compared with a homogenized material.

Tools in H13 experience high temperatures during service. Examples can be hot forging or die-casting dies. Although the exposure time for some applications may be brief, the cumulative effect over a lengthy period of time throughout service requires the use of materials with enhanced resistance to tempering at elevated temperatures. Given the acceptable fracture toughness measured by DT and its outstanding tempering resistance compared with the QT counterpart, direct tempering is considered a promising and more cost-effective heat treatment schedule for additively manufactured H13 using laser-based technologies. This is further confirmed by the improved thermal fatigue resistance of DT if compared with QT [21].

### 4.1.7 Conclusions

- LDED Osprey ® H13 showed a cellular/dendritic solidification structure. Microstructure comprised martensite, RA (~10 vol.%), primary V(C, N), and Mo, Cr-rich carbides. RA and carbides were found on the intercellular/inter-dendritic areas characterized by a heavy micro-segregation of alloying elements.

- Non-uniform hardness along the building direction was evidenced. This was ascribed to the thermal cycling, causing heat transfer from the solidifying layers to the readily solidified ones leading to the partial uncontrolled tempering of bottom layers (intrinsic heat treatment). This was further supported by isochronal dilatometry tests.
- The conventional heat treatment involving austenitization at 1020°C for 20 min was not suitable for recovery of the micro-segregation and carbides dissolution.
- The redissolution of solidification carbides by high-temperature austenitizing is necessary to improve the precipitation of carbides/carbonitrides and secondary hardening during tempering. Austenitization at 1100°C for 40min allows a near fully homogenized microstructure by the elimination of most of the micro-segregations, the partial dissolution of coarse carbides, and significant grain coarsening. Austenitization at 1060°C for 40 min led to acceptable homogenization of the microstructure, enhanced tempering response, and grain size.
- Maximum hardness within the whole technically significant tempering range was achieved by direct tempering of the as-built material. The secondary hardening peak was shifted to a slightly higher temperature compared with quenched counterparts (i.e., ~520 vs. ~500°C) due to the higher amount of RA, the higher dislocation density, and the finer martensite substructure in AB condition.
- Regarding the tempering results, direct tempering seems to be the most effective post-processing thermal treatment for the LDED Osprey ® H13 from the strength (hardness) perspective and increased temper resistance. However, two aspects should be taken into consideration. Firstly, the interconnected network of hard carbides formed on the prior cellular/dendritic boundaries might be harmful to fracture and impact toughness as well as fatigue strength because they might serve as preferential sites for crack initiation and propagation. Secondly, the inhomogeneous microstructure and non-uniform hardness along the build direction might not be fully recovered by direct tempering. A solution for the latter might be the application of modified deposition strategies to homogenize the effect of thermal cycling across the build height.
- DT samples generally demonstrated higher hardness than QT samples tempered at the same temperature due to the finer martensite substructure and the decomposition of about 12% retained austenite during tempering.
- QT samples show higher fracture toughness in comparison to DT at the same reference hardness (490 HV1). This was attributed to the more homogeneous microstructure and the deteriorative effect of densely

populated secondary carbides on the cellular/dendritic boundaries. Nevertheless, the fracture toughness of the DT samples was still comparable to the wrought H13 after heat treatment.

- Tempering resistance strongly depends on the heat treatment schedule. Direct tempering led to improved tempering resistance due to the contribution of finer martensite substructures leading to a finer distribution of alloy carbides. The lower softening of DT is extended up to 40 h at 650°C.

## 4.2 X35CrMoMn7-2-1 tool steel

PLASweld Ferro55 (X35CrMoMn7-2-1) is a steel grade developed by Voestalpine Böhler, designed initially for hard surfacing by plasma spraying. Recently, some tool manufacturers have suggested the idea of expanding its applications by producing components through LDED due to its better processability compared with some of the well-established tool steels, e.g., H13[188]. To the author's best knowledge, no systematic study on the heat treatment of AM-Ferro55 is available in the literature. In the current section, the microstructure, tempering behavior, mechanical properties, and tempering resistance of this grade are investigated, considering two different heat treatment strategies.

### 4.2.1 Microstructure of LDED Ferro55

The as-built microstructure of samples visualized by LOM is presented in Figure 4-24a and b. The dendritic/cellular structure can be observed within the melt pools. The dendrites' growth direction is normal to the melt pool boundaries (solid-liquid front), which is opposite to the local heat flow direction at melt-pool boundaries. Moreover, the presence of solidification carbides on the intercellular retained austenite (RA) was evidenced (Figure 4-24c).

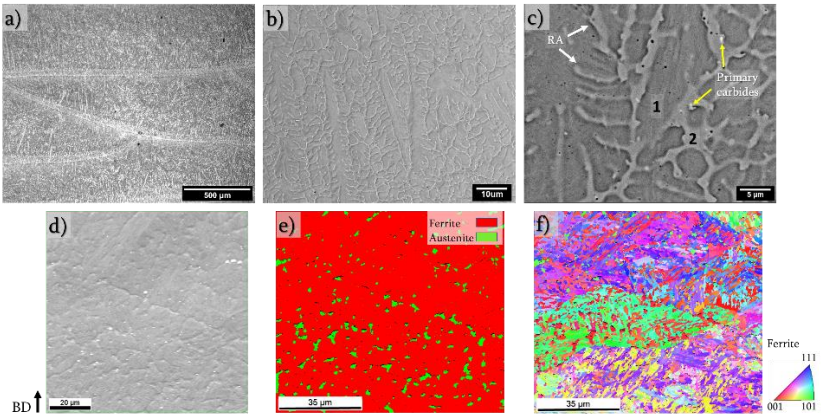


Figure 4-24 a) LOM of few melt-pools, b) cellular/dendritic structure, c) SEM micrographs of as-built sample presenting RA and solidification carbides, EBSD analysis results on AB sample, d) FSD microstructure image, e) phase map revealing retained austenite and f) IPF map of martensite

The chemical composition of the two spots on the matrix (1) and the intercellular region (2) are presented in Table 4-6. It can be observed that the intercellular region is enriched in Cr and Mo. The micro-segregation of alloying elements to the cell/dendrite boundaries occurs due to solute partitioning in liquid and limited solid-state diffusion during fast solidification that lowers the martensite start (Ms) temperature and stabilizes retained austenite (RA). The EBSD phase map (Figure 4-24e) clearly shows the distribution of the RA on the cellular boundaries. The IPF map (Figure 4-24f) highlights the fine martensitic microstructure.

Table 4-6 EDS Spot analysis results on spots marked in Figure 4-24c

| Composition in wt.% | Cr | Mn | Mo | Si | Fe |
|---|---|---|---|---|---|
| **1** | 6.9 | 1.0 | 2.0 | 0.4 | Bal. |
| **2** | 8.7 | 1.1 | 3.8 | 0.4 | Bal. |

The results of XRD analysis (Figure 4-25a) shows ~10 vol.% RA for the as-built material in line with metallographic investigations, while for the quenched sample (1000°C, 40 min) no RA was detected (i.e. below 2 vol.%). The quenched

microstructure excludes the solidification structure features due to the microstructural homogenization and elimination of micro-segregation by diffusion at the high temperature (Figure 4-25b).

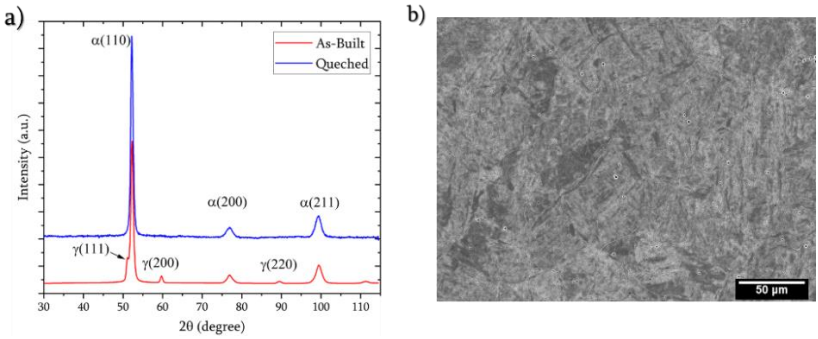


Figure 4-25 a) XRD diffraction pattern for the AB and quenched LDED Fe55, b) SEM micrograph of quenched microstructure (1000˚C,40min)

Preliminary calculations of the non-equilibrium solidification were carried out using the Scheil model (Figure 4-26a), considering complete diffusion in the liquid while no diffusion in solid material. Similar to the case of H13, since no traces of delta ferrite were evident in the AB microstructure, the primary solid phase was set to austenite (FCC) instead of delta ferrite. The simulation predicts the formation of Cr-rich $M_7C_3$, followed by the precipitation of Mo-rich $M_6C$.

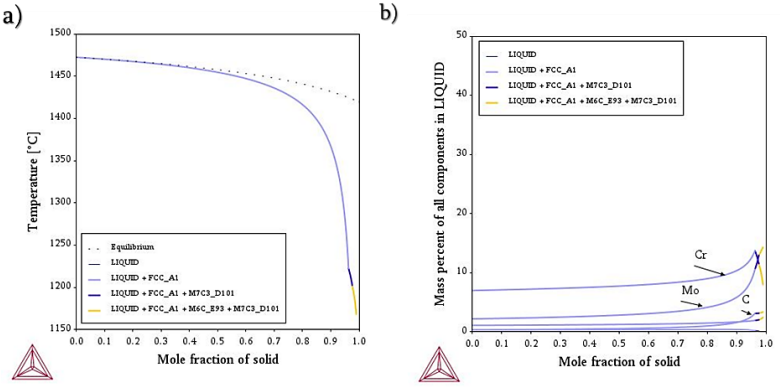


Figure 4-26 a) Mole fraction of solid vs. temperature and b) mass fraction of alloying elements in liquid vs. mole fraction of solid calculated using the Scheil model

The micro-segregation of alloying elements resulting from non-equilibrium solidification (Figure 4-26b) is in accordance with EDS analysis (Table 4-6) and can be considered as the cause of the chemical stabilization of RA at the cellular/dendritic boundaries due to lowering the martensite start (Ms) temperature.

### 4.2.2 Dilatometry studies on LDED Fe55

The dilatometry curves of quenching experiments showed that the onset of martensitic transformation (i.e., Ms temperature) after quenching from 1000°C for 20 min was around 230°C. The $A_{c1}$ and $A_{c3}$ temperatures were 790°C and 860°C, respectively (Figure 4-27a).

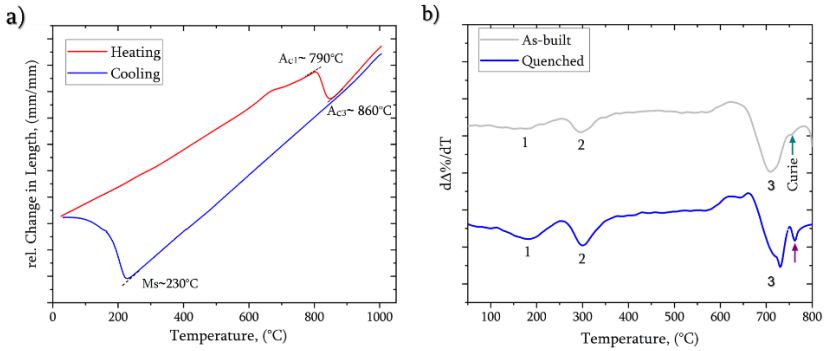


Figure 4-27 a) dilatometry records for austenitization and quenching at 1000°C, and b) isochronal tempering curves (Φ15°C/min)

Dilatometry curves for both quenched and AB specimens show an evident contraction (peak 1) between 100 and 250°C, corresponding to the precipitation of transition carbides. This is followed by another contraction (peak 2) between 250 and 300°C, associated with the transformation/precipitation of $M_3C$ carbides. The third and strongest contraction begins around 650°C, which is indicative of the formation of secondary alloy carbides from martensite (i.e., $M_{23}C_6$, $M_7C_3$, and $M_2C/M_6C$)[189]. The split in the third contraction peak is due to Curie temperature, which causes an expansion at ~770°C.

Comparing the curves for the AB specimen with the quenched one, one can realize that the first two peaks are evidently less intense. This again implies that these low-temperature precipitation events have already happened due to the IHT intrinsic to the layer-wise nature of the LDED. While the third peak relating to the precipitation of alloy carbides at higher temperatures is almost identical for the two

specimens since the previously solidified layers do not reach and remain at this high temperature upon deposition of successive layers.

### 4.2.3 Tempering behavior of LDED Fe55

Tempering curves for the direct tempering (DT) and quenching and tempering (QT) heat treatment schedules are depicted in Figure 4-28Figure 4-28 Tempering curves for the LDED Fe55 for the QT and DT schedules..

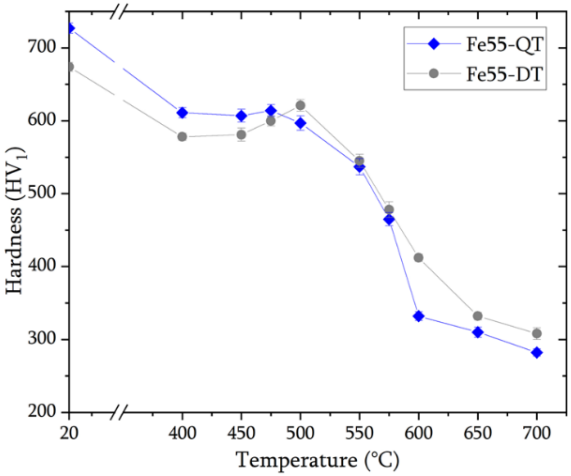


Figure 4-28 Tempering curves for the LDED Fe55 for the QT and DT schedules.

The as-built hardness was 670±12 HV1, while for the quenched sample, it was increased to 730±5 HV1, which can be attributed to the elimination of softer RA. The QT schedule shows a very slight secondary hardening effect at ~475°C due to the precipitation of Cr-rich $M_7C_3$ carbides and Mo-rich $M_2C$ carbides [189]. At higher temperatures, $Cr_{23}C_6$ nucleates at PAGBs and martensite lath boundaries; these carbides have higher coarsening rates and cause a continuous softening by increasing tempering temperature[190], [191]. In the directly tempered samples, a more pronounced secondary hardening peak was observed at 500°C. This can be mainly attributed to the decomposition of enriched RA and its transformation to fresh martensite and carbides during the first tempering cycle playing a role in an apparently enhanced temper resistance at higher temperatures in DT samples [83]. Similar to the QT scenario, the hardness drops continually upon increasing the tempering temperature as a result of the reduction in dislocation density and

coarsening of alloy carbides. The hardness in DT is kept slightly higher than the QT at temperatures higher than the secondary hardening peak. Firstly, this can be attributed to the decomposition of RA and the formation of fresh martensite in the AB specimens. Furthermore, the finer martensite substructure of AB samples, as compared with those undergoing austenitization and quenching, may contribute to a finer distribution of secondary carbides with a higher number density. This is more evident at very high tempering temperatures (over 600°C), where the softening is mainly governed by coarsening of the carbides (Ostwald ripening). This further emphasizes the requirement for V in such a composition in order to facilitate the precipitation of fine and stable secondary MC carbides for enhanced softening resistance.

### 4.2.4 Tempered microstructure of LDED Fe55

The tempered microstructure of DT-450 °C is characterized by the presence of primary carbides that are mainly located on the prior cellular boundaries (Figure 4-29a).

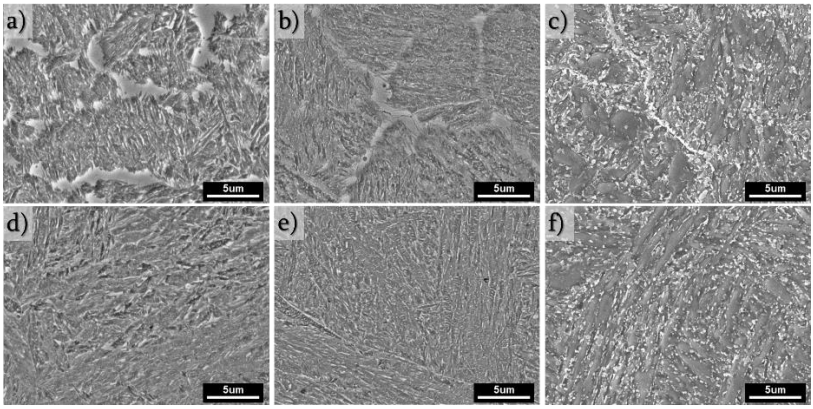


Figure 4-29 SEM micrographs of the LDED Fe55 a) DT-450 °C, b) DT-550 °C, c) DT-650 °C, d) QT-450 °C, e) QT-550 °C and f) QT-650 °C

By increasing the tempering temperature to 550°C, the RA on the cellular boundaries significantly decomposes into martensite. Traces of the primary carbides are still evident in the microstructure, and a small amount of fine secondary carbides within the martensitic matrix can be observed. By further increasing the tempering temperature to 650°C, cellular boundaries are replaced by an interconnected network of carbides, which is another indication for the decomposition of RA, and carbides precipitation within the martensitic matrix is also evident (Figure 4-29c).

Moreover, an evident coarsening of the carbides inside the martensitic matrix is observed, which is in line with the substantial drop in hardness. In the QT-450°C, the solidification structure is removed due to austenitization at high temperatures. Traces of primary carbides on prior cell boundaries are still evident (Figure 4-29d). The microstructure of the QT-550°C seems very similar to that of QT-450°C, no significant change in the size of primary carbides is observed, and precipitation of the secondary carbides within the martensitic matrix is more evident (Figure 4-29e). The microstructure of the quenched and tempered specimen at 650-°C clearly demonstrates coarsening of the secondary carbides within the martensite substructure. Compared to DT650°C, the distribution of carbides is more homogenous, and no accumulation and network of carbides are formed (Figure 4-29c &f).

### 4.2.5 Impact Toughness

The results for Charpy impact tests at room temperature on the DT samples are presented in Figure 4-30.

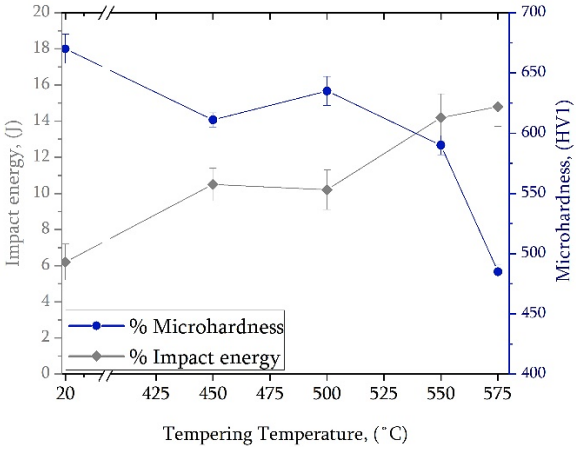


Figure 4-30 CVN impact energy and hardness vs. tempering temperature for DT samples

The impact toughness for the as-built sample was 5±1J at a hardness of 670±8 HV1. Tempering at 450˚C increased the impact toughness to 10.5±0.9 J. A slight decline was observed at 500 ˚C (peak hardening temperature), which is attributed to martensite formation (higher hardness). By increasing the tempering temperature beyond the secondary hardening peak, the impact toughness increases due to softening of the material. At 575˚C, this value reaches 15.3± J at a hardness level of ~500 HV1. These values are comparable and even superior to the recommended

values for H13 according to NADCA (North American Die Casting Association) under NADCA#207-2003 (i.e. 10-13.5 J.cm$^{-2}$ at 44-46 HRC)[192]. Even though the tempering temperature to achieve 500 HV for Fe55 is considerably lower than that of H13 (i.e., 575˚C vs. 625℃, respectively). However, the greater toughness attained at this degree of hardness enables the use of this alloy in applications that do not require significant thermal softening resistance or which operate at slightly lower temperatures, such as polymer injection molding dies and trimming dies.

Specimens tempered at 575˚C demonstrated the highest impact toughness. Moreover, according to the tempering curves (Figure 4-28 Tempering curves for the LDED Fe55 for the QT and DT schedules.), a similar hardness is obtainable by tempering at this temperature for both scenarios. Therefore, to compare the material's response to the two different heat treatment strategies, two groups of samples were tempered at 575˚C in QT and DT conditions, and the results are depicted in Table 4-7. The results showed that QT samples possessed slightly higher impact toughness at fairly similar hardness values. Although it is noteworthy that despite possessing inferior impact toughness compared to QT specimens, the toughness of DT-575 ˚C Fe55 is comparable to or even better than LAM H13 with similar hardness values[193], [194].

Table 4-7 Hardness and CVN impact energy for DT and QT specimens tempered at 575˚C

| Sample | Hardness (HV1) | CVN Impact Energy (J) |
|---|---|---|
| **QT-575˚C** | 469 ± 5 | 16.2 ± 0.9 |
| **DT-575˚C** | 478 ± 7 | 14.8 ± 1.9 |

Figure 4-31 presents the SEM micrograph of the fracture surfaces for the impact toughness specimens.

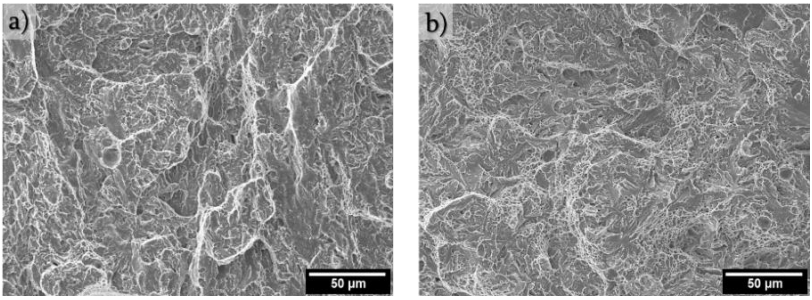


Figure 4-31 SEM micrographs for fracture surfaces of a) DT-575˚C and b) QT-575˚C

The predominant fracture mode exhibited by the samples is transgranular quasi-cleavage in nature, which is typical for martensitic steels tempered at high temperatures [182]. The presence of dimples and microvoids also evidenced plastically deformed regions. The fracture surface of the DT specimen clearly demonstrates more extensive cleavage surfaces, which can be attributed to the formation of carbide networks at cellular boundaries upon tempering (see Figure 4-29) and can explain the lower impact toughness of these samples compared to the QT scenario.

### 4.2.6 Fracture toughness

Further investigations on the effect of microstructure and heat treatment strategies on the anisotropy of mechanical properties were performed by comparing the apparent fracture toughness of material in samples that contained a notch parallel to the build direction (V) and samples that had a notch perpendicular to the BD(H), as demonstrated in Figure 4-32a. All the specimens were tempered at 550˚C and had a hardness of ~530 HV. As depicted by Figure 4-32b, specimens with the notch parallel to the BD (V) showed higher apparent fracture toughness than those with the perpendicular notch. This can be attributed to the fact that in the DT-V and QT-V, the crack propagation path is perpendicular to the meltpool boundaries, which might deviate from the crack path and reduce its energy. This can be supported by the fact that the difference in DT-V and DT-H (110.2±1.3 vs. 100.1±3 MPa.m$^{1/2}$, respectively) is more significant than for QT-V and QT-H (106.3±3.5 vs. 103.0 ±2.7 MPa.m$^{1/2}$, respectively).

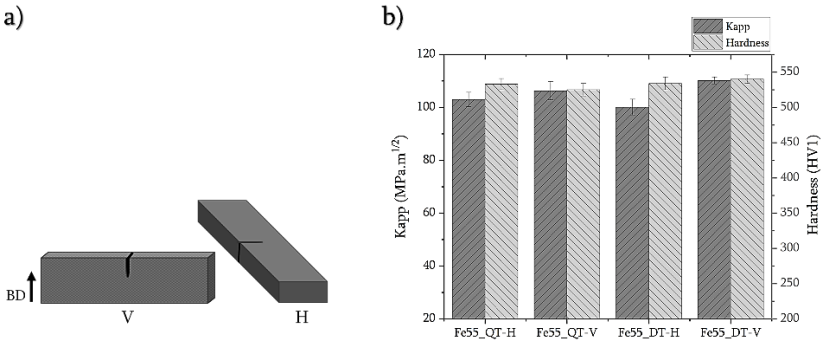


Figure 4-32 a)Schematic of specimens for FT test in two directions, and b) Kapp and hardness for the QT and DT samples for the two directions.

The fracture surfaces of DT specimens evidently show cleavage surfaces oriented along the columnar grains aligned with the BD (Figure 4-33a& c), while this is not evident in the QT samples due to more homogenized microstructure and elimination of the solidification structures during austenitization (Figure 4-33b& d).

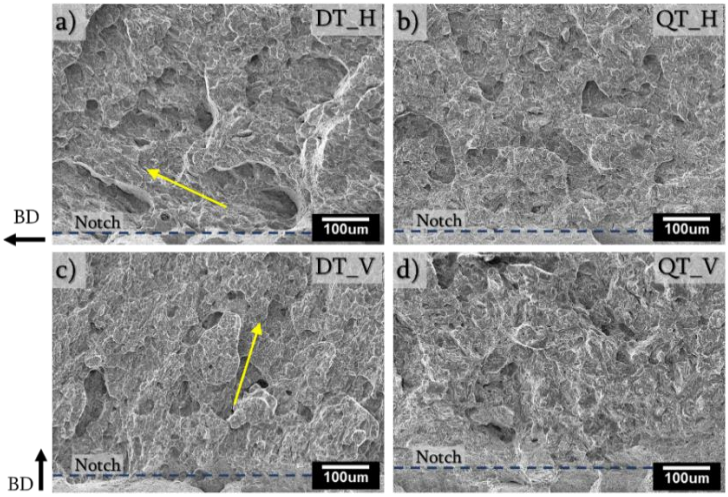


Figure 4-33 SEM micrographs of the fracture surfaces for FT specimens, a)FE55_DT-H, b) FE55_QT-H, c) FE55_DT-V, d) FE55_QT-V

In QT samples, the fracture surface indicates quasi-cleavage behavior, along with high distribution of dimples on the fracture surface, while in DT samples, the fracture surface is governed by more by transgranular quasi-cleavage facets with just very limited and localized dimples and microvoids (Figure 4-34).

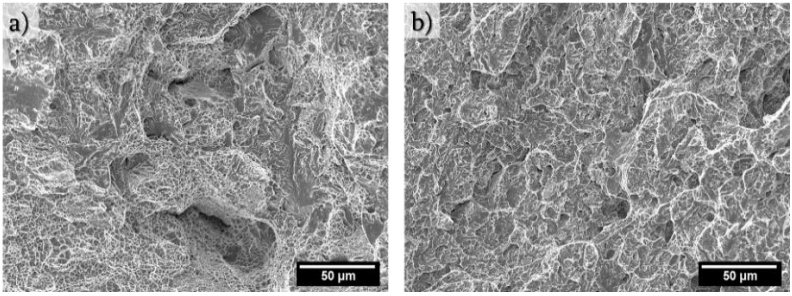


Figure 4-34 Higher magnification of fracture surfaces for a) QT-V and b)DT-V

The difference between apparent fracture toughness for the QT and DT samples for each direction is almost negligible. This might be explained in view of the counteracting of the two effects. Although it is expected that DT specimens demonstrate inferior $K_{app}$ due to the non-homogeneous microstructure and formation of carbides on cellular boundaries, on the other hand, it has been demonstrated that fracture toughness has an inverse relationship with the grain size ($K_{IC} \sim d^{-1}$ ) [195]. Therefore, the finer microstructure of the DT specimens might counteract the effect of carbide precipitation on the cellular boundaries, and hence, the $K_{app}$ in the QT and DT specimens are almost similar.

### 4.2.7 Tempering resistance

The tempering behavior of the DT and QT samples soaked at 600°C are presented in Figure 4-35a. A pair of specimens (i.e., (DT500 HV, QT500 HV), and (DT420 HV, QT420 HV)), were tempered in a way to obtain the same starting hardness. Samples are tempered well above the secondary hardening temperature (i.e., ≥500°C).

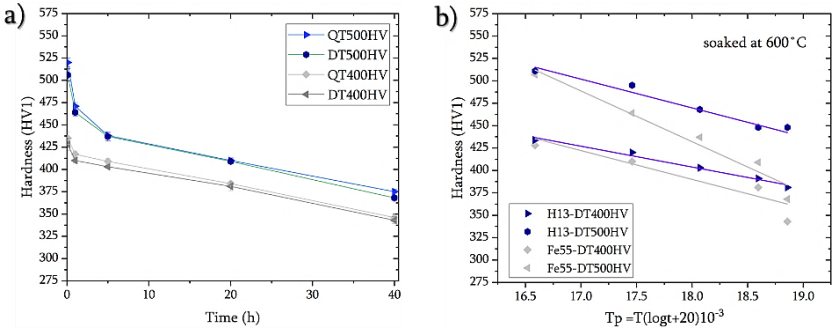


Figure 4-35 a) tempering resistance for Fe55 as hardness vs. time, b) comparison of the tempering resistance for Fe55 and H13

A substantial drop in hardness to 440 HV after 5h is observed for both DT500 HV and QT500HV samples. This is attributed to a drop in dislocation density of the lath martensite in the initial stages of the test [183], [196]. This decline is less pronounced for the samples with an initial hardness of ~430. This is mainly due to the fact that these samples have already been tempered at higher temperatures compared to 500HV specimens (580°C vs. 550°C, respectively), and therefore the decline in dislocation density has already occurred for this sample at higher tempering temperature. The rate of hardness drop after 5h up to 40h is almost identical for both pairs of DT and QT samples for both hardness values. It can imply that, in this

case, the governing softening mechanism in prolonged soaking times is mostly related to the coarsening/transformation of the fine secondary carbides. Another reason is that unlike for H13 since both DT and QT had been tempered at similar temperatures, and therefore their response to soaking at similar temperatures is identical.

For a better comparison of the tempering resistance of H13 and Fe55, their tempering hardness for the DT500 HV and DT420 HV versus Tp are plotted in Figure 4-35b. Looking at the slope of the fitted lines, it is evident that H13 samples systematically show a significantly higher tempering resistance compared to Fe55. The first reason for this behavior can be related to the different secondary carbides in these two alloys, where the main carbides in Fe55 are Cr-rich $M_{23}C_6$, while in H13, we have a high amount of V-rich MC carbides. Therefore, due to the substantially higher coarsening rate of $M_{23}C_6$[189], the hardness decline in Fe55 is more pronounced. Another justification can be given in view of the initial tempering temperature of the samples. In order to achieve harnesses of 500 HV1 and 430 HV1, Fe55 samples were tempered at 550°C and 590°C, respectively. In comparison, these values for the H13 specimens were 625°C and 650°C, correspondingly. Therefore, in view of the higher initial tempering temperature of the H13 samples, and considering that this difference is more for the 500 HV (where the difference in the original tempering temperature is higher), it seems that the initial tempering temperature has a substantial contribution in tempering behavior of the materials.

### 4.2.8 Conclusions

The tempering behavior of a recently utilized tool steel was investigated by applying two different heat treatment strategies,

- The L-DED Fe55 shows a cellular/dendritic structure and as-built microstructure comprised of martensite with ~10 vol.% of retained austenite at interdendritic regions. The presence of some primary carbides in RA regions was also evidenced.
- The as-built microhardness was 670±12 HV1, while for the quenched samples (1000°C, 40min), this value increased to 730±5 HV1. This could be attributed to the elimination and decomposition of the soft RA phase and its replacement with quenched martensite.

- At similar hardness levels, the impact toughness of DT specimens was slightly less than QT, but it was still more than the values reported for LAM H13 at similar hardness levels.
- The apparent fracture toughness of LDED Fe55 at a hardness of ~550 HV1 was between 100-110 MPa.m$^{1/2}$, depending on the heat treatment strategy or the sample orientation. The anisotropy was less pronounced in the QT specimens.
- Direct tempering seems to be a suitable practice for LDED Fe55 since the tempering behavior is very similar to QT samples. No significant difference was evidenced between the tempering resistance of the DT and QT samples.
- Compared to H13 samples tempered to a similar hardness, the tempering resistance of the Fe55 is inferior to that of H13. This was attributed to the different carbide systems in the two alloys and the difference in initial tempering temperature.

# Part 2 Carbon-free Maraging Tool Steels

## 4.3 Maraging steels

### 4.3.1 Microstructure and hardness of LDED Osprey® MAR-60HRC

The microstructure of the deposited as-built samples comprises fine cellular/dendritic features (Figure 4-36a).

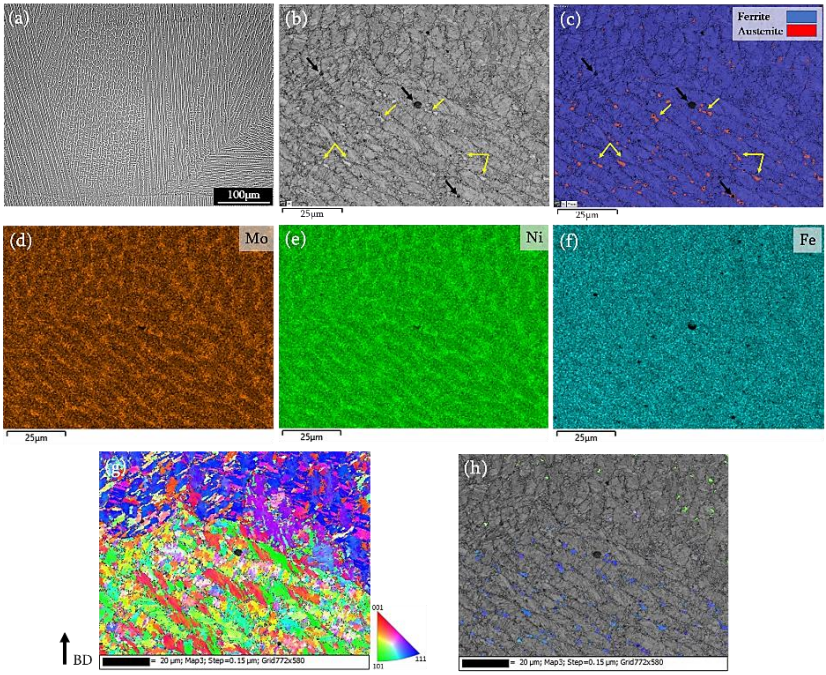


Figure 4-36. a) LOM micrograph showing the overall microstructure of the LDED Osprey® MAR-60HRC (Vilella's reagent), b) EBSD band contrast image, c) Corresponding phase map overlaid by band contrast image, and corresponding EDS elemental map for d) Mo, e) Ni, f) Fe, IPF maps of g) martensite, and h) RA

EBSD band contrast and phase maps revealed the presence of retained austenite (RA) located in the intercellular regions (yellow arrows in Figure 4-36b and c). Corresponding EDS maps evidenced a higher concentration of Mo and Ni and a lower Fe content in the intercellular areas (Figure 4-36d-f). Thermal undercooling provides the driving force for dendrite/cell nucleation and growth. The microsegregation of alloying elements to the cell/dendrite boundaries occurs due to solute partitioning in liquid and limited solid-state diffusion during fast solidification, characteristic of laser-based AM processes such as LDED [44]. The micro-segregation of alloying elements at cell boundaries leads to the chemical stabilization of RA in those areas [1]. Inverse pole figure (IPF) maps of martensite (formed inside the prior austenite grains) and retained austenite along the build direction are presented in Figure 4-36g and h. It can be clearly noted that the crystal orientation of the RA is related to the prior austenite grain orientation. The RA in

the bottom grain is oriented closer to <111> while in the top grain is along <110> direction.

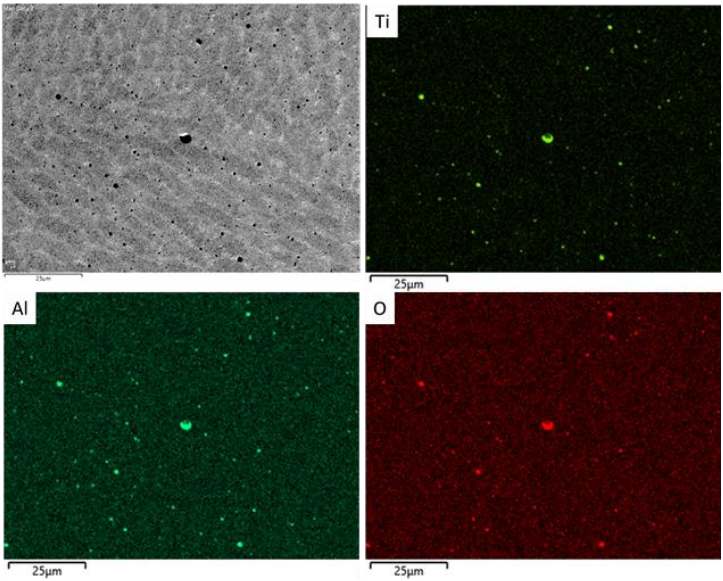


Figure 4-37 EDS elemental mapping of oxide particles in the as-built sample

Figure 4-37 represents the EDS elemental mapping on the fine and mostly round particles presented by black arrows in Figure 4-36 b& c. Their size varies from a hundred nm to a few microns, are rich in Ti (26 at. %), Al (11 at. %), and O (61 at. %), and are plausibly Ti- Al-rich oxides close to $(Ti, Al)_2O_3$ stoichiometry. Due to the high affinity of Ti and Al for O, the oxides can precipitate from the liquid during the LDED processing. Because of the fast cooling rates, and the constraint by primary austenite crystals, these oxides remain fine in size [45].

### 4.3.2 Heat treatment of maraging steels

#### 4.3.2.1 Dilatometric studies

To study the response of the LDED Osprey® MAR-60HRC to heat treatment, firstly, dilatometry experiments were performed on the AB specimens. It is noteworthy that to minimize the probable effect of thermal cycles on the thermal history and microstructure of specimens. Dilatometry samples were cut from the topmost part of the deposition. Figure 4-38a depicts the isochronal aging behavior for the as-built Osprey® MAR-60HRC and Osprey® 18Ni300. The first derivative of the relative

change in length against temperature (dΔ%/dT) plotted vs. temperature shows three distinct contraction peaks.

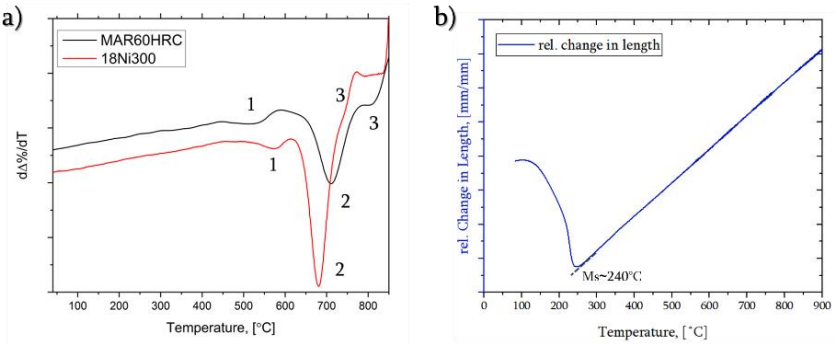


Figure 4-38 a) Isochronal heating dilatometric records of LDED Osprey® MAR-60HRC and Osprey® 18Ni300 (heating rate, 20°C/min), b) dilatometric records during cooling from 900°C for Osprey® MAR-60HRC

According to previous studies, the first peak (peak 1) with an onset around 440°C is representative of $Ni_3Mo$ and $Ni_3Ti$ precipitation [92], [114], [197]. The large contraction (peak 2) with an onset of around 600°C is related to austenite reversion. The 3rd contraction peak (peak 3) occurs as a result of the shear transformation of the remaining martensite ($\alpha'$) to austenite ($\gamma$) [198]–[200]. In this system, similar to the 18Ni series, austenite is an equilibrium phase even at temperatures lower than that of complete $\alpha \rightarrow \gamma$ transformation temperature (~730°C). Therefore, during isochronal annealing, the system approaches equilibrium leading to austenite nucleation from the meta-stable Fe-Ni martensite through a diffusion-controlled reaction (i.e., austenite reversion). The Osprey® 18Ni300 curve follows a similar pattern to that of Osprey® MAR-60HRC, but the intermetallic precipitation onset temperature is slightly higher at roughly 500°C, suggesting that this grade may require longer / higher temperatures for aging. In addition, the peak associated with austenite reversion is significantly more intense, which can result in decreased hardness and improved toughness for this grade. Figure 4-38b shows the dilatometric records upon cooling LDED Osprey® MAR-60HRC from 900°C. The $M_s$ temperature is ~240°C. This temperature is important and will be used in the calculations for the intrinsic aging optimization process in section 4.3.5.

#### 4.3.2.2 Aging behavior of as-built maraging steels

The aging curves (Figure 4-39a) of as-built Osprey® MAR-60HRC with 370 HV1 starting hardness show that the steel can be age-hardened in ~10 min to around 575 HV1 by aging at 480°C.

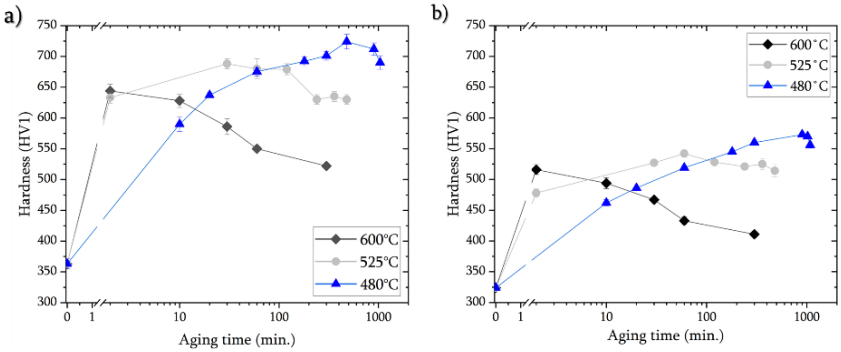


Figure 4-39. Aging curves of a) Osprey® MAR-60HRC and b) Osprey® 18Ni300 maraging steel.

Holding for longer times (~480 min) leads to a maximum hardness of ~730 HV1. After the peak hardness is achieved (~480 min), a slight drop in hardness by longer holding is evident. By aging at 525°C, the hardness increases to 625 HV1 in merely 2 min. Continuation of aging for 30 min results in maximum achievable hardness (680 HV1) at this aging temperature. Longer times cause softening due to over-aging. At 600°C, the maximum hardness is obtained by 2 min holding (i.e., 650 HV1), and a longer holding time leads to overaging. For comparison, the aging curves of Osprey® 18Ni300 are reported (Figure 4-39b). The as-built hardness is around 330 HV1, slightly lower than that of Osprey® MAR-60HRC. The aging response is very similar to the MAR-60HRC, while the achievable hardness is almost 180 HV1 lower than that of the Osprey® MAR-60HRC undergoing identical heat treatment schedules.

The yield strength ($\sigma_y$) and hardness of maraging steel in the as-built condition can be modeled by Eq. 4-4 [201]

$$\sigma_Y \cong 3HV \cong \sigma_0 + \sigma_{martensite} + \sigma_{ss} \qquad \text{(Eq. 4-4)}$$

where $\sigma_0$ is the lattice friction stress, $\sigma_{martensite}$ is the contribution of martensite sub-structure (e.g., block and lath size and dislocation density), while $\sigma_{ss}$ represents the contribution of solid solution hardening (Eq. 4-5).

$$\sigma_{ss} = \sum_i \sqrt{B_i^2 x_{i,\alpha'}} \quad \text{(Eq. 4-5)}$$

The critical resolved–shear stress due to the presence of substitutional solute atoms, $\sigma_{ss}$, is a function of the atomic fraction of each substitutional element ($x_{i,\alpha'}$) and its strengthening constant ($B_i$) given the lattice and modulus misfit compared with Fe. It is assumed that softer intercellular RA does not negatively influence the overall strength of the as-built material.

In aged conditions, intermetallic particle strengthening emerges due to the Orowan looping mechanism, which can be modeled by Eq. 4-6[123]. This term can be added linearly to Eq. 4-4:

$$\Delta\sigma_{Orowan} = M \frac{0.4Gb}{\pi\sqrt{1-\nu}} \frac{1}{L} \ln\left(\frac{2r_s}{b}\right) \quad \text{(Eq. 4-6)}$$

where $M = 2.9$ is the Taylor factor for BCC metals in tension, $\nu \sim 0.3$ is the Poisson's ratio of the matrix, $L$ is the mean inter-precipitate distance, $r_s = (2/3)^{1/2} r$ is the mean radius in the glide plane ($r$ denotes the radius of the precipitates), and $b$ is the Burgers vector. It should be noted that after aging, the solid solution hardening effect of the elements contributing to the formation of the precipitates (i.e., Ni, Ti, and Mo) decreases by increasing the volume fraction of the precipitates.

Given the above description, especially the Orowan strengthening mechanism, up to the peak aging condition, strength increases by an increase in the number density of nano-sized precipitates, which is correlated to the vol% and size of precipitates. Over-aging leads to a drop in hardness and strength because of precipitate coarsening (i.e., lowered number density) and the formation of reverted austenite. Higher temperature aging and longer times contribute to enhanced coarsening and a larger volume fraction of reverted austenite due to the enhanced diffusivity.

This is clearly reported that the increase in Ni content from 11 wt.% to 23 wt.% does not dramatically change the dislocation density and strength of Fe-Ni lath martensite [202]. Therefore, from the strength point of view, the key difference between Osprey® MAR-60HRC and Osprey® 18Ni300 chemistry is their Co, Mo, and Ti content. Given the high supersaturation of alloying elements within the Fe-Ni martensite in AM-processed maraging steels, the higher as-built hardness of Osprey® MAR-60HRC should be discussed in view of a larger substitutional solution hardening effect. According to Fleischer [203], the strengthening results from elastic interactions of solute atoms with screw dislocations, governed by the difference in effective modulus and size of the substituted atom. Ti and Mo show the highest solid solution strengthening effect [201], while Co (having a nearly similar atomic size to iron) has the lowest contribution. The substantial increase in

Mo causes more extensive solid solution strengthening in Osprey® MAR-60HRC, leading to increased as-built hardness. Consequently, in aged condition, higher Mo wt.%, and its combination with high Co gives rise to a higher vol.% of $Ni_3Mo$ and possibly μ-phase precipitates, thus resulting in higher maximum post-age hardness (61HRC) compared with Osprey® 18Ni300 (55HRC) [127].

### 4.3.3 Austenite reversion

Figure 4-40 presents the microstructure of samples after aging for 5 hours at 480 and 525˚C, respectively. The inset in Figure 4-40a shows the uniform distribution of nano-sized intermetallic particles within the martensitic matrix, which are responsible for the increase in hardness and strength.

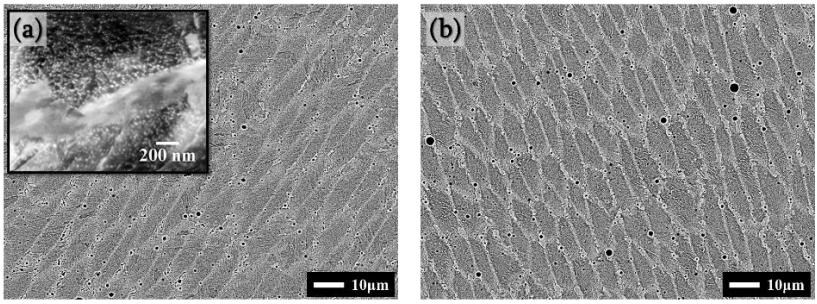


Figure 4-40 SEM micrographs LDED Osprey® MAR-60HRC aged for 5 hours at a) 480 ˚C (the inset highlights nano-sized precipitates within the martensitic matrix) and b) 525˚C; note the increased thickness of the intercellular austenite appears brighter in BED-SEM micrograph

It can be clearly observed that the thickness of the cell boundaries, which appear brighter in electron backscatter mode (BED) micrographs, is increased in the sample aged at a higher temperature. This is an indication of increased reverted austenite content upon aging at higher temperatures. In agreement with previous works [6,49], RA at the cell boundaries can serve as a preferential site for the austenite reversion during aging. This is because, from an energetic and crystallographic point of view, it is favorable for reverted austenite to form Ni-enriched shells around existing retained austenite. In general, since austenite is an equilibrium phase in the aging temperature interval for most of the Fe-Ni maraging alloys, austenite reversion by diffusion during aging is expected. Austenite reversion is accelerated by increasing the aging temperature due to the enhanced diffusivity, leading to the local enrichment of Ni within the martensitic matrix upon dissolution of Ni-rich intermetallic precipitates and formation of Fe-Mo rich precipitates [50].

The decline in maximum achievable hardness upon increasing the aging temperature (Figure 4-39) can be attributed to the larger amount of austenite and enhanced austenite reversion kinetics at higher temperatures that are well in line with the microstructural analysis (Figure 4-40) and equilibrium property diagram of Osprey® MAR-60HRC (Figure 4-41a).

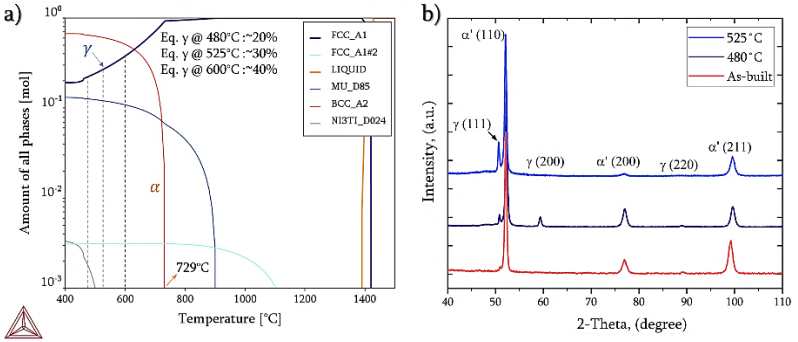


Figure 4-41 a) equilibrium property diagram for Osprey® MAR-60HRC and b) XRD results on heat treated specimens

As demonstrated by the STEP diagram, at the equilibrium state, the amount of reverted austenite can increase from about 20% at 480°C to as high as 40% at 600°C. The XRD results (Figure 4-41a b) for the as-built samples and those aged at 480˚C and 525˚C show ~5, 8, and 20 vol.% austenite, respectively. The discrepancy between amounts of retained austenite predicted by the STEP diagram and XRD results is due to the short aging time in XRD specimens. The austenite reversion kinetics at lower aging temperature for a holding time of 5h was not significant, and the austenite content did not change drastically compared with the as-built material. Aging at higher temperatures gave rise to the reversion of a significant amount of austenite. The peaks pertaining to austenite in XRD measurements, especially for the sample aged at 480°C (see (200) peak intensity) and 525°C (see (111) peak intensity), indicate the existence of a texture. The texture in RA in laser-processed steels is a result of the epitaxial growth of parent austenite at high temperatures along the build direction during the deposition (see Figure 4-36a). The reverted austenite preferentially grows on the existing RA, preserving the same texture [51]. The absence of the (200) peak for the 525°C sample is also attributable to the previously noted preferential orientation of austenite in this sample.

### 4.3.4 Effect of Heat Treatment on Compressive Strength

Figure 4-42 presents the compressive stress-strain curves for the LDED Osprey® MAR-60HRC in the AB state as well as different heat treatment conditions. As it can be observed and mentioned in section 3.4.7, in order to prevent damage to deformation rods and for the machine's safety, deformation was limited to 5% true strain for the aged specimens.

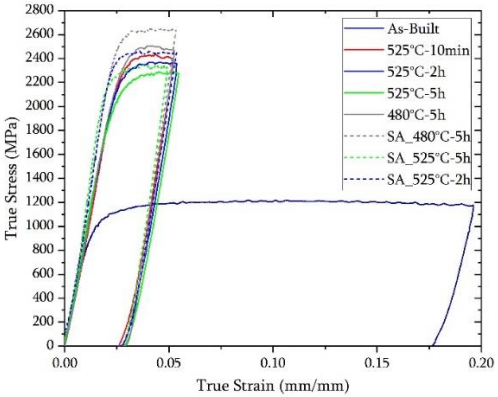


Figure 4-42 Compressive stress-strain curves for Osprey® MAR-60HRC for different aging conditions.

The results of compressive strength and hardness values are presented in Table 4-8.

Table 4-8 Summary of compressive yield strength and hardness values for the heat treated LDED Osprey® MAR-60HRC

| Specimen | Yield strength (MPa) | Compressive strength (MPa) | Hardness (HV1) |
|---|---|---|---|
| As-Built | 991±17 | 1205±21 | 368±9 |
| 525°C-10min | 2100±12 | 2303±12 | 670±6 |
| 525°C-2h | 2120±18 | 2360±11 | 678±10 |
| 525°C-5h | 2002±12 | 2270±18 | 630±12 |
| 480°C-5h | 2250±15 | 2475±14 | 710±8 |
| SA_525°C-2h | 2190±11 | 2435±11 | 680±6 |
| SA_525°C-5h | 2115±14 | 2338±10 | 645±6 |
| SA_480°C-5h | 2470±10 | 2632±10 | 730±5 |

The as-built hardness for the LDED Osprey® MAR-60HRC was 363±8 HV1, and the relative yield strength and compressive strength were 991±17MPa and 1205±21 MPa, respectively. The sample aged at 480 ˚C for 5 hours showed the highest hardness and yield strength with a hardness of 710±8 HV1, yield strength equal to 2340±16MPa, and compressive strength of 2475±11 MPa, which was well expected from the aging curves for this temperature as it is close to peak hardness of the material at this temperature. Direct aging at 525 ˚C for only 10 min resulted in a considerable increase in hardness (670±6 HV1) and yield strength (i.e., 2100±12 MPa). Aging for 2 h at this temperature led to a slight increase in hardness and yield strength to 678±10 HV1 and 2105±14 MPa, respectively. Longer aging time at 525˚C (5 h) resulted in overaging of the samples, leading to reduced hardness, yield strength, and compressive strength (i.e., 630±12 HV1, 1990±13 MPa, and 2270±18MPa, respectively).

The second set of experiments was performed on samples that went through solution annealing treatment (SA) before aging. The hardness value for the SA samples declined to ~340 HV1 as a result of the dislocation recovery and possibly grain growth. In contrast, it was observed that for all the cases, the hardness and yield strengths were superior to those of directly aged samples at the same aging temperature and time. This can be due to the homogenization and elimination of micro-segregated regions in the as-built microstructure, which were characterized as RA with a high concentration of Mo and Ni. This leads to less vol.% of RA, which does not contribute to aging in the SA material. Therefore, a larger vol.% of martensite contributes to the age-hardening process. It should be mentioned that even though austenite lowers the strength of the material, it may be desirable in some applications, as it allows promotes ductility and toughness[15].

### 4.3.5 Intrinsic heat treatment during LDED

In order to investigate the feasibility of intrinsic heat treatment during the deposition of maraging steels, Osprey ® MAR-60HRC was selected as an industrially available powder in the market. The motivation behind this selection was the large wt.% of Co and Mo and lower wt.% of Ni compared with Osprey® 18Ni300. The combination of high amounts of Mo and Co increases the peak hardness of this steel up to 61HRC vs. 55HRC in Osprey® 18Ni300 and strongly enhances the aging kinetics even at lower temperatures (see Figure 4-39). Fast precipitation kinetics is crucial to allow age-hardening during the fast heating cycles, characteristic of the LDED process. Lower Ni content leads to delayed austenite reversion during heating, thus providing a wider aging temperature interval. Moreover, reduced Ni leads to higher Ms temperature [14]. This increases the chance for each layer to

undergo a martensitic transformation during cooling if a correct deposition strategy is chosen. Therefore, this alloy can be a suitable candidate for exploiting IHT during the LDED process. Specifically, in hybrid manufacturing, very localized heat treatments (e.g., IHT) on the additively manufactured segment without affecting the base material heat treatment thermal history might add value to the whole AM process.

Therefore, given the fast aging response in this system, intrinsic aging scenarios were designed to exploit the age-hardening effect during the deposition process. Three samples comprising 15 layers were built with three different pause intervals between each layer. Interlayer dwell times of 30 s, 120 s, and 250 s (after this, IDT-30s, IDT-120s, and IDT-250s, respectively) were selected. According to the hypothesis, an optimum pause time should satisfy the following conditions;

1. Each layer (e.g., layer x) undergoing a temperature increase within the austenite stability range (i.e., >~720°C) by the deposition of successive layers (x + y, y ≥1 ) should have enough time to cool down below $M_s$ (~250°C) to trigger martensitic transformation. Ideally, the temperature should drop below martensite finish ($M_f$) temperature (~120°C) to avoid any retained austenite.

2. In a later stage of deposition, each layer (x) undergoing subcritical heating below the austenite temperature stability range should reach the aging temperature interval (~450°C-650°C) to trigger the precipitation of intermetallic particles within martensite, and ideally, no overaging should occur.

Simulated thermal history on points selected in the middle of 1$^{st}$ and 12$^{th}$ deposited layers during the deposition of 15 successive layers for selected inter-layer pause times are shown in Figure 4-43a-c.

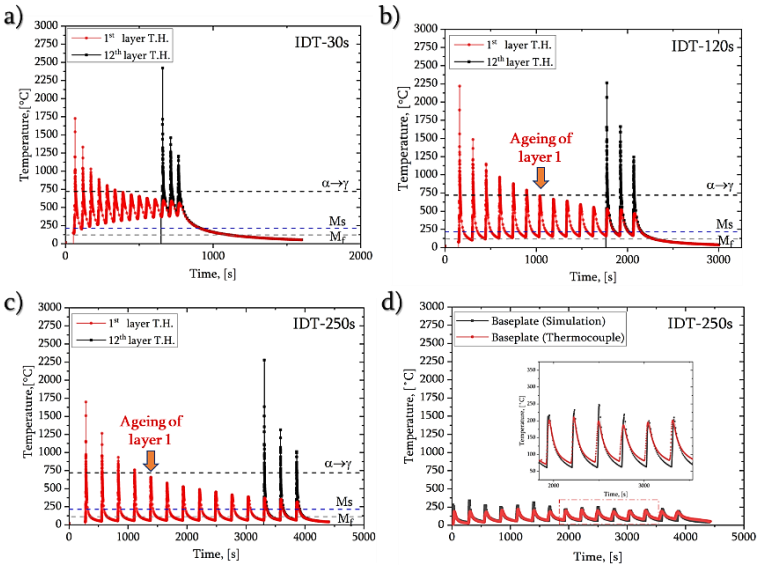


Figure 4-43 Simulations of thermal histories for individual deposited layers during the deposition process for the 1st and 12th layers in a) IDT-30s, b) IDT-120s, c) IDT-250s specimens, and d) thermal history simulation of the base plate together with experimental results measured with thermocouple for the IDT-250s.

It can be appreciated that for the IDT-30s scenario (Figure 4-43a), the time for cooling is not sufficient to cool down the 1st deposited layer below $M_s$ ( i.e., 215°C) during the whole deposition process. This literally means that this layer never experiences martensitic transformation during the deposition period. Similar behavior is shown for layer 12th. Therefore condition 1 is clearly not fulfilled. In the IDT-120s scenario (Figure 4-43b), the minimum attainable temperature in the first layer is around 100°C which is below $M_f$ temperature. Therefore, the material undergoes a full martensite transformation upon cooling. The first layer experiences thermal cycles above α→γ transformation temperature up to the deposition of the 6th layer (i.e., y=5), and condition 1 is fulfilled. After cooling down below $M_f$ temperature during the 120s pause time, the temperature in layer 1 increases to around 650°C as a result of the deposition of the 7th layer (i.e., x+y+1). At this temperature, precipitation of intermetallic particles from the martensite is plausible. From this point onwards, layer 1 is subjected to aging, and condition 2 is also fulfilled. Considering the thermal history of layer 12, it is clear that even if this layer undergoes a martensitic transformation, its highest achievable temperature during the deposition of the last three layers is always higher than the α→γ transformation,

preventing any aging phenomena (i.e., condition 2 cannot be met). Therefore it is expected that the top layers do not undergo aging.

It is evident that by implementing the IDT-250s scenario (Figure 4-43c), 1st deposited layer is heated up above α→γ transformation temperature during deposition of the next layer and cooled down well below $M_f$ (i.e., ~50°C) during each pause. Condition 1 is fulfilled up to the deposition of the 5th layer (i.e., x=1 & y=4). Deposition of the 6th layer (i.e., layer x+y+1) brings layer 1 into the aging temperature interval. This continues until the end of the deposition. Like in the previous case, the last four layers cannot meet condition 2 (see the thermal history for the 12th layer). A thermocouple was attached to the base plate, and the resulting temperature changes were recorded for each of the three deposition scenarios to ensure the accuracy of the simulations. A comparison of the thermocouple experimental findings with the simulated results for IDT-250s reveals a good agreement between the two sets of data (Figure 4-43d).

Optical micrographs of chemically etched deposited samples along the building direction show that IDT-30s sample response to etching is quite uniform (Figure 4-44a), while in IDT-120s and IDT-250s, the bottom and middle regions are heavily etched. The response in the IDT-250s sample is stronger than that of IDT-120s. The topmost layers were less responsive to etching (Figure 4-44b&c). This conveys that some precipitation should have occurred in the heavily etched regions, making the material more prone to chemical attack by the etchant.

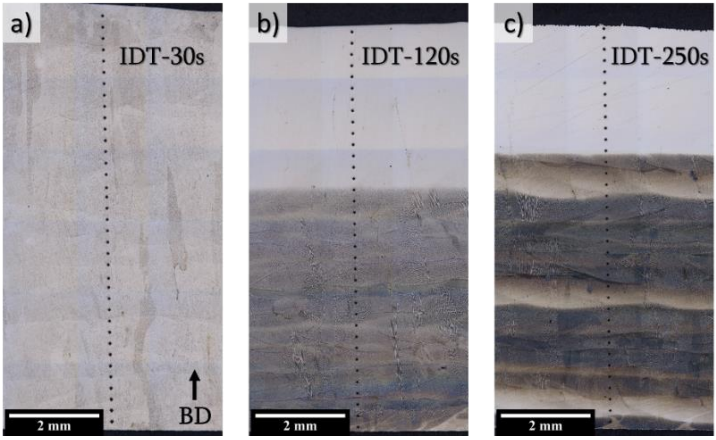


Figure 4-44 Optical micrographs along build height of a) IDT-30s sample showing uniform response to etching, b) IDT-120s sample with bottom to middle layers more responsive to etching, c) IDT-250s sample

SEM micrographs of the IDT-30s sample did not reveal any precipitation within the matrix (Figure 4-45a). At the same time, massive nano-precipitation of intermetallic particles, probably of two types (i.e., coarser spherical particles marked by yellow arrows and finer elongated ones marked by red arrows in the inset), was evident within the martensitic matrix in IDT-250s part (Figure 4-45b), in agreement with its response to chemical etching.

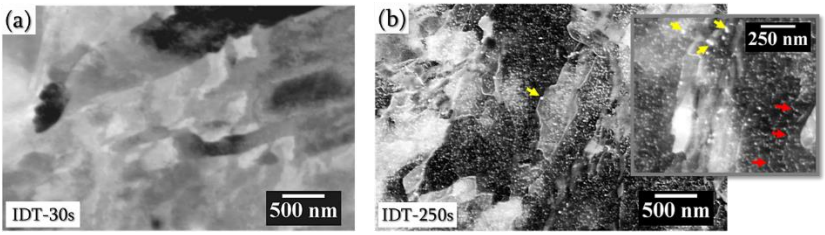


Figure 4-45 SEM micrograph of IDT-30s sample showing martensitic microstructure with no precipitation, and b) SEM micrograph of IDT-250s sample showing massive nano-precipitation

The first derivative of dilatometric curves (dΔ%/dT) for the AB specimen, Specimens with the three different IDTs, and a sample aged to peak hardening condition are presented in Figure 4-46a. As discussed in section 4.3.2.1, the first peak corresponds to the precipitation of intermetallics, while the big contractions of peaks 2 and 3 correspond to austenite reversion. It can be observed that for the IDT-30s specimen, the intensity of the peaks is almost identical to the AB specimen, implying that almost no precipitation has occurred in this specimen. The intensity of peak 1 for the IDT-120s specimen was less, and the peak is slightly shifted to higher temperatures, suggesting that some of the precipitation at lower temperatures have already taken place in this specimen. This trend is intensified for the IDT-250s sample, and the first peak is very shallow and shifted to a higher temperature, meaning that the precipitation is almost completed for this specimen. Finally, the curve for the peak-hardened specimen shows no more contraction relating to precipitation since all the reactions have already taken place in this sample.

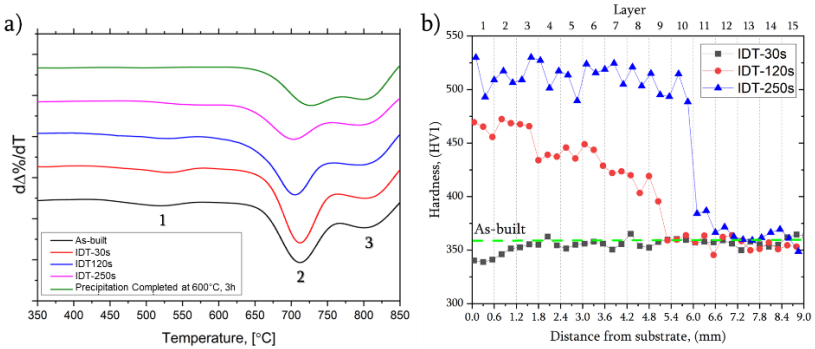


Figure 4-46 a) dilatometry curves for the Ab specimen and samples prepared with different IDT, b) Hardness profiles along the build height for all samples

The hardness profiles along the build height are shown in Figure 4-46b and the results are in good agreement with dilatometry curves. The hardness profile in IDT-30s is relatively flat and shows an average of ~360 HV1 comparable to the as-built hardness of steel. In the IDT-120s specimen, hardness is increased to 470 HV1 in the bottom layers, followed by a gradual decrease to around 400 HV1 at 5mm far from the substrate, followed by a sudden drop to around 360 HV1 (i.e., as-built hardness) up to the top. This is in line with the simulated thermal cycles and the optical micrographs showing that the top layers could not be age-hardened. Indeed, the thermal history in the top layers leads to an annealing process. The hardness profile in the IDT-250s scenario reaches a nearly constant value of 520 HV1 up to 3 mm from the top. This value drops to 360 HV1 in agreement with the abovementioned description. According to the simulations, the total height of the minimum successive deposited layers required to trigger aging in the below layers (i.e., in IDT-250s→ y=4), is around 2.5 mm with the current processing parameters. This is in very good agreement with the height of the non-aged region, both in view of hardness measurements and the optical micrographs. Similar behavior was observed in the work of Kürnsteiner et al. [141] on an experimentally tailored maraging steel.

The compressive stress-strain curves of the samples compressed to 10% true strain show that the IDT-250s sample has a yield strength of 1810±21 MPa, decreasing to 1675±23 MPa for 120P-s. The as-built material, with no pause applied, shows a compressive strength of 1205±29 MPa (Figure 4-47).

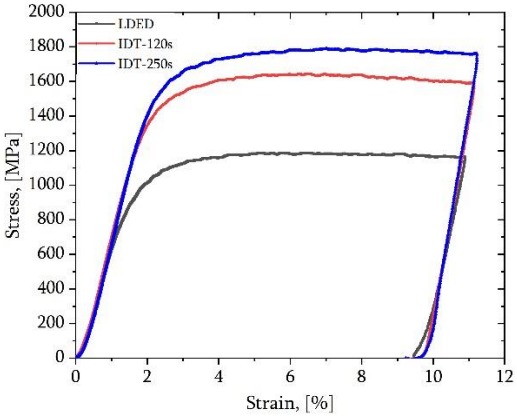


Figure 4-47 Compressive stress-strain curves of as-built, IDT-120s, and IDT-250s samples

### 4.3.6 Other Design Possibilities

In this section, other potential design advantages of LDED, namely the production of bimetals, in-situ mixing of materials, and fabrication of compositionally graded materials, are investigated. In order to benefit from the ultrahigh hardness of the Osprey® MAR-60HRC, a bimetal with Osprey® 18Ni300 steel as the core and Osprey® MAR-60HRC on the surface was deposited. The benefit of using Osprey® 18Ni300 is its high toughness at high hardness levels, along with its compatible chemical composition with Osprey® MAR-60HRC. The latter theoretically leads to the formation of a sound and strong interface without the presence of parasitic reaction phases.

#### 4.3.6.1 Microstructural characterization

An epitaxial dendrite growth can be observed in the first layer of Osprey® MAR-60HRC deposited on the Osprey® 18Ni300, implying a defect-free and compatible interface between the two materials (Figure 4-48a).

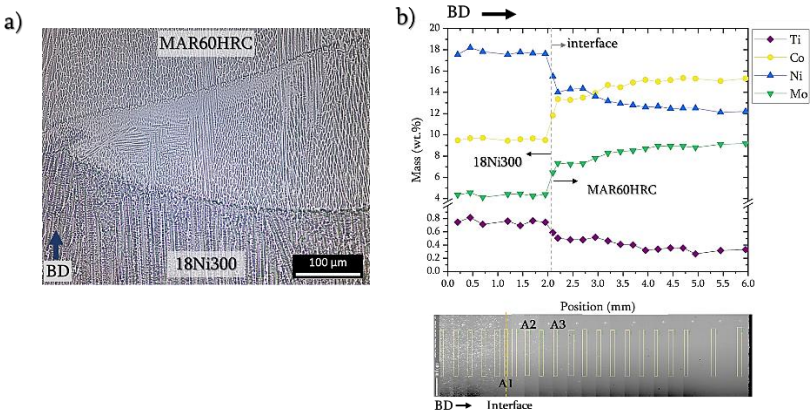


Figure 4-48 a) LOM micrograph showing the interface in as-deposited bimetal, b) EDS analysis results for Ti, Co, Ni, and Mo along the height of bimetal, and the SEM micrograph showing the areas considered for EDS

The change in the chemical composition, starting from the Osprey® 18Ni300 core and passing through the interface towards Osprey® MAR-60HRC at the top surface (see Figure 4-48a and Table 4-9), is plotted using EDS analysis (Figure 4-48b). The plot shows a drop in Ni and Ti wt.% to ~15.5 and 0.6 in the first deposited layer of Osprey® MAR-60HRC at the interface, while Mo and Co increase significantly to around 6.4 wt.% and 12.0 wt.% respectively (zone A1, Figure 4-48a and Table 4-9).

By approaching the second layer of Osprey® MAR-60HRC, Ni content further decreases to ~14.0 wt.%, and Ti to ~0.5 wt.%, while Mo and Co increase to 7.3 wt.% and 14.0 wt.%, respectively (zone A2, Figure 4-48a and Table 4-9). Within the 3rd layer of the deposited Osprey® MAR-60HRC, the concentration profiles become relatively flat, and the chemical composition detected by EDS approaches the nominal Osprey® MAR-60HRC composition (zone A3, Figure 4-48a and Table 4-9). For comparison, the theoretical chemical composition in the case of mixing the two powders at equal wt.% (i.e., 50/50) is shown in Table 4-9. The results indicate that a mixture of Osprey® 18Ni300 and Osprey® MAR-60HRC characterizes the vicinity of the interface, showing an equivalent chemical composition in between the starting materials, which can be roughly said to comprise ~50 wt.% Osprey® 18Ni300, Osprey® MAR-60HRC bal. By increasing the distance from the interface, the material gradually is diluted in Osprey® 18Ni300 and approaches the pure Osprey® MAR-60HRC composition; this is achieved roughly at the top surface of the 3rd deposited layer of Osprey® MAR-60HRC onwards.

Table 4-9 Composition of different layers near the interface of the bimetal, wt.%

| Zone/ Elements | Ni | Co | Mo | Ti | Fe |
|---|---|---|---|---|---|
| **Osprey® 18Ni300** | 18.2 | 9.7 | 4.6 | 0.8 | bal. |
| **A1** | 15.5 | 11.8 | 6.4 | 0.6 | bal. |
| **A2** | 14.0 | 13.4 | 7.3 | 0.5 | bal. |
| **A3** | 13.3 | 14.0 | 8.3 | 0.4 | bal. |
| **OSPREY® MAR-60HRC** | 12.7 | 15.0 | 9.0 | 0.3 | bal. |
| **50%-50% nominal mix** | 15.5 | 12.2 | 7.3 | 0.5 | bal. |

With reference to the simulation of the thermal histories of the deposited layers presented in section 4.3.5, it is plausible that by the deposition of the first layer of Osprey® MAR-60HRC, the last deposited layer of Osprey® 18Ni300 partially remelts, and the mixing of these materials takes place in the liquid state due to the Marangoni effect. This should probably lead to a composition that roughly contains 50 wt. % Osprey® 18Ni300, and 50 wt. % Osprey® MAR-60HRC at the vicinity of the interface (i.e., mixed layer 1, corresponding to regions in the 1$^{st}$ deposited layer of Osprey® MAR-60HRC). By depositing the second layer of Osprey® MAR-60HRC, the solidified layer (mixed layer 1) is partially remelted and mixed with the Osprey® MAR-60HRC, and the equivalent solidified composition may become roughly 25wt.% Osprey® 18Ni300, and 75wt.% Osprey® MAR-60HRC (i.e., mixed layer 2). The successive depositions probably result in a highly diluted composition in Osprey® 18Ni300, which can be considered pure Osprey® MAR-60HRC. Moreover, due to the heat transfer from the solidifying layers to the solidified layers, the concentration gradients might lead to interdiffusion at high temperatures in the solid state. This discussion is essential as it will be used later to describe the hardness profile of the bimetal. Given the compatible chemical compositions of the two alloys, the smooth concentration profiles of the alloying elements near the interface, and the SEM micrographs, no parasitic reaction phases at the interface are expected.

The hardness profiles (Figure 4-49a) before and after the age hardening of the bimetal confirm that the as-built hardness of the Osprey® 18Ni300 is around 325 HV. By approaching the interface, the hardness increases to about 340 HV and rises gradually to around 370 HV in the Osprey® MAR-60HRC region, in line with the aging curves of the two base materials (Figure 4-39).

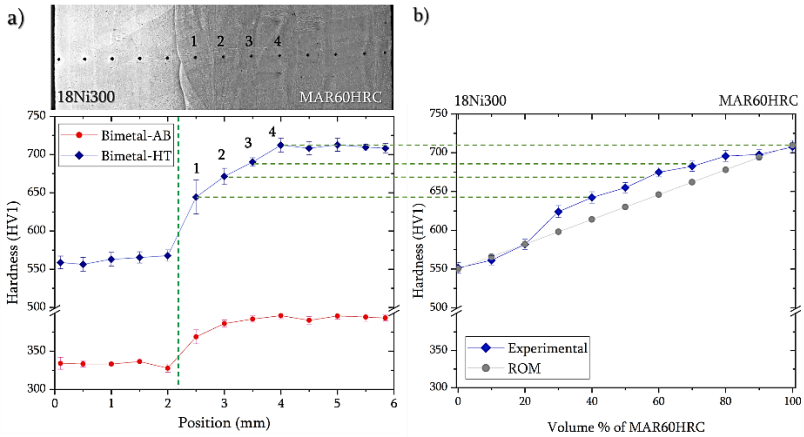


Figure 4-49 Hardness profile across the height for the bimetal samples in the as-built and aged states, b) Hardness profile of the CG sample experimental and ROM

In the aged condition, a similar trend is observed. Hardness in Osprey® 18Ni300 is around 560 HV and increases to 650 HV at the interface, followed by a gradual increase to ~720 HV. The hardness gradient at the interface covers around 2 mm, roughly representative of three deposited layers (layer thickness ~0.7 mm), which is in agreement with the chemical composition gradient near the interface, where mixing of the softer Osprey® 18Ni300 with Osprey® MAR-60HRC was evident. In order to further investigate the dilution influence on the hardness, a compositionally graded (CG) sample was produced through an in-situ mixture of powders and by increasing the amount of Osprey® MAR-60HRC by 10 vol. % in each successive layer. The experimental hardness profile and the calculated hardness profile based on the rule of mixture (ROM) are depicted in Figure 4-49b. The hardness according to ROM ($H_{ROM}$) can be calculated according to Eq. 4-7:

$$H_{ROM} = H_{MAR60}V_{MAR60} + H_{18Ni300}V_{18Ni300} \quad \text{(Eq. 4-7)}$$

where H and V represent the hardness and volume fraction for each material, respectively. The experimental hardness profile and the calculated hardness profile based on the rule of mixture (ROM) are depicted in Figure 4-49b.

The microhardness at point 1 in Figure 4-49a is equal to the microhardness of the layer with 40 vol. % of Osprey® MAR-60HRC in Figure 4-49b. In the second layer, covering points 2, and 3 in Fig. 8a, the microhardness in bimetal lies in between the hardness levels of 60 to 70 vol% of Osprey® MAR-60HRC (see Figure 4-49b). At the top of the third deposited layer (point 4 in Figure 4-49a), the microhardness approaches that of 100% Osprey® MAR-60HRC (see Figure 4-49b). The microhardness doesn't change further from point 4 towards the top layers of the bimetal, therefore, still corresponding to the hardness of pure Osprey® MAR-60HRC. Together with the EDS analysis, these results can appropriately explain the interface characteristics.

The discrepancy between the ROM and experimental results can be due to the change in precipitation kinetics by changing Mo, Ti, and Co content in the mixtures. In Osprey® 18Ni300 with 0.6-0.8 wt.% Ti, $Ni_3Ti$ is one of the main precipitates to form at 400°C to 500°C aging interval; this is accompanied by the precipitation of Mo-rich intermetallic particles (e.g., $Ni_3Mo$) [204]. By increasing Mo and decreasing Ti in the mixtures, which comprise higher vol.% of Osprey® MAR-60HRC, the activity of Mo increases; moreover, the increase in Co wt.% decreases the solubility of Mo in the matrix. The combination of these two factors enhances the precipitation of the $Ni_3Mo$, while $Ni_3Ti$ will still be present as a result of the higher Ti content in the mixtures compared with the pure Osprey® MAR-60HRC. The morphology and size of these two precipitates at the aging temperature differ from each other [205], leading to different contributions to strength according to the Orowan relation. This can lead to an increased experimental hardness compared with the theoretical ROM results. Interestingly, when the vol.% of Osprey® MAR-60HRC in the mixture is either low (i.e., up to 20%) or high ( i.e., 90%), the experimental hardness is identical to that of ROM; therefore, there exists a threshold above which, the precipitation kinetics will be affected by the introduction of the second material. This needs to be further analyzed in future works using thermal analysis.

#### 4.3.6.2 Fracture toughness

Figure 4-50Figure 3-5a presents the schematic of the samples prepared for fracture toughness tests. Tests were performed on samples after aging (480 ˚C, 5h).

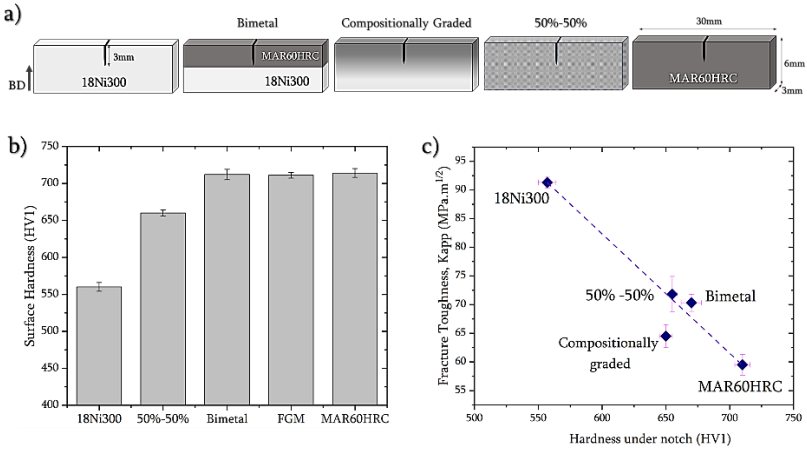


Figure 4-50 a) Schematic of the FT samples, b) surface hardness of FT samples, and c) Kapp values for the samples versus hardness under the notch

The Kapp of the Osprey® 18Ni300 at 565± 6 HV is 90±2 MPa $m^{1/2}$, and this value drops to 60±3 MPa $m^{1/2}$ for Osprey® MAR-60HRC at 725±8 HV. The Bi-Metal shows a fracture toughness of 71±2 MPa $m^{1/2}$ at a similar surface hardness level of Osprey® MAR-60HRC (Figure 4-50b). The higher toughness of bimetal compared with Osprey® MAR-60HRC can be attributed to the influence of concentration and hardness gradient near the interface. The notch tip was located in an area showing a hardness of ~670HV (Figure 4-50c), which is equal to the hardness of a mixture of 50% Osprey® MAR-60HRC, Osprey® 18Ni300 bal. (see Figure 4-49b). The lower hardness below the notch leads to higher Kapp in bimetal. In order to confirm this hypothesis, fracture toughness tests were carried out on samples processed by the 50%-50% mixtures of Osprey® MAR-60HRC and Osprey® 18Ni300. The fracture toughness of the 50%-50% samples, showing a hardness level of 660 HV, perfectly lies in between Osprey® 18Ni300 and Osprey® MAR-60HRC (Figure 4-50c) and matches with that of bimetal if hardness under notch is taken into account for the latter. It is evident that the bimetal with a very high surface hardness shows excellent fracture toughness as well, shifting its position to the right side of the hardness-toughness linear trend. This is mainly due to a defect-free interface and the concentration and hardness gradients below the notch. The fracture toughness obtained in this work for Osprey® 18Ni300 and Osprey® MAR-60HRC is systematically higher than those of conventionally manufactured maraging counterparts at the same hardness level (see Figure 1-4). As discussed earlier in the experimental section, this is a consequence of the larger notch tip radius in the

current study compared with the fatigue pre-cracked notch. This systematic difference was also documented in other works [54], where the fracture toughness of the tool steels by using a fatigue pre-cracked notch (i.e., $\rho \rightarrow 0$) was lower than those performed on the EDM notched samples with a notch radius of 50 µm.

The fracture surface of Osprey® 18Ni300 shows ductile transgranular fracture with the presence of dimples (Figure 4-51a). The fracture surface of the Osprey® MAR-60HRC, on the other hand, shows a quasi-cleavage fracture behavior, a preferential crack propagation along the columnar grains and dendritic substructure can be observed, but it is hard to be concluded as an intergranular fracture (Figure 4-51c). The crack interaction with the interface in the bimetal sample will be discussed in the next section.

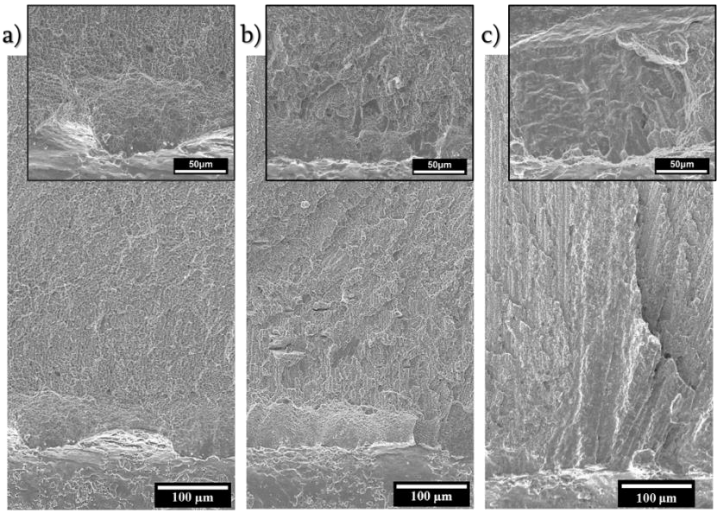


Figure 4-51 SEM images of the fracture surfaces for a)Osprey® 18Ni300 and b)50%-50% specimen, and c) Osprey® MAR-60HRC

#### 4.3.6.3 Crack interaction with Interface in bimetal

The load-displacement curves in Osprey® 18Ni300 show that after reaching the maximum force (i.e., the onset of crack initiation), the load drops instantaneously due to the unstable crack propagation until complete fracture (Figure 4-52a). Signs of limited plastic deformation before reaching the maximum load were evident in the load-displacement records. However, drawing the 5% secant line following the ASTM E399 recommendation did not significantly change the fracture toughness calculations. The records for the Osprey® MAR-60HRC is also showing a similar

sudden load drop after reaching the maximum load, and the load-displacement curve obeys a perfect linear elastic behavior.

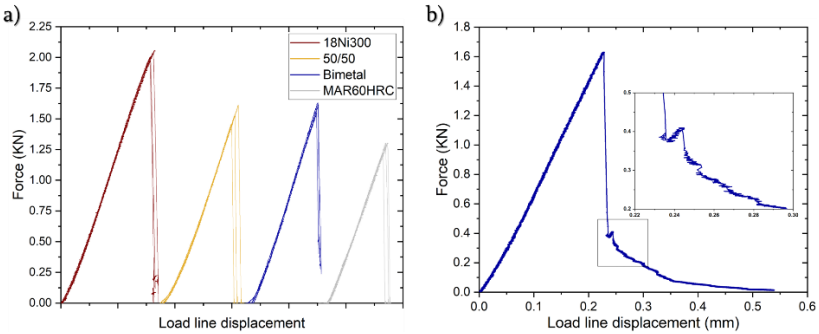


Figure 4-52 a) Load displacement curves for the fracture toughness tests and b) load pop-in for the bimetal

The load-displacement record in bimetal is different, and it shows a maximum, followed by a sudden drop to around 0.4 kN, representing the unstable crack propagation up to that point (Figure 4-52a) and not reaching zero without showing a complete fracture. At this point, to further understand the crack propagation behavior, the test was conducted for one sample with sustained loading until complete fracture (Figure 4-52b). Looking at the load-displacement curve, the appearance of a pop-in is obvious (inset in Figure 4-52b), where the force slightly increases after the sudden drop and again starts to decrease gradually until complete fracture. This behavior can be related to a decline in the driving force for crack propagation and crack arrest in the microstructure. Thus a larger driving force was needed for the crack propagation.

Interestingly, the metallographic cross-section prepared after stopping the test before the occurrence of the pop-in shows that the propagating crack in the Osprey® MAR-60HRC region is arrested at the interface due to the shielding effect of the tougher Osprey® 18Ni300 (Figure 4-53a) in agreement with the load-displacement curve.

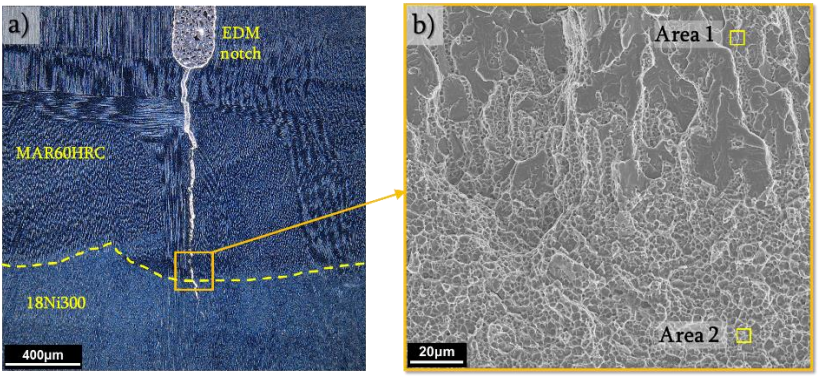


Figure 4-53 a) DF-LOM image highlighting the crack propagation path in the bimetal samples, and b) SEM image of the fracture at the interface of the two materials, demonstrating the transition of fracture mode.

The crack propagation path in bi-material layered structures is governed by a competition between the direction of the "maximum" driving force and the "weakest" microstructural path [206]. This experiment shows that the original crack, "perpendicular" to the interface, does not deflect towards the interface when approaching it. Therefore, the interface was not the "weakest" microstructural path. This can be another indication of a strong and defect-free interface, thanks to the very compatible chemical composition of the two materials. Moreover, by continuing the loading, the crack propagates in the Osprey® 18Ni300, and the fracture surface at the interface shows a transition from a quasi-cleavage fracture in Osprey® MAR-60HRC to a transgranular ductile fracture in Osprey® 18Ni300 with no traces of decohesion or transversal cracking at the interface (Figure 4-53b).

Table 4-10 Chemical composition of two areas at fracture interface of the bimetal, in wt.%

| Element | Fe | Ni | Co | Mo | Ti |
|---|---|---|---|---|---|
| **Area 1** | 64.7 | 13.7 | 13.5 | 7.8 | 0.4 |
| **Area 2** | 64.1 | 18.1 | 9.9 | 5.3 | 0.9 |

This is also supported by the EDS analysis on Area 1 (The first deposited layer of Osprey® MAR-60HRC) and area 2 (Osprey® 18Ni300) in the vicinity of the interface (

Table 4-10). Apart from the improved $K_{app}$ of bimetal compared with Osprey® MAR-60HRC, the crack arrest at the interface (i.e., extrinsic toughening effect) can account for an increased damage tolerance factor in industrial applications.

### 4.3.7 Conclusions

- As-built microstructure of Osprey® MAR-60HRC comprised martensite and a small vol.% of intercellular retained austenite because of heavy micro-segregation of alloying elements to the cellular boundaries.
- Direct aging at 480 ˚C for 6h resulted in a high hardness (~720 HV) for the Osprey® MAR-60HRC, about 180 HV higher than reference Osprey® 18Ni300. Aging at higher temperatures resulted in earlier hardness drop due to austenite reversion and precipitate coarsening.
- Direct aging at 480 ˚C for 5h resulted in the highest achievable hardness and compressive strength for the LDEDed Osprey® MAR-60HRC (i.e., >700 HV and >2400 MPa). Aging for the same duration at 525 ˚C resulted in overaging and promoted austenite reversion. Solution annealing of the samples prior to age hardening further increased hardness and compressive strength to around 730 HV and 2600 MPa, respectively.
- Osprey® MAR-60HRC maraging steel with higher Mo and Co content to enhance age-hardening response and higher hardness was successfully deposited to exploit the IHT. Adopting a proper pause strategy to trigger massive in-situ nano-precipitation increased hardness and yield strength. These results are encouraging as they demonstrate the possibility of eliminating post-processing aging treatment. Results also indicate the feasibility of tailoring the mechanical properties by selecting different pause strategies with the aid of already validated thermal history simulation tools.
- The fracture toughness of Osprey® MAR-60HRC at the peak aged condition was lower than that of Osprey® 18Ni300 (i.e., 60 MPa $m^{1/2}$ vs. 90 MPa $m^{1/2}$).
- Bi-metal samples were deposited successfully with a high-toughness core of Osprey® 18Ni300 and a hard surface of Osprey® MAR-60HRC. A smooth microstructural and hardness transition could be observed without evident interface defects. The fracture toughness of the bimetal (i.e., 71 MPa $m^{1/2}$) was higher than that of Osprey® MAR-60HRC and lower than Osprey® 18Ni300, while the surface hardness of the bimetal was equal to that of Osprey® MAR-60HRC (~720 HV1).
- Besides the improved fracture toughness, the crack arrest at the interface was evidenced in the bimetal with a hard surface and a softer core. This

extrinsic toughening effect can be of high interest when designing a damage-tolerant material.

# Chapter 5

# Conclusions and Future Prospective

The purpose of this thesis was to contribute to the expansion of knowledge regarding heat treatment for additively manufactured tool steels, in particular LDED. Due to the peculiar features inherent to additive manufacturing, the microstructure of the LAM processed tool steels are different from those conventionally processed, and hence different heat treatment strategies might be applied. It was demonstrated that despite the anisotropy in mechanical properties, direct tempering of carbon-bearing tool steels, namely H13 and X35CrMoMn7-2-1 (Ferro55), can be a favorable alternative given the acceptable fracture toughness and better tempering resistance. This was because similar hardness values could be obtained through direct tempering at higher temperatures which can prolong the material's resistance to thermal softening during the service. Moreover, the costly step of austenitization at high temperatures can be avoided. It was also demonstrated that Ferro55 could be a suitable alternative for H13 in a variety of applications due to its simple processability and greater fracture toughness at comparable hardness values. Although, the lack of vanadium and a higher coarsening rate of Cr carbides in this grade confines its application for high-temperature purposes. For a more accurate conclusion between the two heat treatment scenarios of DT and QT, more dynamic testing, such as fatigue, must be conducted in future works. Furthermore, the thermal fatigue of these two grades needs to be studied and compared in the QT and DT states.

In the second part of the work dealing with maraging steels, a new commercial alloy Osprey® MAR-60HRC designed for higher hardness and more demanding applications was investigated. Processing parameters for LDED were developed, and the aging curves for this material were obtained. Moreover, given the fast aging response of this alloy, the feasibility of intrinsic heat treatment was investigated with the aid of thermal simulations. It was shown that in-situ aging of maraging steel might be achieved by applying an appropriate interlayer dwell time and customizing the thermal history of the component. This can be of great importance, specifically in repairing applications, where local heat treatment in the selected area can be applied. Another application can be the fabrication of functionally graded parts where different locations can demonstrate dissimilar properties at different locations of the part. Evidently, this requires a careful design of the thermal history

in parts. In addition, geometrical characteristics and the size of the component might influence the thermal history and, subsequently, the IHT behavior, which requires extensive research.

Considering the wear resistance issue in maraging steels and given the considerably high hardness of Osprey® MAR-60HRC and its low fracture toughness, the fabrication of bimetallic specimens with a tough core of Osprey® 18Ni300 and a hard surface of Osprey® MAR-60HRC was investigated as a possible solution. A bimetal with a defect-free interface was realized due to the similar composition of the two materials by the in-situ mixture of the two powders to obtain a functional part that can combine both high hardness and toughness. This is especially an advantage since most of the currently available maraging steels have problems with wear resistance, and a practical way to face this issue is to increase the hardness. The fabrication of compositionally graded samples was also investigated, and despite having the same surface hardness, the specimens' fracture toughness was lower than the bimetal samples. This might highlight the role of crack arrest that occurs at the interface in bimetal samples. In future works, the wear resistance of the bimetal and CGM specimens will be evaluated and compared to H13 tool steel through pin-on-disk experiments. Moreover, due to faster responses of the Osprey® MAR-60HRC to aging, the thermal softening (overaging) of the bimetal and CGM parts should be investigated in future activities.

## References


[1] 14:00-17:00, “ISO/ASTM 52900:2021.” Accessed: Mar. 21, 2022. [Online]. Available: https://www.iso.org/cms/render/live/en/sites/isoorg/contents/data/standard/07/45/74514.html

[2] N. Guo and M. C. Leu, “Additive manufacturing: technology, applications and research needs,” *Front. Mech. Eng.*, vol. 8, no. 3, pp. 215–243, Sep. 2013, doi: 10.1007/s11465-013-0248-8.

[3] I. Gibson, D. W. Rosen, B. Stucker, and M. Khorasani, *Additive manufacturing technologies*, 3rd ed., vol. 17. Springer, 2021.

[4] M. Yakout, M. A. Elbestawi, and S. C. Veldhuis, “A Review of Metal Additive Manufacturing Technologies,” *Solid State Phenom.*, vol. 278, pp. 1–14, 2018, doi: 10.4028/www.scientific.net/SSP.278.1.

[5] J. P. M. Pragana, R. F. V. Sampaio, I. M. F. Bragança, C. M. A. Silva, and P. A. F. Martins, “Hybrid metal additive manufacturing: A state–of–the-art review,” *Adv. Ind. Manuf. Eng.*, vol. 2, p. 100032, May 2021, doi: 10.1016/j.aime.2021.100032.

[6] C. Sun, Y. Wang, M. D. McMurtrey, N. D. Jerred, F. Liou, and J. Li, “Additive manufacturing for energy: A review,” *Appl. Energy*, vol. 282, p. 116041, Jan. 2021, doi: 10.1016/j.apenergy.2020.116041.

[7] D. Herzog, V. Seyda, E. Wycisk, and C. Emmelmann, “Additive manufacturing of metals,” *Acta Mater.*, vol. 117, pp. 371–392, Sep. 2016, doi: 10.1016/j.actamat.2016.07.019.

[8] N. Asnafi, “Tool and Die Making, Surface Treatment, and Repair by Laser-based Additive Processes,” *BHM Berg- Hüttenmänn. Monatshefte*, vol. 166, no. 5, pp. 225–236, May 2021, doi: 10.1007/s00501-021-01113-2.

[9] J. C. Najmon, S. Raeisi, and A. Tovar, “2 - Review of additive manufacturing technologies and applications in the aerospace industry,” in *Additive Manufacturing for the Aerospace Industry*, F. Froes and R. Boyer, Eds. Elsevier, 2019, pp. 7–31. doi: 10.1016/B978-0-12-814062-8.00002-9.

[10] T. DebRoy *et al.*, “Additive manufacturing of metallic components – Process, structure and properties,” *Prog. Mater. Sci.*, vol. 92, pp. 112–224, Mar. 2018, doi: 10.1016/j.pmatsci.2017.10.001.

[11] S. A. M. Tofail, E. P. Koumoulos, A. Bandyopadhyay, S. Bose, L. O'Donoghue, and C. Charitidis, "Additive manufacturing: scientific and technological challenges, market uptake and opportunities," *Mater. Today*, vol. 21, no. 1, pp. 22–37, Jan. 2018, doi: 10.1016/j.mattod.2017.07.001.

[12] J.-F. Romainville and F. Bley, "EU Market for 3DP Demonstration Equipment and Services – Final Report," *3DP PAN EU*, Dec. 2021. https://3dppan.eu/ (accessed Mar. 28, 2022).

[13] D.-G. Ahn, "Direct metal additive manufacturing processes and their sustainable applications for green technology: A review," *Int. J. Precis. Eng. Manuf.-Green Technol.*, vol. 3, no. 4, pp. 381–395, Oct. 2016, doi: 10.1007/s40684-016-0048-9.

[14] S. M. Thompson, L. Bian, N. Shamsaei, and A. Yadollahi, "An overview of Direct Laser Deposition for additive manufacturing; Part I: Transport phenomena, modeling and diagnostics," *Addit. Manuf.*, vol. 8, pp. 36–62, Oct. 2015, doi: 10.1016/j.addma.2015.07.001.

[15] W. E. Frazier, "Metal Additive Manufacturing: A Review," *J. Mater. Eng. Perform.*, vol. 23, no. 6, pp. 1917–1928, Jun. 2014, doi: 10.1007/s11665-014-0958-z.

[16] A. Standard, "F3187-16 Standard Guide for Directed Energy Deposition of Metals," *ASTM Int. West Conshohocken PA USA*, 2016.

[17] D. M. Keicher and W. D. Miller, "LENSTM moves beyond RP to direct fabrication," *Met. Powder Rep.*, vol. 53, no. 12, pp. 26–28, 1998, doi: 10.1016/S0026-0657(99)80073-3.

[18] J. W. Sears, "Direct laser powder deposition-'State of the Art'," Knolls Atomic Power Lab., Niskayuna, NY (US), 1999.

[19] J. Mazumder, D. Dutta, N. Kikuchi, and A. Ghosh, "Closed loop direct metal deposition: art to part," *Opt. Lasers Eng.*, vol. 34, no. 4, pp. 397–414, Oct. 2000, doi: 10.1016/S0143-8166(00)00072-5.

[20] J. Choi, "Process and properties control in laser aided direct metal/materials deposition process," in *ASME International Mechanical Engineering Congress and Exposition*, 2002, vol. 3641, pp. 81–89.

[21] D. Svetlizky *et al.*, "Directed energy deposition (DED) additive manufacturing: Physical characteristics, defects, challenges and applications," *Mater. Today*, vol. 49, pp. 271–295, Oct. 2021, doi: 10.1016/j.mattod.2021.03.020.

[22] R. P. Martukanitz, “Additive Manufacturing Processes,” in *Directed-Energy Deposition Processes*, 2020, pp. 220–238. Accessed: Oct. 19, 2022. [Online]. Available: https://dl.asminternational.org/handbooks/edited-volume/119/chapter/2348120/Directed-Energy-Deposition-Processes

[23] B. Bax, R. Rajput, R. Kellet, and M. Reisacher, “Systematic evaluation of process parameter maps for laser cladding and directed energy deposition,” *Addit. Manuf.*, vol. 21, pp. 487–494, May 2018, doi: 10.1016/j.addma.2018.04.002.

[24] J. Kummailil, C. Sammarco, D. Skinner, C. A. Brown, and K. Rong, “Effect of Select LENS™ Processing Parameters on the Deposition of Ti-6Al-4V,” *J. Manuf. Process.*, vol. 7, no. 1, pp. 42–50, Jan. 2005, doi: 10.1016/S1526-6125(05)70080-3.

[25] K. Zhang, S. Wang, W. Liu, and X. Shang, “Characterization of stainless steel parts by Laser Metal Deposition Shaping,” *Mater. Des.*, vol. 55, pp. 104–119, Mar. 2014, doi: 10.1016/j.matdes.2013.09.006.

[26] M. Ziętala *et al.*, “The microstructure, mechanical properties and corrosion resistance of 316L stainless steel fabricated using laser engineered net shaping,” *Mater. Sci. Eng. A*, vol. 677, pp. 1–10, Nov. 2016, doi: 10.1016/j.msea.2016.09.028.

[27] J. L. Bennett, S. J. Wolff, G. Hyatt, K. Ehmann, and J. Cao, “Thermal effect on clad dimension for laser deposited Inconel 718,” *J. Manuf. Process.*, vol. 28, pp. 550–557, Aug. 2017, doi: 10.1016/j.jmapro.2017.04.024.

[28] G. Wang, X. Sun, M. Huang, Y. Qin, Y. Yao, and S. Yang, “Influence of processing parameters on the microstructure and tensile property of 85 W-15Ni produced by laser direct deposition,” *Int. J. Refract. Met. Hard Mater.*, vol. 82, pp. 227–233, Aug. 2019, doi: 10.1016/j.ijrmhm.2019.04.016.

[29] L. Tang, J. Ruan, R. G. Landers, and F. Liou, “Variable Powder Flow Rate Control in Laser Metal Deposition Processes,” *J. Manuf. Sci. Eng.*, vol. 130, no. 4, Jul. 2008, doi: 10.1115/1.2953074.

[30] F. Xing, W. Liu, and T. Wang, “Real-time Sensing and Control of Metal Powder Laser Forming,” in *2006 6th World Congress on Intelligent Control and Automation*, Jun. 2006, vol. 2, pp. 6661–6665. doi: 10.1109/WCICA.2006.1714372.

[31] G. Pi, A. Zhang, G. Zhu, D. Li, and B. Lu, “Research on the forming process of three-dimensional metal parts fabricated by laser direct metal forming,”

*Int. J. Adv. Manuf. Technol.*, vol. 57, no. 9, pp. 841–847, Dec. 2011, doi: 10.1007/s00170-011-3404-5.

[32] E. Fearon and K. G. Watkins, "Optimisation of layer height control in direct laser deposition," *Int. Congr. Appl. Lasers Electro-Opt.*, vol. 2004, no. 1, p. 1708, Oct. 2004, doi: 10.2351/1.5060232.

[33] U. Chadha *et al.*, "Directed Energy Deposition via Artificial Intelligence-Enabled Approaches," *Complexity*, vol. 2022, p. e2767371, Sep. 2022, doi: 10.1155/2022/2767371.

[34] N. Shamsaei, A. Yadollahi, L. Bian, and S. M. Thompson, "An overview of Direct Laser Deposition for additive manufacturing; Part II: Mechanical behavior, process parameter optimization and control," *Addit. Manuf.*, vol. 8, pp. 12–35, Oct. 2015, doi: 10.1016/j.addma.2015.07.002.

[35] W. J. Sames, F. A. List, S. Pannala, R. R. Dehoff, and S. S. Babu, "The metallurgy and processing science of metal additive manufacturing," *Int. Mater. Rev.*, vol. 61, no. 5, pp. 315–360, Jul. 2016, doi: 10.1080/09506608.2015.1116649.

[36] W. Hofmeister and M. Griffith, "Solidification in direct metal deposition by LENS processing," *JOM*, vol. 53, no. 9, pp. 30–34, Sep. 2001, doi: 10.1007/s11837-001-0066-z.

[37] D.-R. Liu, S. Wang, and W. Yan, "Grain structure evolution in transition-mode melting in direct energy deposition," *Mater. Des.*, vol. 194, p. 108919, Sep. 2020, doi: 10.1016/j.matdes.2020.108919.

[38] T. T. Roehling *et al.*, "Modulating laser intensity profile ellipticity for microstructural control during metal additive manufacturing," *Acta Mater.*, vol. 128, pp. 197–206, Apr. 2017, doi: 10.1016/j.actamat.2017.02.025.

[39] S. Mitzner, S. Liu, M. S. Domack, and R. A. Hafley, "Grain Refinement of Freeform Fabricated Ti-6Al-4V Alloy Using Beam/Arc Modulation," presented at the 23rd Annual International Solid Freeform Fabrication Symposium, Austin, TX, Aug. 2012. Accessed: Nov. 07, 2022. [Online]. Available: https://ntrs.nasa.gov/citations/20120014597

[40] P. Kürnsteiner, M. B. Wilms, A. Weisheit, B. Gault, E. A. Jägle, and D. Raabe, "High-strength Damascus steel by additive manufacturing," *Nature*, vol. 582, no. 7813, Art. no. 7813, Jun. 2020, doi: 10.1038/s41586-020-2409-3.

[41] Y. Tian *et al.*, “Rationalization of Microstructure Heterogeneity in INCONEL 718 Builds Made by the Direct Laser Additive Manufacturing Process,” *Metall. Mater. Trans. A*, vol. 45, pp. 4470–4483, Sep. 2014, doi: 10.1007/s11661-014-2370-6.

[42] D. Svetlizky *et al.*, “Directed energy deposition of Al 5xxx alloy using Laser Engineered Net Shaping (LENS®),” *Mater. Des.*, vol. 192, p. 108763, Jul. 2020, doi: 10.1016/j.matdes.2020.108763.

[43] H. Knoll, S. Ocylok, A. Weisheit, H. Springer, E. Jägle, and D. Raabe, “Combinatorial Alloy Design by Laser Additive Manufacturing,” *Steel Res. Int.*, vol. 88, no. 8, p. 1600416, 2017, doi: https://doi.org/10.1002/srin.201600416.

[44] T. Niendorf *et al.*, “Functionally Graded Alloys Obtained by Additive Manufacturing,” *Adv. Eng. Mater.*, vol. 16, no. 7, pp. 857–861, 2014, doi: 10.1002/adem.201300579.

[45] A. Bandyopadhyay and B. Heer, “Additive manufacturing of multi-material structures,” *Mater. Sci. Eng. R Rep.*, vol. 129, pp. 1–16, Jul. 2018, doi: 10.1016/j.mser.2018.04.001.

[46] G. A. Roberts, R. Kennedy, and G. Krauss, *Tool Steels, 5th Edition*. ASM International, 1998.

[47] R. A. Mesquita, *Tool Steels: Properties and Performance*. CRC Press, 2016.

[48] Wright, P. K. and Trent, E. M., *Metal Cutting - 4th Edition*, 4th ed. Elsevier Science Ltd, 2000. Accessed: Nov. 06, 2022. [Online]. Available: https://www.elsevier.com/books/metal-cutting/wright/978-0-7506-7069-2

[49] F. Hippenstiel, V. Lubich, P. Vetter, and W. Grimm, *Handbook of plastic mould steels*. Edelstahlwerke Buderus AG Wetzlar, 2004.

[50] Materials Park, “ASTM A681-08 Standard Specification for Tool Steels Alloy.” OH: ASTM International. Accessed: Oct. 19, 2022. [Online]. Available: https://www.astm.org/a0681-08r15.html

[51] P. Bajaj, A. Hariharan, A. Kini, P. Kürnsteiner, D. Raabe, and E. A. Jägle, “Steels in additive manufacturing: A review of their microstructure and properties,” *Mater. Sci. Eng. A*, vol. 772, p. 138633, Jan. 2020, doi: 10.1016/j.msea.2019.138633.

[52] K. Kempen, B. Vrancken, S. Buls, L. Thijs, J. Van Humbeeck, and J.-P. Kruth, “Selective Laser Melting of Crack-Free High Density M2 High Speed

Steel Parts by Baseplate Preheating," *J. Manuf. Sci. Eng.*, vol. 136, no. 6, Oct. 2014, doi: 10.1115/1.4028513.

[53] G. Gong *et al.*, "Research status of laser additive manufacturing for metal: a review," *J. Mater. Res. Technol.*, vol. 15, pp. 855–884, Nov. 2021, doi: 10.1016/j.jmrt.2021.08.050.

[54] A. Ankara and H. B. Ari, "Determination of hot crack susceptibility in various kinds of steels," *Mater. Des.*, vol. 17, no. 5, pp. 261–265, Jan. 1996, doi: 10.1016/S0261-3069(97)00019-8.

[55] A. Simchi, "Direct laser sintering of metal powders: Mechanism, kinetics and microstructural features," *Mater. Sci. Eng. A*, vol. 428, no. 1, pp. 148–158, Jul. 2006, doi: 10.1016/j.msea.2006.04.117.

[56] G. Y. Baek, G. Y. Shin, K. Y. Lee, and D. S. Shim, "Mechanical Properties of Tool Steels with High Wear Resistance via Directed Energy Deposition," *Metals*, vol. 9, no. 3, p. 282, Mar. 2019, doi: 10.3390/met9030282.

[57] S. Kapil, F. Legesse, S. Negi, K. P. Karunakaran, and S. Bag, "Hybrid layered manufacturing of a bimetallic injection mold of P20 tool steel and mild steel with conformal cooling channels," *Prog. Addit. Manuf.*, Mar. 2020, doi: 10.1007/s40964-020-00129-3.

[58] J. Boes, A. Röttger, C. Mutke, C. Escher, and W. Theisen, "Microstructure and mechanical properties of X65MoCrWV3-2 cold-work tool steel produced by selective laser melting," *Addit. Manuf.*, vol. 23, pp. 170–180, Oct. 2018, doi: 10.1016/j.addma.2018.08.005.

[59] O. Hentschel *et al.*, "Processing of AISI H11 Tool Steel Powder Modified with Carbon Black Nanoparticles for the Additive Manufacturing of Forging Tools with Tailored Mechanical Properties by Means of Laser Metal Deposition (LMD)," *Metals*, vol. 8, no. 9, Art. no. 9, Sep. 2018, doi: 10.3390/met8090659.

[60] Y. Ali, P. Henckell, J. Hildebrand, J. Reimann, J. P. Bergmann, and S. Barnikol-Oettler, "Wire arc additive manufacturing of hot work tool steel with CMT process," *J. Mater. Process. Technol.*, vol. 269, pp. 109–116, Jul. 2019, doi: 10.1016/j.jmatprotec.2019.01.034.

[61] R. Casati, M. Coduri, N. Lecis, C. Andrianopoli, and M. Vedani, "Microstructure and mechanical behavior of hot-work tool steels processed by Selective Laser Melting," *Mater. Charact.*, vol. 137, pp. 50–57, Mar. 2018, doi: 10.1016/j.matchar.2018.01.015.

[62] J. Mazumder, J. Choi, K. Nagarathnam, J. Koch, and D. Hetzner, “The direct metal deposition of H13 tool steel for 3-D components,” *JOM*, vol. 49, no. 5, pp. 55–60, May 1997, doi: 10.1007/BF02914687.

[63] J. Brooks, C. Robino, T. Headley, S. Goods, and M. Griffith, “Microstructure and Property Optimization of LENS Deposited H13 TooFSteel,” 1999. doi: http://dx.doi.org/10.26153/tsw/830.

[64] J. Choi and Y. Hua, “Dimensional and material characteristics of direct deposited H13 tool steel by CO2 laser,” *J. Laser Appl.*, vol. 16, no. 4, pp. 245–251, Nov. 2004, doi: 10.2351/1.1809638.

[65] A. J. Pinkerton and L. Li, “Direct additive laser manufacturing using gas- and water-atomised H13 tool steel powders,” *Int. J. Adv. Manuf. Technol.*, vol. 25, no. 5, pp. 471–479, Mar. 2005, doi: 10.1007/s00170-003-1844-2.

[66] R. Cottam, J. Wang, and V. Luzin, “Characterization of microstructure and residual stress in a 3D H13 tool steel component produced by additive manufacturing,” *J. Mater. Res.*, vol. 29, no. 17, pp. 1978–1986, Sep. 2014, doi: 10.1557/jmr.2014.190.

[67] J. Krell, A. Röttger, K. Geenen, and W. Theisen, “General investigations on processing tool steel X40CrMoV5-1 with selective laser melting,” *J. Mater. Process. Technol.*, vol. 255, pp. 679–688, May 2018, doi: 10.1016/j.jmatprotec.2018.01.012.

[68] M. Narvan, K. S. Al-Rubaie, and M. Elbestawi, “Process-Structure-Property Relationships of AISI H13 Tool Steel Processed with Selective Laser Melting,” *Materials*, vol. 12, no. 14, Art. no. 14, Jan. 2019, doi: 10.3390/ma12142284.

[69] H. Xiao, C. Chen, and M. Zhang, “Microstructure and Mechanical Properties of H13 Steel/High-Speed Steel Composites Prepared by Laser Metal Deposition,” *J. Mater. Eng. Perform.*, vol. 29, no. 1, pp. 66–77, Jan. 2020, doi: 10.1007/s11665-019-04476-3.

[70] F. Deirmina, N. Peghini, B. AlMangour, D. Grzesiak, and M. Pellizzari, “Heat treatment and properties of a hot work tool steel fabricated by additive manufacturing,” *Mater. Sci. Eng. A*, vol. 753, pp. 109–121, Apr. 2019, doi: 10.1016/j.msea.2019.03.027.

[71] E. B. Fonseca, A. H. G. Gabriel, L. C. Araújo, P. L. L. Santos, K. N. Campo, and E. S. N. Lopes, “Assessment of laser power and scan speed influence on microstructural features and consolidation of AISI H13 tool steel processed

by additive manufacturing," *Addit. Manuf.*, vol. 34, p. 101250, Aug. 2020, doi: 10.1016/j.addma.2020.101250.

[72] J. S. Park, J. H. Park, M.-G. Lee, J. H. Sung, K. J. Cha, and D. H. Kim, "Effect of Energy Input on the Characteristic of AISI H13 and D2 Tool Steels Deposited by a Directed Energy Deposition Process," *Metall. Mater. Trans. A*, vol. 47, no. 5, pp. 2529–2535, May 2016, doi: 10.1007/s11661-016-3427-5.

[73] J.-H. Park, K.-S. Kim, J.-Y. Kim, J.-B. Jeon, Y.-M. Koo, and K.-A. Lee, "Microstructure and tensile properties of bulk AISI D2 tool steel fabricated by direct energy deposition," *Mater. Charact.*, vol. 194, p. 112355, Dec. 2022, doi: 10.1016/j.matchar.2022.112355.

[74] G. Y. Baek, K. Y. Lee, S. H. Park, and D. S. Shim, "Effects of substrate preheating during direct energy deposition on microstructure, hardness, tensile strength, and notch toughness," *Met. Mater. Int.*, vol. 23, no. 6, pp. 1204–1215, Nov. 2017, doi: 10.1007/s12540-017-7049-2.

[75] E. M. Lee, G. W. Shin, L. Kiyong, H. S. Yoon, and D. S. Shim, "Study of High Speed Steel AISI M4 Powder Deposition using Direct Energy Deposition Process," *Trans. Mater. Process.*, vol. 25, pp. 353–358, Dec. 2016, doi: 10.5228/KSTP.2016.25.6.353.

[76] J. Choi and Y. Chang, "Characteristics of laser aided direct metal/material deposition process for tool steel," *Int. J. Mach. Tools Manuf.*, vol. 45, no. 4, pp. 597–607, Apr. 2005, doi: 10.1016/j.ijmachtools.2004.08.014.

[77] A. Bohlen, H. Freiße, M. Hunkel, and F. Vollertsen, "Additive manufacturing of tool steel by laser metal deposition," *Procedia CIRP*, vol. 74, pp. 192–195, Jan. 2018, doi: 10.1016/j.procir.2018.08.092.

[78] L. Xue, J. Chen, and S.-H. Wang, "Freeform Laser Consolidated H13 and CPM 9V Tool Steels," *Metallogr. Microstruct. Anal.*, vol. 2, no. 2, pp. 67–78, Apr. 2013, doi: 10.1007/s13632-013-0061-0.

[79] W. Wu, L. Y. Hwu, D. Y. Lin, and J. L. Lee, "The relationship between alloying elements and retained austenite in martensitic stainless steel welds," *Scr. Mater.*, vol. 42, no. 11, pp. 1071–1076, May 2000, doi: 10.1016/S1359-6462(00)00339-0.

[80] ASM Handbook Committee., *ASM Handbook–Volume 4: Heat Treating*, 10th edition. ASM International, 1991.

[81] L. Costa, R. Vilar, T. Reti, and A. M. Deus, “Rapid tooling by laser powder deposition: Process simulation using finite element analysis,” *Acta Mater.*, vol. 53, no. 14, pp. 3987–3999, Aug. 2005, doi: 10.1016/j.actamat.2005.05.003.

[82] J. Mazumder, A. Schifferer, and J. Choi, “Direct materials deposition: designed macro and microstructure,” *Mater. Res. Innov.*, vol. 3, no. 3, pp. 118–131, Oct. 1999, doi: 10.1007/s100190050137.

[83] S. Amirabdollahian, F. Deirmina, M. Pellizzari, A. Molinari, and P. Bosetti, “Heat Treatment Behavior of a Hot Work Tool Steel Produced through Direct Laser Metal Deposition,” in *Proceedings of: EuroPM 2020 Virtual Congress*, Oct. 2020.

[84] Y. Kong and H. Huang, “Effect of intrinsic heat treatment on microstructure and hardness of additively manufactured Inconel 625 alloy by directed energy deposition,” *Mater. Des.*, vol. 224, p. 111279, Dec. 2022, doi: 10.1016/j.matdes.2022.111279.

[85] H. Chae *et al.*, “Unravelling thermal history during additive manufacturing of martensitic stainless steel,” *J. Alloys Compd.*, vol. 857, p. 157555, Mar. 2021, doi: 10.1016/j.jallcom.2020.157555.

[86] V. Igwemezie, A. Mehmanparast, and F. Brennan, “The influence of microstructure on the fatigue crack growth rate in marine steels in the Paris Region,” *Fatigue Fract. Eng. Mater. Struct.*, vol. 43, no. 10, pp. 2416–2440, 2020, doi: 10.1111/ffe.13312.

[87] X. F. Ma *et al.*, “Fatigue short crack propagation behavior of selective laser melted Inconel 718 alloy by in-situ SEM study: Influence of orientation and temperature,” *Int. J. Fatigue*, vol. 139, p. 105739, Oct. 2020, doi: 10.1016/j.ijfatigue.2020.105739.

[88] E. A. Jägle, P.-P. Choi, J. Van Humbeeck, and D. Raabe, “Precipitation and austenite reversion behavior of a maraging steel produced by selective laser melting,” *J. Mater. Res.*, vol. 29, no. 17, pp. 2072–2079, Sep. 2014, doi: 10.1557/jmr.2014.204.

[89] A. Magnee, J. M. Drapier, D. Coutsouradis, L. Habrakan, and J. Dumont, “Cobalt-containing high-strength steels,” 1974, Accessed: Jul. 16, 2019. [Online]. Available: http://inis.iaea.org/Search/search.aspx?orig_q=RN:6217555

[90] V. K. Vasudevan, S. J. Kim, and C. M. Wayman, “Precipitation reactions and strengthening behavior in 18 Wt Pct nickel maraging steels,” *Metall. Trans. A*, vol. 21, no. 10, pp. 2655–2668, Oct. 1990, doi: 10.1007/BF02646061.

[91] A. M. Hall and C. J. Slunder, “The Metallurgy, Behavior, and Application of the 18-Percent Nickel Maraging Steels,” BATTELLE MEMORIAL INST COLUMBUS OH COLUMBUS LABS, NASA-SP-5051, Jan. 1968. Accessed: Jul. 17, 2019. [Online]. Available: https://apps.dtic.mil/docs/citations/ADA382105

[92] S. Floreen, “The physical metallurgy of maraging steels,” *Metall. Rev.*, vol. 13, no. 1, pp. 115–128, Jan. 1968, doi: 10.1179/mtlr.1968.13.1.115.

[93] J. Hunt, F. Derguti, and I. Todd, “Selection of steels suitable for additive layer manufacturing,” *Ironmak. Steelmak.*, vol. 41, no. 4, pp. 254–256, May 2014, doi: 10.1179/0301923314Z.000000000269.

[94] “Metal AM Summer 2016,” *Metal Additive Manufacturing*. https://www.metal-am.com/magazine-metal-summer-2016-pdf-single-page-edition/ (accessed Jul. 17, 2019).

[95] D. Bourell *et al.*, “Materials for additive manufacturing,” *CIRP Ann.*, vol. 66, no. 2, pp. 659–681, Jan. 2017, doi: 10.1016/j.cirp.2017.05.009.

[96] R. Casati, J. N. Lemke, A. Tuissi, and M. Vedani, “Aging Behaviour and Mechanical Performance of 18-Ni 300 Steel Processed by Selective Laser Melting,” *Metals*, vol. 6, no. 9, Art. no. 9, Sep. 2016, doi: 10.3390/met6090218.

[97] T. H. Becker and D. DImitrov, “The achievable mechanical properties of SLM produced Maraging Steel 300 components,” *Rapid Prototyp. J.*, vol. 22, no. 3, pp. 487–494, 2016, doi: 10.1108/RPJ-08-2014-0096.

[98] G. Casalino, S. L. Campanelli, N. Contuzzi, and A. D. Ludovico, “Experimental investigation and statistical optimisation of the selective laser melting process of a maraging steel,” *Opt. Laser Technol.*, vol. 65, pp. 151–158, Jan. 2015, doi: 10.1016/j.optlastec.2014.07.021.

[99] S. L. Campanelli, A. Angelastro, C. G. Signorile, and G. Casalino, “Investigation on direct laser powder deposition of 18 Ni (300) marage steel using mathematical model and experimental characterisation,” *Int. J. Adv. Manuf. Technol.*, vol. 89, no. 1, pp. 885–895, Mar. 2017, doi: 10.1007/s00170-016-9135-x.

[100] E. A. Jägle, Z. Sheng, P. Kürnsteiner, S. Ocylok, A. Weisheit, and D. Raabe, "Comparison of Maraging Steel Micro- and Nanostructure Produced Conventionally and by Laser Additive Manufacturing," *Materials*, vol. 10, no. 1, Art. no. 1, Jan. 2017, doi: 10.3390/ma10010008.

[101] L. Kučerová, K. Burdová, Š. Jeníček, and I. Chena, "Effect of solution annealing and precipitation hardening at 250 °C–550 °C on microstructure and mechanical properties of additively manufactured 1.2709 maraging steel," *Mater. Sci. Eng. A*, vol. 814, p. 141195, May 2021, doi: 10.1016/j.msea.2021.141195.

[102] P. Stoll, A. Spierings, K. Wegener, S. Polster, and M. Gebauer, "SLM Processing of 14 Ni (200 Grade) Maraging Steel," in *DDMC 2016: Proceedings of the 3rd Fraunhofer Direct Digital Manufacturing Conference*, 2016. doi: 10.3929/ethz-a-010802372.

[103] M. A. Kottman, "Additive Manufacturing of Maraging 250 Steels for the Rejuvenation and Repurposing of Die Casting Tooling," Case Western Reserve University, 2015. Accessed: Oct. 20, 2022. [Online]. Available: https://etd.ohiolink.edu/apexprod/rws_olink/r/1501/10?clear=10&p10_accession_num=case1416854466

[104] R. Kannan and P. Nandwana, "Thermodynamics and kinetics of precipitation and austenite reversion during aging of Ti-free grade 300 maraging steel manufactured by laser powder bed fusion (LPBF)," *J. Mater. Sci.*, vol. 56, no. 33, pp. 18722–18739, Nov. 2021, doi: 10.1007/s10853-021-06447-3.

[105] A. Hadadzadeh, A. Shahriari, B. S. Amirkhiz, J. Li, and M. Mohammadi, "Additive manufacturing of an Fe–Cr–Ni–Al maraging stainless steel: Microstructure evolution, heat treatment, and strengthening mechanisms," *Mater. Sci. Eng. A*, vol. 787, p. 139470, Jun. 2020, doi: 10.1016/j.msea.2020.139470.

[106] S. Ćirić-Kostić *et al.*, "Fatigue response of additively manufactured Maraging Stainless Steel CX and effects of heat treatment and surface finishing," *Fatigue Fract. Eng. Mater. Struct.*, vol. 45, no. 2, pp. 482–499, 2022, doi: 10.1111/ffe.13611.

[107] S. Afkhami, V. Javaheri, E. Dabiri, H. Piili, and T. Björk, "Effects of manufacturing parameters, heat treatment, and machining on the physical and mechanical properties of 13Cr10Ni1·7Mo2Al0·4Mn0·4Si steel processed by laser powder bed fusion," *Mater. Sci. Eng. A*, vol. 832, p. 142402, Jan. 2022, doi: 10.1016/j.msea.2021.142402.

[108] R. Palad, Y. Tian, K. Chadha, S. Rodrigues, and C. Aranas, “Microstructural features of novel corrosion-resistant maraging steel manufactured by laser powder bed fusion,” *Mater. Lett.*, vol. 275, p. 128026, Sep. 2020, doi: 10.1016/j.matlet.2020.128026.

[109] Y. Tian, R. Palad, L. Jiang, T. Dorin, K. Chadha, and C. Aranas, “The effect of heat treatments on mechanical properties of M789 steel fabricated by laser powder bed fusion,” *J. Alloys Compd.*, vol. 885, p. 161033, Dec. 2021, doi: 10.1016/j.jallcom.2021.161033.

[110] C. Turk, H. Zunko, C. Aumayr, H. Leitner, and M. Kapp, “Advances in Maraging Steels for Additive Manufacturing,” *BHM Berg- Hüttenmänn. Monatshefte*, vol. 164, no. 3, pp. 112–116, Mar. 2019, doi: 10.1007/s00501-019-0835-z.

[111] F. Deirmina *et al.*, “Heat Treatment And Mechanical Properties Of A Novel Ultrahigh Strength Co-free Maraging Steel Fabricated By Additive Manufacturing,” in *Proceedings of: EuroPM 2020 Virtual Congress*, Oct. 2020.

[112] D. Riabov, K. Frisk, M. Thuvander, E. Hryha, and S. Bengtsson, “Design and characterization of a cobalt-free stainless maraging steel for laser-based powder bed fusion,” *Mater. Des.*, vol. 223, p. 111180, Nov. 2022, doi: 10.1016/j.matdes.2022.111180.

[113] Z. Guo and W. Sha, “Modelling the correlation between processing parameters and properties of maraging steels using artificial neural network,” *Comput. Mater. Sci.*, vol. 29, no. 1, pp. 12–28, Jan. 2004, doi: 10.1016/S0927-0256(03)00092-2.

[114] W. Sha, A. Cerezo, and G. D. W. Smith, “Phase chemistry and precipitation reactions in maraging steels: Part IV. Discussion and conclusions,” *Metall. Mater. Trans. A*, vol. 24, no. 6, pp. 1251–1256, Jun. 1993, doi: 10.1007/BF02668193.

[115] W. Sha, “Thermodynamic calculations for precipitation in maraging steels,” *Mater. Sci. Technol.*, vol. 16, no. 11–12, pp. 1434–1436, Nov. 2000, doi: 10.1179/026708300101507415.

[116] W. W. Sun, R. K. W. Marceau, M. J. Styles, D. Barbier, and C. R. Hutchinson, “G phase precipitation and strengthening in ultra-high strength ferritic steels: Towards lean ‘maraging’ metallurgy,” *Acta Mater.*, vol. 130, pp. 28–46, May 2017, doi: 10.1016/j.actamat.2017.03.032.

[117] O. Moshka, M. Pinkas, E. Brosh, V. Ezersky, and L. Meshi, “Addressing the issue of precipitates in maraging steels – Unambiguous answer,” *Mater. Sci. Eng. A*, vol. 638, pp. 232–239, Jun. 2015, doi: 10.1016/j.msea.2015.04.067.

[118] S. Bodziak *et al.*, “Precipitation in 300 grade maraging steel built by selective laser melting: Aging at 510 °C for 2 h,” *Mater. Charact.*, vol. 151, pp. 73–83, May 2019, doi: 10.1016/j.matchar.2019.02.033.

[119] Menges, G., Michaeli, W., and Mohren, P., *How to Make Injection Molds*, 3rd ed. Hanser Publications, 2001.

[120] D. G. Lee, K. C. Jang, J. M. Kuk, and I. S. Kim, “The influence of niobium and aging treatment in the 18% Ni maraging steel,” *J. Mater. Process. Technol.*, vol. 162–163, pp. 342–349, May 2005, doi: 10.1016/j.jmatprotec.2005.02.102.

[121] H. Shirazi, G. Miyamoto, S. Hossein Nedjad, T. Chiba, M. Nili Ahmadabadi, and T. Furuhara, “Microstructure evolution during austenite reversion in Fe-Ni martensitic alloys,” *Acta Mater.*, vol. 144, pp. 269–280, Feb. 2018, doi: 10.1016/j.actamat.2017.10.068.

[122] A. Fathy, T. Mattar, H. El-Faramawy, and W. Bleck, “Mechanical properties of new low-nickel cobalt-free maraging steels,” *Steel Res.*, vol. 73, no. 12, pp. 549–556, 2002, doi: 10.1002/srin.200200027.

[123] L. Sun *et al.*, “A novel ultra-high strength maraging steel with balanced ductility and creep resistance achieved by nanoscale β-NiAl and Laves phase precipitates,” *Acta Mater.*, vol. 149, pp. 285–301, May 2018, doi: 10.1016/j.actamat.2018.02.044.

[124] Y. He, K. Yang, W. Qu, F. Kong, and G. Su, “Strengthening and toughening of a 2800-MPa grade maraging steel,” *Mater. Lett.*, vol. 56, no. 5, pp. 763–769, Nov. 2002, doi: 10.1016/S0167-577X(02)00610-9.

[125] Y. He, K. Yang, and W. Sha, “Microstructure and mechanical properties of a 2000 MPa grade co-free maraging steel,” *Metall. Mater. Trans. A*, vol. 36, no. 9, pp. 2273–2287, Sep. 2005, doi: 10.1007/s11661-005-0100-9.

[126] J. Grum and M. Zupančič, “Behaviour of 12% Ni steel with the change of initial precipitates,” *J. Mater. Process. Technol.*, vol. 155–156, pp. 2019–2025, Nov. 2004, doi: 10.1016/j.jmatprotec.2004.04.305.

[127] S. Amirabdollahian *et al.*, “Towards controlling intrinsic heat treatment of maraging steel during laser directed energy deposition,” *Scr. Mater.*, vol. 201, p. 113973, Aug. 2021, doi: 10.1016/j.scriptamat.2021.113973.

[128] L. F. Van Swam, R. M. Pelloux, and N. J. Grant, “Fatigue behavior of maraging steel 300,” *Metall. Trans. A*, vol. 6, no. 1, pp. 45–54, Jan. 1975, doi: 10.1007/BF02673669.

[129] B.-Z. Weiss, “Maraging Steels—Structure, Properties and Applications,” in *Specialty Steels and Hard Materials*, N. R. Comins and J. B. Clark, Eds. Pergamon, 1983, pp. 35–54. doi: 10.1016/B978-0-08-029358-5.50009-4.

[130] J. Suryawanshi, K. G. Prashanth, and U. Ramamurty, “Tensile, fracture, and fatigue crack growth properties of a 3D printed maraging steel through selective laser melting,” *J. Alloys Compd.*, vol. 725, pp. 355–364, Nov. 2017, doi: 10.1016/j.jallcom.2017.07.177.

[131] P. L. L. Santos, J. A. Avila, E. B. da Fonseca, A. H. G. Gabriel, A. L. Jardini, and É. S. N. Lopes, “Plane-strain fracture toughness of thin additively manufactured maraging steel samples,” *Addit. Manuf.*, vol. 49, p. 102509, Jan. 2022, doi: 10.1016/j.addma.2021.102509.

[132] X. Yan *et al.*, “Additive manufacturing of WC reinforced maraging steel 300 composites by cold spraying and selective laser melting,” *Surf. Coat. Technol.*, vol. 371, pp. 161–171, Aug. 2019, doi: 10.1016/j.surfcoat.2018.03.072.

[133] J. Hu, H. Zhu, J. Zhang, M. Ouyang, C. Qiu, and J. Duan, “Effects of TiC addition on microstructure, microhardness and wear resistance of 18Ni300 maraging steel by direct laser deposition,” *J. Mater. Process. Technol.*, vol. 296, p. 117213, Oct. 2021, doi: 10.1016/j.jmatprotec.2021.117213.

[134] Z. Li, B. Teng, B. Yao, and J. Liu, “Microstructure and mechanical properties of WC reinforced 18Ni300 composites produced by selective laser melting,” *Mater. Charact.*, vol. 180, p. 111406, Oct. 2021, doi: 10.1016/j.matchar.2021.111406.

[135] N. Kang *et al.*, “Selective laser melting of tungsten carbide reinforced maraging steel composite,” *Addit. Manuf.*, vol. 22, pp. 104–110, Aug. 2018, doi: 10.1016/j.addma.2018.04.031.

[136] K. Shetty, S. Kumar, and P. Raghothama Rao, “Effect of ion nitriding on the microstructure and properties of Maraging steel (250 Grade),” *Surf. Coat. Technol.*, vol. 203, no. 10, pp. 1530–1536, Feb. 2009, doi: 10.1016/j.surfcoat.2008.11.034.

[137] Y. Hong *et al.*, “Improving surface mechanical properties of the selective laser melted 18Ni300 maraging steel via plasma nitriding,” *Surf. Coat. Technol.*, vol. 406, p. 126675, Jan. 2021, doi: 10.1016/j.surfcoat.2020.126675.

[138] M. Godec, B. Podgornik, A. Kocijan, Č. Donik, and D. A. S. Balantič, "Use of plasma nitriding to improve the wear and corrosion resistance of 18Ni-300 maraging steel manufactured by selective laser melting," *Sci. Rep.*, vol. 11, no. 1, p. 3277, Feb. 2021, doi: 10.1038/s41598-021-82572-y.

[139] S. Shakerin, M. Sanjari, B. S. Amirkhiz, and M. Mohammadi, "Interface engineering of additively manufactured maraging steel-H13 bimetallic structures," *Mater. Charact.*, vol. 170, p. 110728, Dec. 2020, doi: 10.1016/j.matchar.2020.110728.

[140] S. Shakerin, A. Hadadzadeh, B. S. Amirkhiz, S. Shamsdini, J. Li, and M. Mohammadi, "Additive manufacturing of maraging steel-H13 bimetals using laser powder bed fusion technique," *Addit. Manuf.*, vol. 29, p. 100797, Oct. 2019, doi: 10.1016/j.addma.2019.100797.

[141] P. Kürnsteiner, M. B. Wilms, A. Weisheit, B. Gault, E. A. Jägle, and D. Raabe, "High-strength Damascus steel by additive manufacturing," *Nature*, vol. 582, no. 7813, Art. no. 7813, Jun. 2020, doi: 10.1038/s41586-020-2409-3.

[142] P. Kürnsteiner, M. B. Wilms, A. Weisheit, P. Barriobero-Vila, E. A. Jägle, and D. Raabe, "Massive nanoprecipitation in an Fe-19Ni-xAl maraging steel triggered by the intrinsic heat treatment during laser metal deposition," *Acta Mater.*, vol. 129, pp. 52–60, May 2017, doi: 10.1016/j.actamat.2017.02.069.

[143] Z. B. Jiao, J. H. Luan, Z. W. Zhang, M. K. Miller, and C. T. Liu, "High-strength steels hardened mainly by nanoscale NiAl precipitates," *Scr. Mater.*, vol. 87, pp. 45–48, Sep. 2014, doi: 10.1016/j.scriptamat.2014.05.006.

[144] A. A. Hassen *et al.*, "Scaling Up metal additive manufacturing process to fabricate molds for composite manufacturing," *Addit. Manuf.*, vol. 32, p. 101093, Mar. 2020, doi: 10.1016/j.addma.2020.101093.

[145] N. Shamsaei, A. Yadollahi, L. Bian, and S. M. Thompson, "An overview of Direct Laser Deposition for additive manufacturing; Part II: Mechanical behavior, process parameter optimization and control," *Addit. Manuf.*, vol. 8, pp. 12–35, Oct. 2015, doi: 10.1016/j.addma.2015.07.002.

[146] F. Deirmina, N. Peghini, B. AlMangour, D. Grzesiak, and M. Pellizzari, "Heat treatment and properties of a hot work tool steel fabricated by additive manufacturing," *Mater. Sci. Eng. A*, vol. 753, pp. 109–121, Apr. 2019, doi: 10.1016/j.msea.2019.03.027.

[147] M. Yuan *et al.*, “Characteristics of a modified H13 hot-work tool steel fabricated by means of laser beam powder bed fusion,” *Mater. Sci. Eng. A*, vol. 831, p. 142322, Jan. 2022, doi: 10.1016/j.msea.2021.142322.

[148] R. Shivpuri, “Dies and Die Materials for Hot Forging,” Jan. 2005, doi: 10.31399/asm.hb.v14a.a0003975.

[149] F. Cajner, D. Landek, and V. Leskovšek, “Surface modifications of maraging steels used in the manufacture of moulds and dies,” *undefined*, 2010, Accessed: Oct. 21, 2022. [Online]. Available: https://www.semanticscholar.org/author/D.-Landek/48102824

[150] Escher, C. and Henke, T., “New trends in thin coatings for sheet metal forming tools,” in *Proceedings of the 6th International Tooling Conference*, Karlstad, Sweden, Sep. 2002, pp. 919–933. Accessed: Jan. 16, 2023. [Online]. Available: https://scholar.google.com/scholar_lookup?title=New%20trends%20in%20thin%20coatings%20for%20sheet%20metal%20forming%20tools&pages=919-933&publication_year=2002&author=Escher%2CC&author=Henke%2CT

[151] J. Fox and S. Weisberg, *An R Companion to Applied Regression*. SAGE Publications, 2018.

[152] “Maud – Materials Analysis Using Diffraction.” http://nanoair.dii.unitn.it:8080/maud/ (accessed Dec. 08, 2021).

[153] B. Ekmekci, “Residual stresses and white layer in electric discharge machining (EDM),” *Appl. Surf. Sci.*, vol. 253, no. 23, pp. 9234–9240, Sep. 2007, doi: 10.1016/j.apsusc.2007.05.078.

[154] “Measuring Residual Stress Caused by Wire EDM of Tool Steel,” *Int. J. Electr. Mach.*, vol. 5, pp. 23–28, 2000, doi: 10.2526/ijem.5.23.

[155] K. Poorna Chander, M. Vashista, K. Sabiruddin, S. Paul, and P. P. Bandyopadhyay, “Effects of grit blasting on surface properties of steel substrates,” *Mater. Des.*, vol. 30, no. 8, pp. 2895–2902, Sep. 2009, doi: 10.1016/j.matdes.2009.01.014.

[156] J. M. Guilemany, N. Llorca-Isern, and P. J. Szabo, “RESIDUAL STRESS CHARACTERISATION OF GRIT BlASTED STEEL SURFACES,” *Surf. Eng.*, vol. 12, no. 1, pp. 77–79, Jan. 1996, doi: 10.1179/sur.1996.12.1.77.

[157] A. Aversa *et al.*, “The role of Directed Energy Deposition atmosphere mode on the microstructure and mechanical properties of 316L samples,” *Addit. Manuf.*, vol. 34, p. 101274, Aug. 2020, doi: 10.1016/j.addma.2020.101274.

[158] Y. Huang *et al.*, "Rapid prediction of real-time thermal characteristics, solidification parameters and microstructure in laser directed energy deposition (powder-fed additive manufacturing)," *J. Mater. Process. Technol.*, vol. 274, p. 116286, Dec. 2019, doi: 10.1016/j.jmatprotec.2019.116286.

[159] P. Grgac, M. Liptak, M. Behulova, L. Caplovic, H.-G. Lindenkreuz, and W. Löser, "Influence of melt undercooling on the microstructure of levitated Cr–Mo–V tool steel," *Mater. Sci. Eng. A*, vol. 449–451, pp. 658–661, Mar. 2007, doi: 10.1016/j.msea.2006.02.428.

[160] J. Platl, H. Leitner, C. Turk, A. G. Demir, B. Previtali, and R. Schnitzer, "Defects in a Laser Powder Bed Fused Tool Steel," *Adv. Eng. Mater.*, vol. n/a, no. n/a, p. 2000833, doi: 10.1002/adem.202000833.

[161] R. Staśko, H. Adrian, and A. Adrian, "Effect of nitrogen and vanadium on austenite grain growth kinetics of a low alloy steel," *Mater. Charact.*, vol. 56, no. 4, pp. 340–347, Jun. 2006, doi: 10.1016/j.matchar.2005.09.012.

[162] F. Deirmina and M. Pellizzari, "Mechanical properties and tempering resistance of an ultrafine grained Tool Steel-PSZ composite fabricated by high energy mechanical milling and spark plasma sintering," *Mater. Sci. Eng. A*, vol. 786, p. 139428, Jun. 2020, doi: 10.1016/j.msea.2020.139428.

[163] R. Lagneborg, B. Hutchinson, T. Siwecki, and S. Zajac, "The role of vanadium in microalloyed steels," in *Proc. Michael Korchynsky Symp., MS&T Conf., Pittsburgh, PA, USA*, 2014, pp. 1–95.

[164] X. Di, M. Li, Z. Yang, B. Wang, and X. Guo, "Microstructural evolution, coarsening behavior of vanadium carbide and mechanical properties in the simulated heat-affected zone of modified medium manganese steel," *Mater. Des.*, vol. 96, pp. 232–240, Apr. 2016, doi: 10.1016/j.matdes.2016.02.038.

[165] N. K. Balliger and R. W. K. Honeycombe, "Coarsening of vanadium carbide, carbonitride, and nitride in low-alloy steels," *Met. Sci.*, vol. 14, no. 4, pp. 121–133, Apr. 1980, doi: 10.1179/030634580790426337.

[166] J. Sjöström and J. Bergström, "Thermal fatigue testing of chromium martensitic hot-work tool steel after different austenitizing treatments," *J. Mater. Process. Technol.*, vol. 153–154, pp. 1089–1096, Nov. 2004, doi: 10.1016/j.jmatprotec.2004.04.158.

[167] M. Pellizzari, S. Furlani, F. Deirmina, R. Siriki, B. AlMangour, and D. Grzesiak, "Fracture Toughness of a Hot Work Tool Steel Fabricated by

Laser-Powder Bed Fusion Additive Manufacturing," *Steel Res. Int.*, vol. 91, no. 5, p. 1900449, 2020, doi: 10.1002/srin.201900449.

[168] A. Medvedeva, J. Bergström, S. Gunnarsson, and J. Andersson, "High-temperature properties and microstructural stability of hot-work tool steels," *Mater. Sci. Eng. A*, vol. 523, no. 1, pp. 39–46, Oct. 2009, doi: 10.1016/j.msea.2009.06.010.

[169] F. Deirmina and M. Pellizzari, "Strengthening mechanisms in an ultrafine grained powder metallurgical hot work tool steel produced by high energy mechanical milling and spark plasma sintering," *Mater. Sci. Eng. A*, vol. 743, pp. 349–360, Jan. 2019, doi: 10.1016/j.msea.2018.11.093.

[170] A. Eser, C. Broeckmann, and C. Simsir, "Multiscale modeling of tempering of AISI H13 hot-work tool steel – Part 1: Prediction of microstructure evolution and coupling with mechanical properties," *Comput. Mater. Sci.*, vol. 113, pp. 280–291, Feb. 2016, doi: 10.1016/j.commatsci.2015.11.020.

[171] G. Krauss, "Tempering of Lath Martensite in Low and Medium Carbon Steels: Assessment and Challenges," *Steel Res. Int.*, vol. 88, no. 10, p. 1700038, 2017, doi: 10.1002/srin.201700038.

[172] D. P. Koistinen and R. E. Marburger, "A general equation prescribing the extent of the austenite-martensite transformation in pure iron-carbon alloys and plain carbon steels," *Acta Metall.*, vol. 7, no. 1, pp. 59–60, Jan. 1959, doi: 10.1016/0001-6160(59)90170-1.

[173] H. Ghassemi-Armaki, R. P. Chen, K. Maruyama, M. Yoshizawa, and M. Igarashi, "Static recovery of tempered lath martensite microstructures during long-term aging in 9–12% Cr heat resistant steels," *Mater. Lett.*, vol. 63, no. 28, pp. 2423–2425, Nov. 2009, doi: 10.1016/j.matlet.2009.08.024.

[174] B. Sonderegger *et al.*, "Kinetics of Precipitation in a Complex Hot-work Tool Steel," *Steel Res. Int.*, vol. 81, no. 1, pp. 64–73, 2010, doi: 10.1002/srin.200900069.

[175] M. Pellizzari and A. Molinari, "Deep cryogenic treatment of cold work tool steel," in *proc. of the 6th Int. Tooling Conf., Karlstad, Sweden, Karlstad University*, 2002, pp. 547–558.

[176] X. Zhao *et al.*, "The effect of thermal cycling on direct laser-deposited gradient H13 tool steel: Microstructure evolution, nanoprecipitation behaviour, and mechanical properties," *Mater. Today Commun.*, vol. 25, p. 101390, Dec. 2020, doi: 10.1016/j.mtcomm.2020.101390.

[177] M. Pellizzari, S. Furlani, F. Deirmina, R. Siriki, B. AlMangour, and D. Grzesiak, “Fracture Toughness of a Hot Work Tool Steel Fabricated by Laser-Powder Bed Fusion Additive Manufacturing,” *Steel Res. Int.*, vol. 91, no. 5, p. 1900449, 2020, doi: 10.1002/srin.201900449.

[178] M. Pellizzari, A. Fedrizzi, and M. Zadra, “Influence of processing parameters and particle size on the properties of hot work and high speed tool steels by Spark Plasma Sintering,” *Mater. Des.*, vol. 32, no. 4, pp. 1796–1805, Apr. 2011, doi: 10.1016/j.matdes.2010.12.033.

[179] T. Yuxin, L. Minghe, C. Haiyan, Y. Guanghong, and X. Zhou, “Effects of quenching temperature on microstructure and mechanical properties of H13 mandrel steel,” *Baosteel Tech. Res.*, vol. 4, no. 3, p. 58, 2010.

[180] B.-W. Lee, J. Jang, and D. Kwon, “Evaluation of fracture toughness using small notched specimens,” *Mater. Sci. Eng. A*, vol. 334, no. 1, pp. 207–214, Sep. 2002, doi: 10.1016/S0921-5093(01)01804-4.

[181] S. Lynch, “A review of underlying reasons for intergranular cracking for a variety of failure modes and materials and examples of case histories,” *Eng. Fail. Anal.*, vol. 100, pp. 329–350, Jun. 2019, doi: 10.1016/j.engfailanal.2019.02.027.

[182] Committee and K. Mills, *ASM Handbook, Volume 12: Fractography*, 9th ed. 1987.

[183] Q. Zhou, X. Wu, N. Shi, J. Li, and N. Min, “Microstructure evolution and kinetic analysis of DM hot-work die steels during tempering,” *Mater. Sci. Eng. A*, vol. 528, no. 18, pp. 5696–5700, Jul. 2011, doi: 10.1016/j.msea.2011.04.024.

[184] J. H. Hollomon and L. D. Jaffe, “Time-Temperature Relations In Tempering Steel,” *Trans. Am. Inst. Min. Metall. Eng.*, vol. 162, pp. 223–249, 1945.

[185] F. R. Larson and J. Miller, “A Time-Temperature Relationship for Rupture and Creep Stresses,” *Trans. Am. Soc. Mech. Eng.*, vol. 74, no. 5, pp. 765–771, 1952, doi: 10.1115/1.4015909.

[186] L. C. F. Canale, X. Yao, J. Gu, and G. E. Totten, “A historical overview of steel tempering parameters,” *Int. J. Microstruct. Mater. Prop.*, vol. 3, no. 4–5, pp. 474–525, Jan. 2008, doi: 10.1504/IJMMP.2008.022033.

[187] Z. Zhang, D. Delagnes, and G. Bernhart, “Microstructure evolution of hot-work tool steels during tempering and definition of a kinetic law based on

hardness measurements," *Mater. Sci. Eng. A*, vol. 380, no. 1, pp. 222–230, Aug. 2004, doi: 10.1016/j.msea.2004.03.067.

[188] A. Komodromos, F. Kolpak, and A. E. Tekkaya, "Manufacturing of Integrated Cooling Channels by Directed Energy Deposition for Hot Stamping Tools with Ball Burnished Surfaces," *BHM Berg- Hüttenmänn. Monatshefte*, vol. 167, no. 9, pp. 428–434, Sep. 2022, doi: 10.1007/s00501-022-01264-w.

[189] H. Bhadeshia and R. Honeycombe, *Steels: Microstructure and Properties*, 4th ed. Elsevier, 2017.

[190] K. Wieczerzak *et al.*, "The effect of temperature on the evolution of eutectic carbides and M7C3 → M23C6 carbides reaction in the rapidly solidified Fe-Cr-C alloy," *J. Alloys Compd.*, vol. 698, pp. 673–684, Mar. 2017, doi: 10.1016/j.jallcom.2016.12.252.

[191] B.-J. Lee, "On the stability of Cr carbides," *Calphad*, vol. 16, no. 2, pp. 121–149, Apr. 1992, doi: 10.1016/0364-5916(92)90002-F.

[192] J.-Y. Li, Y.-L. Chen, and J.-H. Huo, "Mechanism of improvement on strength and toughness of H13 die steel by nitrogen," *Mater. Sci. Eng. A*, vol. 640, pp. 16–23, Jul. 2015, doi: 10.1016/j.msea.2015.05.006.

[193] B. Ren, D. Lu, R. Zhou, Z. Li, and J. Guan, "Preparation and mechanical properties of selective laser melted H13 steel," *J. Mater. Res.*, vol. 34, no. 8, pp. 1415–1425, Apr. 2019, doi: 10.1557/jmr.2019.10.

[194] M. Ackermann, J. Šafka, L. Voleský, J. Bobek, and J. R. Kondapally, "Impact Testing of H13 Tool Steel Processed with Use of Selective Laser Melting Technology," *Mater. Sci. Forum*, vol. 919, pp. 43–51, 2018, doi: 10.4028/www.scientific.net/MSF.919.43.

[195] Z. Fan, "The grain size dependence of ductile fracture toughness of polycrystalline metals and alloys," *Mater. Sci. Eng. A*, vol. 191, no. 1, pp. 73–83, Feb. 1995, doi: 10.1016/0921-5093(94)09621-3.

[196] N. Du *et al.*, "Microstructural Stability and Softening Resistance of a Novel Hot-Work Die Steel," *Crystals*, vol. 10, no. 4, Art. no. 4, Apr. 2020, doi: 10.3390/cryst10040238.

[197] O. Moshka, M. Pinkas, E. Brosh, V. Ezersky, and L. Meshi, "Addressing the issue of precipitates in maraging steels – Unambiguous answer," *Mater. Sci. Eng. A*, vol. 638, pp. 232–239, Jun. 2015, doi: 10.1016/j.msea.2015.04.067.

[198] R. Kapoor and I. S. Batra, “On the α′ to γ transformation in maraging (grade 350), PH 13-8 Mo and 17-4 PH steels,” *Mater. Sci. Eng. A*, vol. 371, no. 1, pp. 324–334, Apr. 2004, doi: 10.1016/j.msea.2003.12.023.

[199] A. Goldberg and D. G. O’connor, “Influence of Heating Rate on Transformations in an 18 per cent Nickel Maraging Steel,” *Nature*, vol. 213, no. 5072, Art. no. 5072, Jan. 1967, doi: 10.1038/213170a0.

[200] I. R. Souza Filho *et al.*, “Martensite to austenite reversion in a high-Mn steel: Partitioning-dependent two-stage kinetics revealed by atom probe tomography, in-situ magnetic measurements and simulation,” *Acta Mater.*, vol. 166, pp. 178–191, Mar. 2019, doi: 10.1016/j.actamat.2018.12.046.

[201] E. Galindo-Nava, W. Rainforth, and P. Rivera-Díaz-del-Castillo, “Predicting microstructure and strength of maraging steels: Elemental optimisation,” *Acta Mater.*, vol. 117, pp. 270–285, 2016.

[202] S. Morito, J. Nishikawa, and T. Maki, “Dislocation density within lath martensite in Fe-C and Fe-Ni alloys,” *ISIJ Int.*, vol. 43, no. 9, pp. 1475–1477, 2003.

[203] R. L. Fleischer, “Substitutional solution hardening,” *Acta Metall.*, vol. 11, no. 3, pp. 203–209, 1963.

[204] F. Habiby, T. N. Siddiqui, H. Hussain, A. Ul Haq, and A. Q. Khan, “Lattice changes in the martensitic phase due to ageing in 18 wt% nickel maraging steel grade 350,” *J. Mater. Sci.*, vol. 31, no. 2, pp. 305–309, Jan. 1996, doi: 10.1007/BF01139144.

[205] O. Moshka, M. Pinkas, E. Brosh, V. Ezersky, and L. Meshi, “Addressing the issue of precipitates in maraging steels – Unambiguous answer,” *Mater. Sci. Eng. A*, vol. 638, pp. 232–239, Jun. 2015, doi: 10.1016/j.msea.2015.04.067.

[206] R. O. Ritchie, “On the interaction of cracks with bimaterial interfaces,” *Mater. Sci.*, vol. 32, no. 1, pp. 107–120, Jan. 1996, doi: 10.1007/BF02538931.

# Scientific Production

**International Journals:**

[1] S. Amirabdollahian et al., "Towards controlling intrinsic heat treatment of maraging steel during laser directed energy deposition," Scr. Mater., vol. 201, p. 113973, Aug. 2021, doi: 10.1016/j.scriptamat.2021.113973.

[2] S. Amirabdollahian, F. Deirmina, M. Pellizzari, P. Bosetti, and A. Molinari, "Tempering behavior of a direct laser deposited hot work tool steel: Influence of quenching on secondary hardening and microstructure," Mater. Sci. Eng. A, vol. 814, p. 141126, May 2021, doi: 10.1016/j.msea.2021.141126.

[3] H. Rajaei, C. Menapace, S. Amirabdollahian, M. Perini, G. Straffelini, and S. Gialanella, "Microstructural and Tribological Evaluation of Brake Disc Refurbishing Using Fe-Based Coating via Directed Energy Deposition," Metals, vol. 12, no. 3, p. 465, 2022.

[4] M. Pellizzari, D. Massignani, S. Amirabdollahian, and F. Deirmina, "Thermal Fatigue Behavior of AISI H13 Hot Work Tool Steel Produced by Direct Laser Metal Deposition," Steel Res. Int., vol. n/a, no. n/a, p. 2200449, doi: 10.1002/srin.202200449.

[5] S. Amirabdollahian, F. Deirmina, L. Harris, E. Bettini, R. Siriki, M. Pellizzari, P. Bosetti, A. Molinari, "Laser-directed energy deposition of dissimilar maraging steels with a defect-free interface: design for improved surface hardness and fracture toughness,", under review.

**Proceedings:**

[1] S. Amirabdollahian, F. Deirmina, M. Pellizzari, P. Bosetti, M. Benedetti, and A. Molinari, "The effect of different post-processing thermal treatments on the mechanical properties and tempering resistance of additively manufactured H13 hot work tool steel," in Proceedings of Tooling 2022, Orebro, Sweden, Apr. 2022.

[2] S. Amirabdollahian, M. Perini, T. Tekin, P. Bosetti, and A. Molinari, "Characterization and Heat Treatment of an Additively Manufactured Tool Steel Fabricated by Laser Directed Energy Deposition," in Proceedings of Tooling 2022, Orebro, Sweden, Apr. 2022.

[3] Amirabdollahian, S., Eslami, M., Bosetti, P., Perini, M., and Molinari, A., "Heat Treatment and Properties of AISI 415 Martensitic Stainless Steel Manufactured by Laser-Directed Energy Deposition," in World PM 2022 Congress and Exhibition, Lyon, France, Oct. 2022.

[4] De Bortoli, L. et al., "A microstructural analysis of the bonding layer in the manufacturing of Co alloy / Ti alloy bimetallic components by Directed Energy Deposition," in World PM 2022 Congress and Exhibition, Lyon, France, Oct. 2022.

[5] A. T. Silvestri, S. Amirabdollahian, M. Perini, P. Bosetti, and A. Squillace, "Direct Laser Deposition for Tailored Structure," in Proceedings of ESAFORM 2021, Liège, Belgium, Apr. 2021.

[6] S. Amirabdollahian, F. Deirmina, M. Pellizzari, A. Molinari, and P. Bosetti, "Heat Treatment Behavior of a Hot Work Tool Steel Produced through Direct Laser Metal Deposition," in Proceedings of EuroPM 2020 Virtual Congress, Oct. 2020.

[7] M. Zago, I. Cristofolini, and S. Amirabdollahian, "Designing Powder Metallurgy Process-The Influence of High Sintering Temperature on Dimensional and Geometrical Precision," in International Joint Conference on Mechanics, Design Engineering & Advanced Manufacturing, 2020, pp. 3–8.

[8] M. Perini, S. Amirabdollahian, and P. Bosetti, "Building Multi-Material components by Direct Laser Deposition," in MATEC Web of Conferences, 2019, vol. 299, p. 01006.